DRAFT
EIC PDR
September 29, 2024

Electron Ion Collider
Preliminary Design Report

Contributors:

E-C. Aschenauer[1], R. Ent[2], S. Joosten[3], M. Żurek[3], ADD NAMES AND INSTITUTIONS

[1]Brookhaven National Laboratory, USA
[2]Thomas Jefferson National Accelerator Facility, USA
[3]Argonne National Laboratory, USA

Contents

List of Figures

List of Tables

multi-chapters

Chapter 0

Style Guide

The following is the Style guild as developed for the full design report. This is the guide the accelerator team is following and it will make merging the documents together much easier if everyone uses this guide.

0.1 Chapter Abstract

Summary: Each chapter begins with a stand-alone single “punch line” page that serves as a chapter abstract. Rather than simply duplicating the Table of Contents outline of the subject matter of the chapter, a well-constructed abstract will lay out the key ideas and conclusions that chapter editors wish to convey to readers. The Executive Summary will also describe these key ideas, in a modestly longer form (perhaps $\sim 250 - 1000$ words per chapter). This sample **non-EIC** chapter abstract emphasizes key ideas such as the separation of pre-existing and new subsystems, and the level of technical risk.

The Cryogenic System consists of the cryoplant that provides cooling for cryomodules; the test and instruments cryoplant that provides cooling for test stands and liquid helium for instruments; cryoplant that provides 16 K helium cooling for the target hydrogen moderators, and the distribution system that connects the linac cryoplant to cryomodules. The linac cryoplant and test/instrument cryoplant share common gas management and storage systems. The target cryoplant system is completely separate due to potential for tritium contamination.

The Vacuum System provides vacuum for the linac beam line, target system and instrument lines. It uses well established technology and procedures based on experience at similar facilities, including RHIC, Tevatron, and LHC. It has low technical risk.

Test Stands provide testing and validation of both RF equipment (klystrons and modulators) and cryomodules. Cryogenic connection to cryomodules in the test stands will prototype similar connections in the linac tunnel. The test stand program accommodates the unavoidable uncertainty in EIC construction schedule by allowing for RF equipment testing in a temporary location if necessary. Cryomodule testing will be carried out at the EIC site. All cryomodules will be tested at nominal temperatures and RF power levels before tunnel installation.

0.2 Wordsmithing

0.2.1 Passive voice

Authors should avoid the passive voice as much as possible – as in this sentence. This rule is sometimes made to be broken – as in this sentence :). The crucial point is that authors should not use passive voice to avoid identifying the specific individual or group of individuals within the EIC organization which is/are (or will be) responsible for fulfilling some specific function. It's not good enough to say, "Quality management will be implemented". The purpose of the Design Report is to explain for EIC itself, and for readers outside of EIC, who will implement quality management, and how they will do it. Excessive use of passive voice is not just bad writing. It communicates confusion or uncertainty about the path from aspiration to reality.

0.2.2 Verb tenses

The simplest way to make everything consistent is to apply a general rule:

> Use past tense for things that happened in the past, present tense for things that are happening now, and future tense for things that will happen in the future.

If the designs call for something to happen, they call for it in the present tense. But it will happen in the future tense. Avoid inconsistent usage across chapters, across authors, and even within the same paragraph by a single author.

0.2.3 Apostrophes

Decades are written as in the 1960s and 1970s, NOT as in the 1980's or 1990's.

0.2.4 Capitalization and names

0.2.4.1 Pieces of EIC

For example, linac, accelerator, target station, test stand. For the sake of consistency these terms will not be capitalized.

0.2.4.2 Internal phrases

Correct capitalization for specific "internal" EIC phrases and names will be accumulated here. For example:

> Pre-construction Phase NOT Pre-Construction phase
> Decommissioning Phase NOT De-commissioning phase
> Work Packages NOT Work-packages

0.2.4.3 Discipline-specific approaches or “guiding principles” or buzz phrases

Such as design integration, systems engineering, defense in depth. Recommend capitalizing none of them, but the important thing is to be consistent.

0.2.4.4 Formal group names

When authors identify the parts of the EIC organization who will be responsible for doing something, then capitalize the formal names of that groups from the org chart. Recommend avoiding informal terms such as “test stand personnel”, where possible.

0.2.4.5 Headings

The titles of sections and subsections should have only the first letter capitalized.

0.2.5 Captions

Write Figure and Table captions in a self-contained way, to carry a complete self-contained description of the figure. Define symbology in all figures, either in the text or (preferably) in the caption. Captions always end with a period. Use the format:

```
\caption[Short caption for List of Tables or Figures.]{Long caption to carry a complete
self-contained description of the figure or table, in the chapter text.}
```

0.2.6 Spelling

The Design Report follows American spelling rules. For example, with “z” not “s”, and “program” not “programme”:

emphasize not emphasise
meter not metre

0.2.6.1 Exceptions to U.S. spelling

1. (None so far).

0.2.6.2 Capitalization

The words “Figure”, “Table”, “Chapter” and “Section” should always be capitalized in the text if they occur with a number. For example, Figure 3.8 occurs in Chapter 3 and Table 5.5 is in Section 5.1.3, but there are many other figures and tables in other section, subsections and chapters.

0.2.7 Commas

The incorrect placement of a comma can change the meaning of a sentence. For example, compare "Let's eat Mom" and "Let's eat, Mom". And compare "Scientists, who conduct important research, are well respected in the community" with "Scientists who conduct important research are well respected in the community".

Commas go where there is a natural pause in a long sentence, where additional information has been added to a sentence and where, if removed, the sentence would still make sense. They are used when listing items – between each item on the list. They are used where two shorter sentences are made into one (usually with the addition of "and"), but still consist of two separate parts. And they are used after "lead" words [however, therefore, consequently, in fact].

0.2.7.1 Commas in numbers

Write 2.4 million and not 2,4 million (as in some parts of Europe).

No commas in numbers below 10,000 – thus, write 1240 and 9999, but 12,400 and 99,999.

0.2.8 Plurals and possessives

For example, use

WPs not WP's (plural)
EIC's not EIC' (possessive)

0.2.9 Abbreviations

0.2.9.1 Textual treatment of Figures and Tables

The words "Figure" and "Table" should always be capitalized in the text. Include a reference or discussion of all Tables and Figures in the main text of the chapter. For example, "Figure 3.8 shows thus-and-such". The abbreviations Fig. and Tab. should not be used.

0.2.9.2 Radio frequency

The phrase "radio frequency" is always two words and is never hyphenated or capitalized, whether used as an adjective or as a noun. Thus, the two radio frequencies used in the radio frequency system are 352.21 MHz and 704.42 MHz. The upper case abbreviation "RF" is acceptable in many circumstances.

0.2.9.3 etc., et cetera

It is acceptable to use "e.g." within parentheses, but not outside. For example, Jack and Jill met many animals (e.g. Reynard the Fox) when going down the hill. It is also correct to say that Jack and Jill met many animals, for example Reynard the Fox, but no tortoise. Similar rules apply for "i.e.".

The periods (i.e. the full stops) should not be dropped, for example "ie" or "eg".

It is incorrect to use ok, o.k., or okay.

The following are acceptable:

> e.g.
> etc.
> i.e.
> RF (in many circumstances)

0.2.10 Hyphenation of multi-word adjectival phrases

In general, hyphenate an adjectival phrase where the second part is a past (-ed) or present (-ing) participle of a verb. Consider the following illustrative (nonsensical) paragraph:

> This chapter describes the *beam physics design* of the *neutron-generating* spallation target. Following a brief overview, the chapter presents a detailed description of the *beam physics* of EIC, which drive the accelerator design. The accelerator consists of several sections: the ion source, *normal-conducting* linac, *superconducting* linac and *beam transport* sections. The chapter also describes the *radio frequency* system.

Simplified advice available online includes: *"When two or more words are combined to form a modifier immediately preceding a noun, join the words by hyphens if doing so will significantly aid the reader in recognizing the compound adjective."* Not so simple are phrases like "high-power proton beam" where "proton beam" itself is a single idea. Some judgement is involved . . . .

For the sake of consistency, the editors have created and are expanding a spreadsheet of words and phrases specifying hyphenation policy for the Design Repoprt. Here are somewhat-arbitrary rules for whether or not to hyphenate some common multi-word phrases, *when they are used as an adjective, a noun, or as a verb*. Alphabetically:

> 1D, 2D, 3D, 4D
> accelerator-driven
> back up (verb)
> back-flow (noun adj)
> backscattering
> backup (adj noun)
> baseline (adj or noun)
> beam dynamics
> beam guide
> beam instrumentation

beam physics
beampipe
beam port
beam time
beam transport
beamline
bispectral
bottom-up approach
broadband
by-product
clamshell clamshell-style
clean room
cold box
co-chair (noun)
contact-less
cool-down (noun or adj)
coordinate
cost-saving
cross reference (noun)
cross-reference (verb)
cross section
cryo-building
cryo-pump
cryo-system
cryomodule
cryoplant
debunched
decision making (noun)
decommissioning
de-excitation
deionised
down-mix
downtime
eigenmode (noun adj)
equipartitioning
failover
failsafe
feed box
feedthrough
follow up (verb)
follow-up (adj and noun)
hands-on (adj)
high level
high-β
high-current (adj)
high-power
high-resolution
hot cell
in situ (italicize)
innermost
inrush

interdependency
interlayer
intra-layer
intra-nuclear
Joule-Thomson valve
layout (noun)
life-cycle (noun)
line-of-sight
long-pulse
lookup
Lorentz detuning (noun)
Lorentz-detuning (adj)
low-resolution
magnetoresistance
medium-β
metadata
micropattern
microphonics
midpoint
middleware
multi-component
multi-layer
multi-pacting
multi-particle
multi-resistant
nanoparticle
nano-sized
nanostructure
neutron-generating
noninvasive (seen both ways in different dictionaries)
normal-conducting
on-board
ongoing
on-site (adj)
outermost
outgassing
overarching
phase space (noun)
phase-space (adj)
pinpoint
plug-in
post mortem (noun or adj)
pre-cools
premoderator
prequalification
radio frequency
radionuclide
radiotoxic
ramp up (verb)
ramp-up (noun)
read-back

ready-made
requalification
roadmap
safety-critical
short-pulse
short-term
shut off (noun verb)
shut-off (adj)
space charge (noun)
space-charge (adj)
staff-based
start-up
state-of-the-art
storm water
stripline
sub-atmospheric
subcomponent
sub-cool
sub-millimeter
sub-second
superconducting
switchyard
systemwide
thermo-mechanical
thermo-plastic
thermo-responsive
thermosyphon
time-frame
time scale
time-saving
time-stamp (noun and verb)
timeline
timesaving (adj and noun)
tool-set
top level
trade-off
tunable
tune up (verb)
tune-up (adj and noun)
twofold
uniaxial
uninterruptible
un-irradiated
up-mix
uptime
von Mises
waste water (noun)
waveguide
work flow (noun)
work-flow (adj)
workspace

world-leading
X-ray (upper case X)
zigzag (noun or adj)

0.2.11 Double letters

In UK spelling, both ”focussing” and ”focusing” are considered to be correct. In the Design Report we use single ”s” spelling in all cases.

Note the ’double “l” rule for UK English – label becomes labelled, travel becomes travelled, et cetera. Not so with U.S. English in the Design Report.

0.2.12 Mathematical symbols, subscripts and superscripts

Mathematical symbols are written in math-mode, even when they are embedded in text. For example, a longitudinal dimension L is often called a length. Descriptive subscripts and superscripts, as in L_{acc} or $L^{overhead}$, are not written in Roman font. They appear to be italics, no matter how long or short they are.

0.2.13 Quotation marks

LaTeX is fussy about some things, like quotation marks. Sooner or later an author, a chapter editor, or a general editor must pay attention. This the correct way to put “a certain piece of text” inside quotation marks. The following ”certain piece of text” is incorrect.

0.2.14 Citations, references and the bibliography

Please use inspire hep bibtex entries and notation whenever possible.

Don’t use a “pointer” (for example [4]) in place of naming a reference [2]. That is, use “Joe Blow [4] describes thus and such,” NOT, “[4] describes thus and such”. There should be a space in the text before the citation, so “Joe Blow[4]” is wrong. Multiple citations should be placed with the same square brackets. In the LaTeX vernacular, use `Joe Blow~\cite{Blow2011}` or `Joe Blow~\cite{Blow2011,Smith2012}`.

We are using `bibtex` to handle the references, which are gathered into one `bib` file per chapter, although all references appear in a single bibliography at the end of the Design Report.

During the editing process we are (currently by default) using the LaTeXpackage `showkeys`, which flags references (to Tables, Figures, sections and subsections) and citations (to references) above the text, or in the margin. This should aid in generating cross-references, for example, even though it is rather ugly. It will be turned off in the final stages of editing, before printing. (Comments and feedback, please!)

0.2.15 Miscellaneous

0.2.15.1 "Calculations show that . . . "

This usage, with no indication who carried out the calculations, provides no way for a reader to check the work, or to build upon it in the future. Citations of internal documents, or of individuals to contact to get more information would be helpful for readers, and would also convey a greater sense of credibility. For example, "Relativistic Heavy Ion Collider (2021), unpublished calculations by members of the XYZ working group. Contact Sven Larsson (sven.larsson@bnl.gov) for details."

0.2.15.2 "Should", "must", and reference to future studies

In general, authors should convey the conviction that EIC will do what it should do. In those cases where there is an ongoing internal debate, the Design Report should convey the sense that such debates will be resolved on the basis of a reasoned and careful assessment of the evidence. Only write about future studies in those limited cases where it is needed to show "that we know what we are doing".

0.2.15.3 "Enable"

Incorrect usage:

> "Neutrons pass easily through most materials, enabling the study of large or bulk samples and buried interfaces."

Correct usage:

> "In addition, as the BLM system will be a major tool for beam tune-up, it should also be designed in a way that enables it to pin-point the loss location as precisely as possible."

The point is that the direct object of enable is made capable of doing something – roughly a synonym for empower. You enable the direct object to do something (enable it to pin-point . . .). You could rewrite the first sentence to say, "enabling the study of large or bulk samples . . . to take place." Then it would be correct – although more unwieldy than just saying "making possible the study of . . . "

0.2.15.4 Reporting technical results without a clear statement of their import

In general, it is a mistake to assume that "the numbers speak for themselves". Using words to summarize the meaning of results helps readers to understand them; it also signals that the authors understand the implications of the results they report.

0.2.15.5 Excessive and inconsistent use of lists

Sometimes the use of lists is appropriate, but often there are too many in a draft. Authors should rework most lists into narrative form. For the remaining lists, authors should follow editorial guide-lines to ensure consistent style across the entire Design Report.

After minimizing the number of lists, Design Report editors will convert most of the remaining lists to enumerated lists. The first letter of each item will be upper case, even when the items in the list are not formulated as complete sentences. Items will generally end with a semi-colon unless the phrases are very short, in which case a comma will be used. The last item in the list will be followed by a period. In those cases in which each item in a list consists of multiple sentences, items will be ended with a period.

0.2.15.6 Cross-references

Should be added throughout the whole Design Report, but only down to `\subsection` level, so that cross-references can be found and numbered in the Table of Contents. This implies that subsections should be reasonably balanced in length – not too many pages long.

0.2.15.7 Isotopes

Write ^{3}He, for example, not 3He or He-3.

0.2.15.8 *** asterisks in comments

Sometimes a comment is inserted in a sentence, perhaps indicating that something needs to happen later, such as add a value, a citation, or more text. In this case please include (at least) 3 asterisks in a row *** so that text searches (for example `grep *** *.f`) are made easier. ALSO CONSIDER WRITING IN UPPER CASE***.

0.3 Dimensions and units

Systeme Internationale (SI) units will be used wherever possible. For example, use MPa instead of bar. Some exceptions are inevitable, for example Kilpatrick units. Unusual units should be briefly explained, on their first introduction.

When in doubt, the `siunitx` package does the Right Thing, for example using:

- `\si{\units}` lower case si
- `\SI{numbers}{\units}` upper case SI

A longitudinal dimension – or length – L should be written in one of these ways:

- $L = 100$ m `$L = 100$~m`
- $L = 100$ µm `$L = 100$~\si{\micro\metre}`
- $L = 100\,\mathrm{km}$ `$L = $ \SI{100}{km}`
- $L = 10^2\,\mathrm{km}$ `$L = $ \SI{e2}{km}`

so that the dimension (“m” or “μm” or “km”) is not in italics, and is separated from the numerical value by a non-breakable space – for example “`~`” in LaTeX vernacular. Do not write $L = 100$m, 100m or 100 m. Note that text and mathematical equals signs are different in length (= and $=$): always use the latter.

Powers of ten are written in one of these ways:

- 3.14×10^{39} `$3.14 \times 10^{39}$`
- 3.14×10^{39} `\SI{3.14e39}{}`

Complex dimensions may be written in one of these ways:

- $F = 42\ \mathrm{J\ cm^{-2}\ s^{-1}}$ `$F = 42$~J cm$^{-2}$ s$^{-1}$`
- $F = 42\,\mathrm{J\,cm^{-2}\,s^{-1}}$ `$F=$ \SI{42}{J.cm^{-2}.s^{-1}}`

Exceptionally, percentages are written without a space – 42% is correct but 42 % is not. In LaTeX vernacular a `%` sign is the beginning of a comment, so it is necessary to say `\%` . . .

Temperatures are written as 273 K or 100°C or 101°C, without a space between the number and the °C unit symbol.

Angles are preferably written $\theta = 7.5$ degrees, although 7.5° is acceptable.

0.4 Numbering – chapters, sections, and subsections

In the `\documentclass{report}` style, a “section” (such as this, with the numeric label 0.4) has two numbers associated with it.

0.4.1 This is the heading of a subsection

A “subsection” (like this, 0.4.1) is labelled by 3 numbers, namely “chapter_number.section_number.subsection_number”. Sections and subsections begin with a bold face font.

0.4.1.1 A subsubsection heading like this has no period at the end

In bold font, it has no numerical label, and sits separately from the text that immediately follows, even if there is no white space between `\subsubsection{}` and the first word of the text. It does not appear in the Table of Contents.

This paragraph heading ends with a period. Subsequent text remains in the same paragraph. The editors will use their judgement to prevent the excessive use of paragraph headings and boldface text.

0.4.2 More formatting rules and standards

0.4.2.1 Clearpages and Pagebreaks

As a rule there is NO `\clearpage` or `\pagebreak` before a new section (or subsection), and hence no white space.

0.5 Equations, Tables, Figures, and plots

0.5.1 Equations

Start with a simple equation, like Equation 1:

$$H = \frac{\sqrt{3\left\langle x^4\right\rangle\left\langle x'^4\right\rangle + 9\left\langle x^2x'^2\right\rangle^2 - 12\left\langle xx'^3\right\rangle\left\langle x^3x'\right\rangle}}{2\left\langle x^2\right\rangle\left\langle x'^2\right\rangle - 2\left\langle xx'\right\rangle^2} \tag{1}$$

Avoid ending a sentence with an equation, in order to avoid deciding whether or not to put a period after the equation.

Here is a simple equation array:

$$\begin{aligned} M_{virg}(\sigma) &= M_{virg0} + k_{virg}.\sigma \\ M_{rel}(\sigma) &= M_{rel0} + k_{rel}.\sigma \end{aligned} \tag{2}$$

0.5.2 Tables

- Table 1 is a relatively complicated multi-column table, while Table 2 is a standard 3-column parameter table.
- Table 3 shows how to make a table exportable, for example to the Parameter Tables appendix.
- The source text for Table 4 shows how to enable text filling in columns.
- Table 5 shows 2 ways to squeeze tables, with the `\scalebox{}` and `\phantom{}` commands.
- Table 6 shows a third way, using `\tabcolsep{}`.

The vertical spacing of Table rows is set in “preamble.tex” by the line `\renewcommand{\arraystretch}{1.0}`.

0.5.3 Converting between LaTeX and Excel table formats

More than one free utility enables table conversion with a drag-and-drop interface. E.g.:

Excel to LaTeX try `https://tableconvert.com/excel-to-latex`

LaTeX to Excel try `https://tableconvert.com/latex-to-excel`

Facility	Location	Status	First oper.	Power [MW]	Instruments	Integrated flux [10^{14}cm^{-2}]	Peak flux [10^{15}cm^{-2}s^{-1}]
ESS	Lund	Pre-constr.	2019	5	22	–	40
J-PARC	Tokai	Re-furbish	2009			–	

Table 1: A standard Table looks like this, using "toprule", "midrule" and "bottomrule" separation lines.

Parameter	Unit	Value
Energy	GeV	2.5
Current	mA	50
Pulse length	ms	2.86
Pulse repetition frequency	Hz	14
Average power	MW	5
Peak power	MW	125

Table 2: Long version of caption for top-level parameters.

Parameter	Unit	Value
Energy	GeV	2.5

Table 3: A parameter table made available for export, for example to Appendix E "Parameter Tables", using input from a /Tables subdirectory file.

System	Subsystem	Test
Target	Shaft and drive	Run at up to 25 Hz.
	Target segments	Leak test at pressure.
	Target Safety System	Demonstrate trip signals generated for all defined cases.
Primary helium loop	Pump, heat exchanger, filter	Pressure and flow tests without target.
	Full loop with target	Full operational test without heat.

Table 4: A table with fixed third column width, enabling text filling.

Nuclide	Decay time [years]						
	0	6	40	100	1000	10^4	10^5
^{3}H	0.9	83.4	96.4	72	0	0	0
^{14}C	0	0	0	0	0.3	0.6	0
^{36}Cl	0	0	0	0	0	0	0.7
^{39}Ar	0	0	0	0.1	0.7	0	0
^{154}Dy	0	0	0	0	0	0.2	4.3
^{163}Ho	0	0	0	0.7	29.7	53.4	0

Table 5: Two ways to squeeze tables, with the "scalebox" and "phantom" commands.

Nuclide	**Decay time** [years]						
	0	6	40	100	1000	10^4	10^5
^{137}La	0	0	0	0	1.4	8.7	57.6
^{148}Gd	0	0.2	0.9	11.6	0.1	0	0
^{150}Gd	0	0	0	0	0	0.3	5.6
^{154}Dy	0	0	0	0	0	0.2	4.3
^{157}Tb	0	0.1	0.6	9.3	7.2	0	0
^{154}Dy	0	0	0	0	0	0.2	4.3
^{163}Ho	0	0	0	0.7	29.7	53.4	0

Table 6: A third way to squeeze tables, with the "tabcolsep".

0.5.4 Figures

Many figures, like Figure 1, are non-graphical images – perhaps a photograph, drawing or sketch.

Figure 1: This is an example of a non-graphical figure. We need to address the means by which we can give "all" graphs the same look and feel.

0.5.5 Plots

It is clear that for the ePIC detector sections we will mostly be using ROOT and Python, while the accelerator team most likely will be using a different package; so as soon as a figure style is agreed on, we will need to make style packages for ROOT and Python so all figures in the manuscript look stylistically the same.

As teams develop initial plots, please be sure to each the codes available so that they can be remade in a common style.

0.6 Italics and bold face type

In general, retsrain the use of *italics* and **bold face**.

Long quotations will be set in italics. Italics will also be used (sparingly) for traditional purposes of emphasis (e.g. "when she was good, she was *very* good.")

Occasionally, authors wish to draw attention to the subject matter being addressed in a block of text. Usually, this should be done by headings and subheadings. In those limited instances in which use of altered type face is appropriate within the body text, the editors will use bold face, rather than italics. One such situation is for short introductory phrases at the beginning of paragraph-long items in an enumerated list.

0.7 Issues that this Style Guide does not yet address

This Style Guide addresses “consistency of style” issues. Here is a numerical list of issues that could or should be significantly expanded:

1. the use of pronouns
2. specialized terminology
3. acronyms
4. the use of italics
5. the use of digits (e.g. 1) where written numbers are more appropriate
6. the overuse of capital letters (Boron vs. boron, User vs. user, etc.).
7. balancing the length of sections and subsections
8. global glossary
9. Lists
10. Plots (see placeholder 0.5.5)

Chapter 2

Physics Goals and Requirements

2.1 EIC Context and History

Add the EIC context and history here.

2.2 The Science Goals of the EIC and the Machine Parameters.

Add the science goals of the EIC and the machine parameters here.

2.3 Scientific Requirements

2.3.1 Systematic Uncertainties

Add text here.

2.3.2 Radiative Corrections

Add text here.

2.4 The EIC Science (ePIC performance for key observables)

2.4.1 Origin of Nucleon Mass

Add text here.

2.4.2 Origin of Nucleon Spin

Add text here.

2.4.3 Multi-Dimensional Imaging of the Nucleon

2.4.3.1 Imaging in Momentum Space

Add text here.

2.4.3.2 Imaging in Transverse Position Space

Add text here.

2.4.4 Properties of Nuclear Matter

2.4.4.1 Gluon Saturation

Add text here.

2.4.4.2 Nuclear Modifications of Parton Distribution Functions

Add text here.

2.4.4.3 Passage of Color Charge Through Cold QCD Matter

Add text here.

Chapter 8

Experimental Systems

8.1 Experimental Equipment Requirements Summary

The YR table (Fig. 8.1) is being reviewed and an updated table with accompanying text will be included in the draft Version1.

Table 10.6: This matrix summarizes the high level requirements for the detector performance. The interactive version of this matrix can be obtained through the Yellow Report Physics Working Group WIKI page (https://wiki.bnl.gov/eicug/index.php/Yellow_Report_Physics_Common).

η	Nomenclature			Tracking				Electrons and Photons			π/K/p		HCAL		Muons
				Resolution	Allowed	minimum-pT	Si-Vertex	Resolution σE/E	PID	min E	p-Range	Separation	Resolution σE/E	Energy	
-6.9 to -5.8			low-Q2 tagger	σθ/θ < 1.5%; 10-6 < Q2 < 10-2 GeV2											
-5.0 to -4.5						300 MeV pions									
-4.5 to -4.0			Instrumentation to separate charged particles from photons			300 MeV pions		2%/√E(+1-3%)		50 MeV					
-4.0 to -3.5	↓ p/A	Auxiliary De								50 MeV			~50%/√E + 6%		
-3.5 to -3.0			Backward Detector							50 MeV					
-3.0 to -2.5				σpT/pT ~ 0.1%⊕0.5%			σ_xy~30/pT µm +40 µm		π suppression up to 1:1E-4	50 MeV	≤ 7 GeV/c		~45%/√E+6%		muons useful for bkg. improve resolution
-2.5 to -2.0				σpT/pT			σ_xy~30/pT µm +20 µm	2%/√E(+1-3%)		50 MeV					
-2.0 to -1.5				σpT/pT 0.05%⊕0.5%				7%/√E(+1-3%)		50 MeV					
-1.5 to -1.0								7%/√E(+1-3%)		50 MeV					
-1.0 to -0.5			Barrel	σpT/pT ~0.05%×pT+0.5%	~5% or less X		σxyz ~ 20 µm, d0(z) ~ d0(rφ) ~ 20/pTGeV µm + 5 µm			50 MeV	≤ 10 GeV/c	≥ 3σ			
-0.5 to 0.0		Central Detector								50 MeV			~85%/√E+7%	~500 MeV	
0.0 to 0.5										50 MeV			~85%/√E+7%		
0.5 to 1.0										50 MeV	≤ 15 GeV/c		~85%/√E+7%		
1.0 to 1.5			Forward Detectors	σpT/pT ~0.05%×pT+1.0%		<100MeV pions, 135MeV kaons	σ_xy~30/pT µm +20 µm		3σ e/π	50 MeV	≤ 30 GeV/c		35%/√E		
1.5 to 2.0										50 MeV	≤ 50 GeV/c				
2.0 to 2.5										50 MeV					
2.5 to 3.0				σpT/pT ~ 0.1%×pT+2.0%			σ_xy~30/pT µm +40 µm	(10-12)%/√E(+1-3%)		50 MeV	≤ 30 GeV/c				
3.0 to 3.5							σ_xy~30/pT µm +60 µm			50 MeV	≤ 45 GeV/c				
3.5 to 4.0			Instrumentation to separate charged particles from photons	Tracking capabilities are desirable for forward tagging						50 MeV					
4.0 to 4.5	↑ e	Auxiliary Detectors								50 MeV			35%/√E (goal), <50%/√E (acceptable)*, 3mrad/√E (goal)		
4.5 to 5.0			Neutron Detection			300 MeV pions		4.5%/√E for photon energy > 20 GeV	<= 3 cm granularity	50 MeV					
> 6.2			Proton Spectrometer	σintrinsic(|t|)/|t| < 1%; Acceptance: 0.2 < pt < 1.2 GeV/c											

Figure 8.1: Table presenting the Experimental Equipment Requirements Summary in the YR. At present, the table is not updated and it is here as a mere space holder.

8.2 General Detector Considerations and Operations Challenges

8.2.1 General Design Considerations

This section will discuss the detector challenges with cross-reference to the appropriate sections. The Sec.s to refer to are related to machine parameters (not in chapter 8), 8.1 “Experimental Equipment requirement Summary”, 8.2.2 ”Background and Rates” and 8.2.3 ”Radiation Level”. At present, all these sections are not available. Therefore, for Version0, a mere list of topics that will be covered is provided.

Discussion of challenges related to:

- Physics requirements (ref. to Sec. 8.1);
- Beams rates, polarization, luminosities (ref. to Sec.s in the machine chapters);
- Integration with the machine and hermeticity (ref. to Sec.s in the machine chapters, ref. to Sec. 8.1);
- Rates and multiplicity (ref. to Sec.c in the machine chapters, to Sec. 8.2.2);
- Radiation hardness (Ref. to Sec. 8.2.3).

8.2.2 Backgrounds and Rates

Add text here.

8.2.3 Radiation Level

Add text here.

8.3 The ePIC Detector

8.3.1 Introduction

The Context The development of the EIC science and the experimental equipment required to successfully implement the science as documented in the NSAC and NAS reports has been driven by an international EIC community, formalized in 2016 in the EIC User Group [3], at present (September 2024) formed by more than 1500 members from almost 300 institutions and 40 countries. Several conceptual general-purpose detectors had been elaborated. A next step effort was required by the EIC project approval with the signature of CD0 in December 2019. The User Group engaged in advancing the state of documented physics studies, which dictate the detector requirements, and consolidate the general-purpose detector concept matching these requirements. This effort resulted in the EIC Yellow Report completed in early 2021 and then published in Nuclear Physics A [4]. This document guided the two proposals for a general-purpose detector elaborated in 2021, which resulted in further progress in the conceptual detector design. In 2022, a merging process of the communities presenting the two proposals and of the two conceptual approaches resulted in the formation of the ePIC Collaboration [5] (July 2022) and in baselining of the ePIC detector as EIC project detector. At present (September 2024), ePIC has more than 850 members from 177 Institutions and 25 countries, confirming the international vocation of the community pursuing the EIC science and detector.

The Detector THIS DETECTOR DESCRIPTION IS AN INTRODUCTION TO THE WHOLE SECTION 8.3. IT WILL BE REVISED WHEN THE SUBSYSTEM MATERIAL IS UPLOADED TO ENSURE A BETTER CONSISTENCY OF THE SECTION 8.3.

The detector challenges and the technologies matching these challenges are discussed in Sec. 8.2.1. The resulting design of the ePIC detector consists in a Central Detector (CD) surrounding the Interaction Point 6 (IP6) making optimal use of the space available at the Interaction Region (IR) complemented by equipment situated along the outgoing beam lines, the Far Detectors (FD), which complete the phase-space coverage.

Figure 8.2 illustrates the CD kinematic coverage; Fig. 8.3 presents a schematic overview of the CD structure. The overall CD length is imposed by the constrain of the IR design. The asymmetric beam energies reflect in an asymmetric design of the detector and, together with the requirements from physics, imposes the choice of the different detector technologies that have been adopted. The setup is designed around the solenoid providing the magnetic field for the momentum analysis. The adoption of a solenoid shapes the CD in a barrel region where the subsystem have pseudo-cylindrical layouts and two endcap regions, the forward one equipping the region around the outgoing ion beam and the backward endcap around the outgoing electron beam. The barrel subsystems cover, approximately, the pseudorapidity η region (-1.5, 1.5), while the endcaps equip the regions up to pseudorapidity $|3.5 - 4.0|$, the upper bound being dictated by the beampipe layout. The separation in barrel and endcap region is not rigid with exceptions where the optimization of the detector design suggests it. For instance, the most inner layers of the tracking system have acceptance well beyond $\eta < |1.5|$, the barrel Cherenkov PID counter and the barrel electromagnetic calorimeter extends in the backward endcap.

The CD subsystems have a layered structure, from inside to outside: tracking subsystems, particle identification devices, electromagnetic calorimeters, solenoid coils in the barrel, and hadronic calorimeters.

The reference operation condition of the new **MARCO magnet** (Sec. 8.3.2), specifically designed for ePIC, is with 1.7 T field intensity and it can provide up to 2 T. It has good homogeneity in the central region and provides projective field lines in the forward endcap to match the requirements posed by the usage of a gaseous radiator in the forward RICH. The solenoid axis coincides with the electron beam line in the IR to limit the synchrotron radiation from the beam electrons. This results in helicoidal trajectories of the beam ions, due to the crossing angle of the two beams.

The **tracking system** (Sec. 8.3.3) is the most inner subsystem in order to ensure the minimum distortion of the trajectories by the material crossed by the particles. It consists of pseudo cylindrical layers completed by discs in the endcaps. The low material budget (Fig. 8.4) is guaranteed by the selected tracker technologies, with the thin ITS3 MAPS, even in support-less arrangement in the most inner layers, and MPGDs for the most external layers. The two tracker technologies support each other thanks to key complementary characteristics. MAPS sensors offer extremely fine space resolution, but poor timing information in the order of a few microsecond range. In-time hits can be selected combining MAPS information with the measurements in the MPGDs, which have time resolution of 10-20 ns. Further space and time information will be provided by the time-of-flight layers in the barrel and the forward endcap and by the first layer of the barrel imaging electromagnetic calorimeter equipped with AstroPix MAPS sensors. The minimization of the material budget

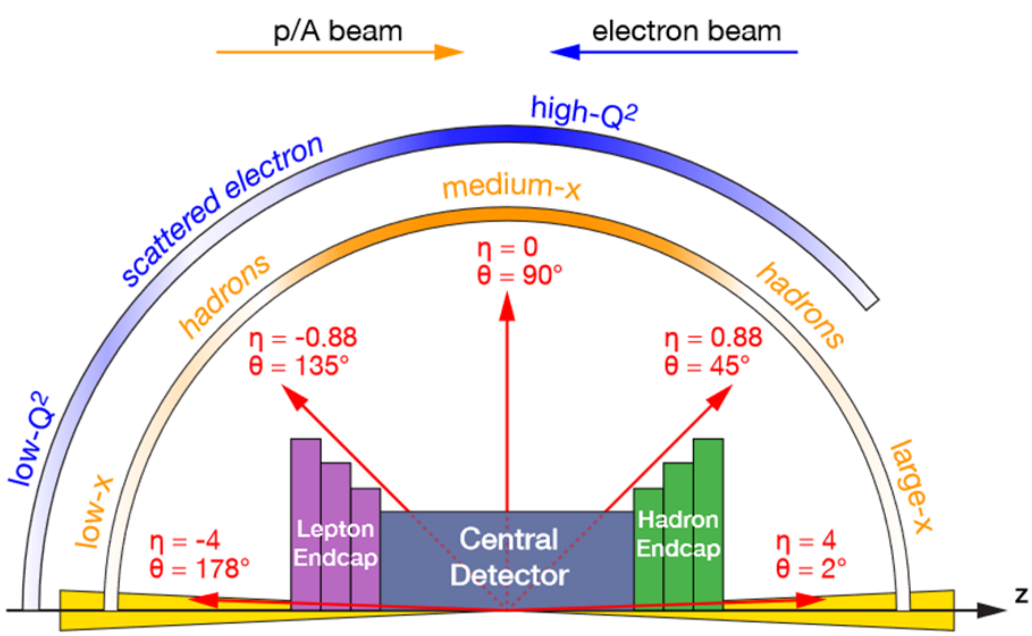

Figure 8.2: A schematic showing how hadrons and the scattered electron for different x - Q^2 are distributed over the detector rapidity coverage. THIS FIGURES IS A PLACE HOLDER: IT IS FROM YR AND REQUIRES REVISION.

is one of the ingredients allowing fine resolution for momentum determination and vertex reconstruction. To this end, fine intrinsic resolution is requested for the trackers and it is provided by the ITS3 MAPS. The momentum resolution is affected by the available lever arm and the solenoidal configuration of the magnetic field, the latter having its largest impact on the very forward and backward trajectories.

The tracking information is also a key ingredient for the performance of the Cherenkov imaging devices; in particular, very fine resolution of the particle direction is needed for the barrel DIRC. The most external tracker layers in the barrel, positioned in front of the DIRC, further support this requirement.

The **particle identification subsystems** (Sec. 8.3.4) surround the tracking systems. Their mission is twofold: (i) supporting the electromagnetic calorimeters by complementing the pion/electron separation to ensure the high purity of the electron sample; (ii) identifying hadrons, as needed by a large fraction of the physics program. The coverage of the wide kinematic domain imposes the adoption of a variety of technologies with time-of-flight measurements complementing Cherenkov imaging devices. Time-of-flight dedicated layers by AC-LGADs are present in the barrel and in the forward endcap, the barrel layer being by strip sensor elements to reduce the material budget, while the forward endcap layer is by pixelized AC-LGADs. In the backward endcap, the fine time-resolution provided by the photosensors of the Cherenov counter, which are sitting in the endcap acceptance, provide timing information via the Cherenkov light generated in the sensor window. The Cherenkov imaging counter in the backward endcap is a proximity focusing RICH with aerogel radiator and extended proximity gap to increase the resolution and, correspondingly, enlarging the momentum range for particle identification. As already underlined, the use of fine-time resolution HRPPDs by MCP technology as photosensors also provides timing information.

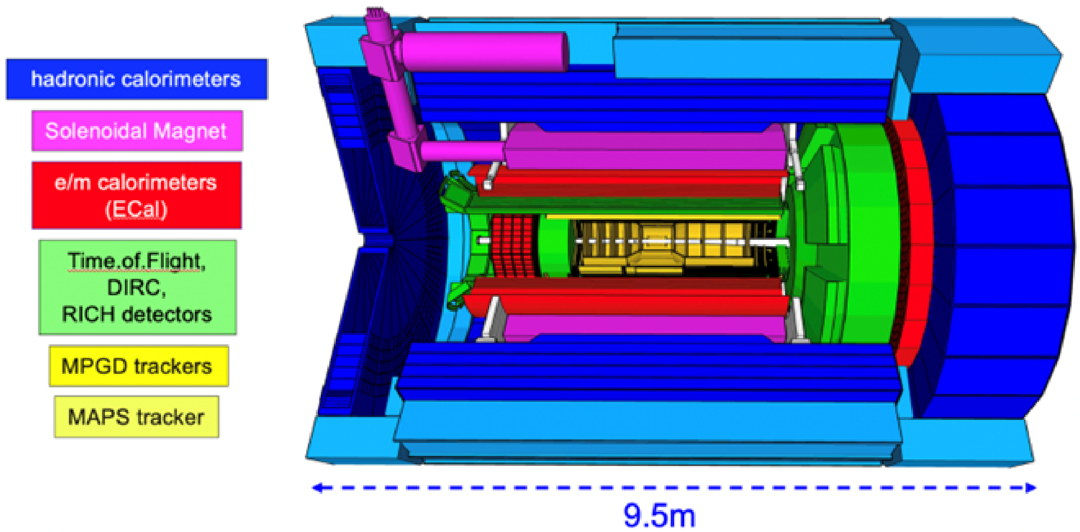

Figure 8.3: A schematic showing the ePIC central detector subsystems. THIS FIGURES IS A PLACE HOLDER

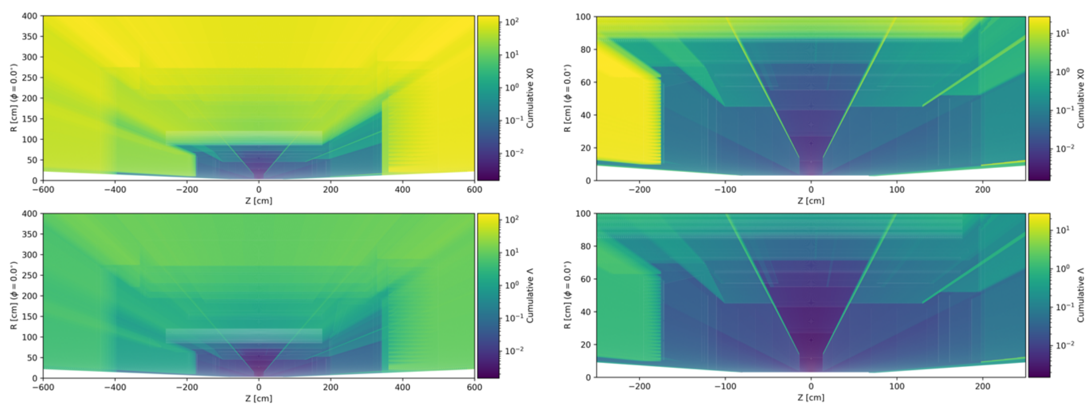

Figure 8.4: Cumulative material budget in radiation lengths (top row) and interaction lengths (bottom row) for the whole CD (left column) and zooming at the CD tracking region (right column). THIS FIGURES IS A PLACE HOLDER BECAUSE IT HAS TO BE COMPLETED WITH SUBSYSTEM CONTOURS AND REQUIRES GRAPHICAL IMPROVEMENTS.

The whole detector components are positioned in the acceptance, in front of the electromagnetic calorimeter. This layout is compatible with the overall detector design; in fact, the bulky elements, namely the sensors with readout electronics and services are just in front of the calorimeter acting as a pre-shower element. In the barrel, a high performance DIRC is used, this choice being dictated by the reduced space. The DIRC fused silica bars, acting as radiator and as photon lightguides, make possible positioning the image expansion elements and the read-out electronics with its services in the backward region, outside the acceptance cone. The dual radiator RICH (Sec) in the forward endcap is equipped with two radiators, aerogel and gas, therefore acting as a couple of Cherenkov imaging counters dedicated to particle identification in two different momentum ranges, while economizing in space and single photon sensors. It is a focusing RICH with spherical mirrors as focusing elements. The photosensors and related services are placed outside the acceptance thank to appropriate mirror orientation.

The electromagnetic calorimeters (Sec. 8.3.5) are external to the particle identification devices and, once more, the different technologies are imposed by the physics requirements, the kinematic ranges and the overall constrains. The budget of the material in front of the calorimeters is low and mainly concentrated near to the calorimeter front face. The backward endcap electromagnetic calorimeter is by fine granularity lead tungstate crystal offering very fine energy resolution. In the barrel, the electromagnetic calorimeter has a hybrid architecture combining imaging layers by AstroPix MAPS and sampling calorimetry by lead and scintillating fibers with sampling layer between the imaging layers and in the most external calorimeter portion. The layout is pseudo cylindrical with the read-out equipment at the cylinder edges minimizing the space requirement in the crowded barrel area. The electromagnetic calorimetry in the forward region is by sampling calorimetry with scintillating fibers inserted in matrices of tungsten powder embedded in epoxy. This calorimeter offer a near to 1 ratio of the signal amplitude response for electrons and hadrons and, therefore, it is design to operate in duet with the hadronic calorimeter place immediately behind.

All the **hadron calorimeters** (Sec. 8.3.6) are by iron as converter and scintillating active elements, even if with very different implementations. The forward endcap calorimeter is by SiPM-on-tile technology, with finer granularity in the central zone, near to the beam pipe, to cope with the higher rates. The barrel calorimeter, placed behind the solenoid coils, acts as a tail catcher. The backward endcap calorimeter . . . (to be completed: layout in evolution).

All the calorimeter subsystem in the ePIC detector make use of SiPMs as photosensors, even if of different size and pixelization, with common approach for the readout chain.

The global layout of the FDs (Sec.s 8.3.7 and 8.3.8) is illustrated in a artistic view in Fig. 8.5.

The **forward FDs** include tracking and electromagnetic calorimetry inserted in the first dipole of the ion beam line B0, off-momentum detector trackers and roman-pot trackers and a zero-degree-calorimeter. The technology for the trackers is by AC-LGADs, which have good radiation hardness. The B0 electromagnetic calorimeter is by lead tungstate crystals. The zero-degree-calorimeter is formed by a long SiPM-on-tile module with fine granularity adequate for photon and neutron detection. A crystal layer can be inserted in front of it for those studies that require the detection of low energy photons.

The **luminosity system** is part of the backward FD. Based on the measurement of the photons from the Betha-Heitler process at IP, it consists of a high-rate calorimeter for direct photon detection and a couple of pair spectrometers to detect the electrons and positrons generated by the Betha-Heitler photons in the exit window. The high-rate calorimeter and the calorimeters in the pair spectrometers are by tungstate and scintillating fibers. Tracking in the pair spectrometer is by AC-LGADs. The **low-Q**^{2} taggers consist in tracking stations followed by an electromagnetic calorimeter. The selected technologies must cope with extremely high rate in this kinematic region. Therefore, tracking is by TimePix4 and calorimetry by tungstate and scintillating fibers.

Integral elements of the detector are the **electronic read-out chain**, the data acquisition system (Sec. 8.3.10) and the **software implementation and computing model** (Sec. 8.3.11). The overall underlining model that has guided the selection of the components and the design of the read-out/DAQ/software/computing architecture is the streaming readout concept. Streaming readout has been selected to simplify the readout scheme as no triggers are required and to increase the information selection flexibility, to improve the event building from the holistic detector information, to improve, via continuous dataflow, the knowledge of backgrounds and, therefore, enhances the control over systematics. In this approach, already at the front-end level, the ASICs, which

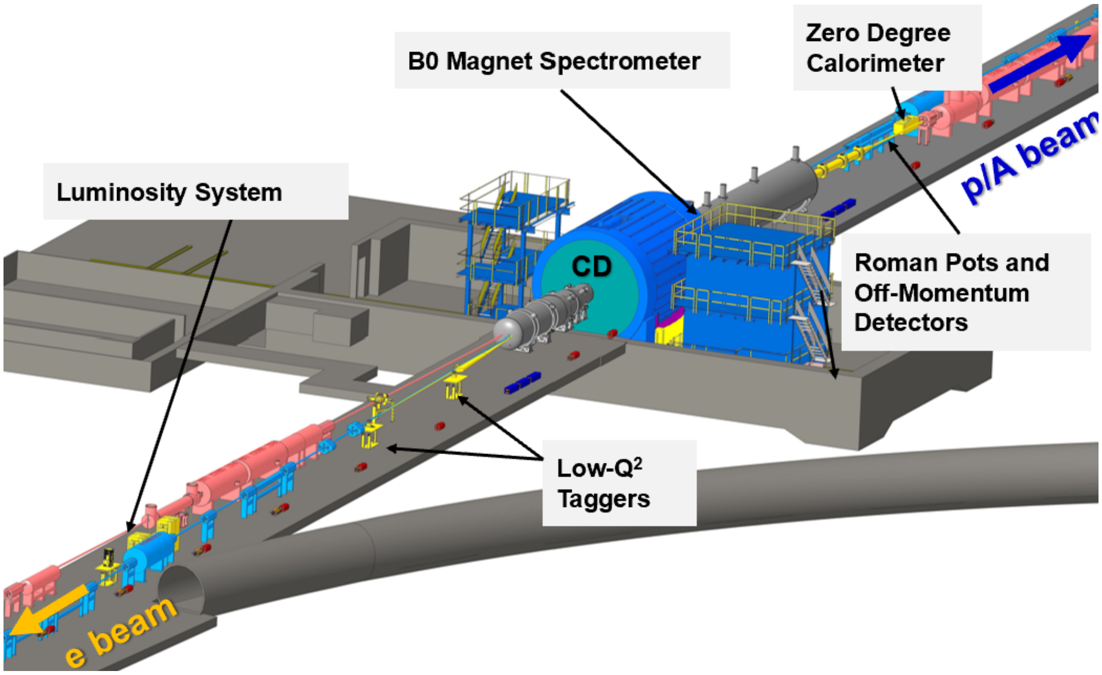

Figure 8.5: A schematic showing the ePIC far detector subsystems. THIS FIGURES IS A PLACE HOLDER

are intimate related to the sensors and their performance, have been selected with architectures compatible with their usage in streaming readout mode.

Independent setups are designed to measure and monitor the **beam polarization** (Sec. 8.3.9). Rapid, precise beam polarization measurements will be crucial for meeting the goals of the EIC physics program as the uncertainty in the polarization propagates directly into the uncertainty for relevant observables as asymmetries. The basic requirements for beam polarimetry are non-destructive with minimal impact on the beam lifetime, uncertainty at the 1% level, the capacity of measuring the beam polarization for each bunch in the ring with rapid, quasi-online analysis in order to provide timely feedback for accelerator setting up. The electron beam polarimetry will be based on the well established Compton polarimeter techniques, where the polarized electrons scatter from 100% circularly polarized laser photons. This approach offers the advantage that both longitudinal and transversal polarizations are measured. Hadron polarimetry has been successfully performed on RHIC polarized proton beams for nearly two decades. Through continual development a relative systematic uncertainty ¡1.5% was achieved for the most recent RHIC polarized proton run. As the only hadron polarimeter system at a high energy collider it is the natural starting point for hadron polarimetry at the EIC. Hadron polarization will be measured via a transverse single spin left right asymmetry in the pp interaction on targets by plastic material (H-C composition), where the experimental challenge is the control of the background events.

Technological Synergistic Aspects of the Detector Design The synergistic aspects of the ePIC detector have been carefully maximized in view of the optimal usage of the workforce and the financial resources. This is illustrated by the following examples.

SiPM sensors, recently introduced in calorimetry applications, are adopted for all the electromagnetic and hadronic calorimeters in ePIC. They offer a cost-effective technology that can operate in magnetic field, can provide wide dynamic range when the sensor type is properly chosen to tune the response parameters, and present low noise level by applying appropriate thresholding. The use of a common technology makes possible to access the effect of the radiation by a single effort and the use of the same front-end ASIC CALOROC.

Also the calorimetry reconstruction software is synergistic for the overall set of subsystems.

In electromagnetic calorimetry, the sampling approach with tungsten and scintillating fiber is adopted for the forward endcap calorimeter and in FDs: calorimetry in B0, luminosity system and low-Q^2 taggers.

In hadron calorimetry, the SiPM-on-tile technology is used for the forward endcap calorimeter and its insert in the central area, as well as for the zero-degree calorimeter.

In particle identification by Cherenkov imaging counters, MCP-based photosensors are used for the backward endcap RICH and the barrel DIRC, that can be read by the same read-out ASIC HGCROC (information to be crosschecked). The backward endcap RICH and the forward endcap RICH use aerogel as radiator and the quality assessment station will be used for both batches. The reconstruction software in both RICHes has large communalities and it is based on the same ray-tracing algorithm.

AC-LGADs form the time-of-flight layers and are used for tracking in the forward FD in B0, off momentum detectors and roman pots, and selected for the pair spectrometers of the luminosity system.

In tracking by MAPS, the different sensors of the inner layers, the outer layers and the forward and backward disks are all evolutions of the ITS3 sensor, therefore all based on stitching the same readout chip element.

The same hybrid MPGD architecture with a preamplifying GEM layer followed by a μRWELL is used in the most outer tracker in the barrel and the most external discs in the endcaps. All MPGDs, namely the hybrid MPGDs and the cylindrical Micromegas in the barrel are coupled to the same front-end ASIC: SALSA.

A single integrated effort is at the basis of the tracking reconstruction with the use of the software package AC.

8.3.2 Magnet

Requirements

Requirements from physics: Add text here.

Requirements from Radiation Hardness: Add text here.

Requirements from Data Rates: Add text here.

Justification

Device concept and technological choice: Add text here.

Subsystem description:

General device description: Add text here.

Sensors: Add text here.

FEE: Add text here.

Other components: Add text here.

Requirements from Data Rates: Add text here.

Implementation

Services: Add text here.

Subsystem mechanics and integration: Add text here.

Calibration, alignment and monitoring: Add text here.

Status and remaining design effort:

R&D effort: Add text here.

E&D status and outlook: Add text here.

Other activity needed for the design completion: Add text here.

Status of maturity of the subsystem: Add text here.

Environmental, Safety and Health (ES&H) aspects and Quality Assessment (QA planning: Add text here.

Construction and assembly planning: Add text here.

Collaborators and their role, resources and workforce: Add text here.

Risks and mitigation strategy: Add text here.

Additional Material Add text here.

8.3.3 Tracking

Add text here.

8.3.3.1 The silicon trackers

Requirements

Requirements from physics: Add text here.

Requirements from Radiation Hardness: Add text here.

Requirements from Data Rates: Add text here.

Justification

Device concept and technological choice: Add text here.

Subsystem description:

General device description: Add text here.

Sensors: Add text here.

FEE: Add text here.

Other components: Add text here.

Performance

Implementation

Services: Add text here.

Subsystem mechanics and integration: Add text here.

Calibration, alignment and monitoring: Add text here.

Status and remaining design effort:

R&D effort: Add text here.

E&D status and outlook: Add text here.

Other activity needed for the design completion: Add text here.

Status of maturity of the subsystem: Add text here.

Environmental, Safety and Health (ES&H) aspects and Quality Assessment (QA planning: Add text here.

Construction and assembly planning: Add text here.

Collaborators and their role, resources and workforce: Add text here.

Risks and mitigation strategy: Add text here.

Additional Material Add text here.

8.3.3.2 The MPGD trackers

Requirements

Requirements from physics: Add text here.

Requirements from Radiation Hardness: Add text here.

Requirements from Data Rates: Add text here.

Justification

Device concept and technological choice: Add text here.

Subsystem description:

General device description: Add text here.

Sensors: Add text here.

FEE: Add text here.

Other components: Add text here.

Performance

Implementation

Services: Add text here.

Subsystem mechanics and integration: Add text here.

Calibration, alignment and monitoring: Add text here.

Status and remaining design effort:

R&D effort: Add text here.

E&D status and outlook: Add text here.

Other activity needed for the design completion: Add text here.

Status of maturity of the subsystem: Add text here.

Environmental, Safety and Health (ES&H) aspects and Quality Assessment (QA planning: Add text here.

Construction and assembly planning: Add text here.

Collaborators and their role, resources and workforce: Add text here.

Risks and mitigation strategy: Add text here.

Additional Material Add text here.

8.3.4 Particle identification

Add text here.

8.3.4.1 The time-of-flight layers

Requirements and Justifications

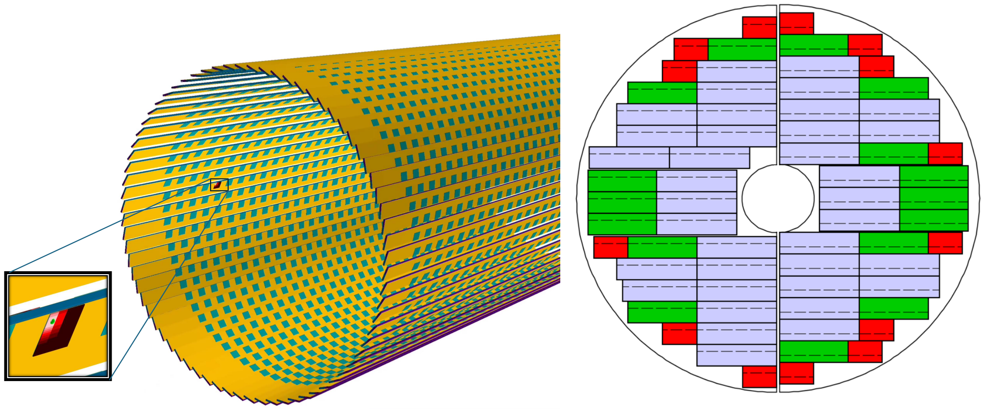

Figure 8.6: Geometries of BTOF with insert of sensor and charge sharing distribution (left), and the layout of sensor modules and service hybrids of FTOF on one side (right).

Requirements from physics: With single hit timing resolution of 35 ps from the Barrel TOF (BTOF) and 25 ps from the Forward TOF (FTOF), the AC-LGAD TOF detector system can provide particle identification for low momentum charged particles, e.g., π-K separation at the 3σ level for $p_T < 1.2$ GeV/c for $-1.2 < \eta < 1.6$, and $p < 2.5$ GeV/c for $1.9 < \eta < 3.6$, respectively. By combining the PID information for low momentum particles from the TOF detectors and high momentum particles from Cherenkov detectors, ePIC will have excellent PID capability over a wide momentum range in a nearly 4π acceptance, which is crucial to achieve the goals of the EIC physics program. Besides precise timing resolution, AC-LGAD sensors can also provide precise spatial resolution, and thus aid track reconstruction and momentum determination. The requirements on the timing and spatial resolutions, as well as the material budgets are being evaluated in ePIC MC simulation to find the optimal configuration without over-designing these detectors. Table 8.1 summarizes the current specifications of the timing and spatial resolutions, material budgets, the covered area, channel counts and dimensions. Figure 8.6 shows the BTOF and FTOF layouts with an insert showing charge sharing on a sensor. Figure 8.7 shows the performance of the TOF detector in the form of $1/\beta$ as a function of particle momentum p for ep DIS events from PYTHIA+GEANT4 simulation. Together with the other PID detectors, we are able to demonstrate that the ePIC PID performance which includes the TOF detectors as one of the integral components meets the requirements.

Subsystem	Area (m^2)	dimension (mm^2)	channel count	timing σ_t (ps)	spatial σ_x (μm)	material budget (X_0)
Barrel TOF	12	0.5*10	2.4M	35	30 ($r \cdot \phi$)	0.015
Forward TOF	1.1	0.5*0.5	3.2M	25	30 (x, y)	0.05

Table 8.1: Required performance for physics and proposed configurations for the TOF detector system.

Requirements from Radiation Hardness: The radiation fluence and dose at ePIC are significantly less than in the LHC experiments. It is safe to assume that the maximum foreseen fluence for the lifetime of the TOF detectors will be $< 5 \times 10^{12}$ n_{eq}/cm^2, as seen in Fig. 8.8 and Tab. 8.2. Here the highest fluence between raw and 1MeV n_{eq}/cm^2 fluence was considered, as the standard NIEL correction is not applicable for some aspects of LGAD radiation damage.

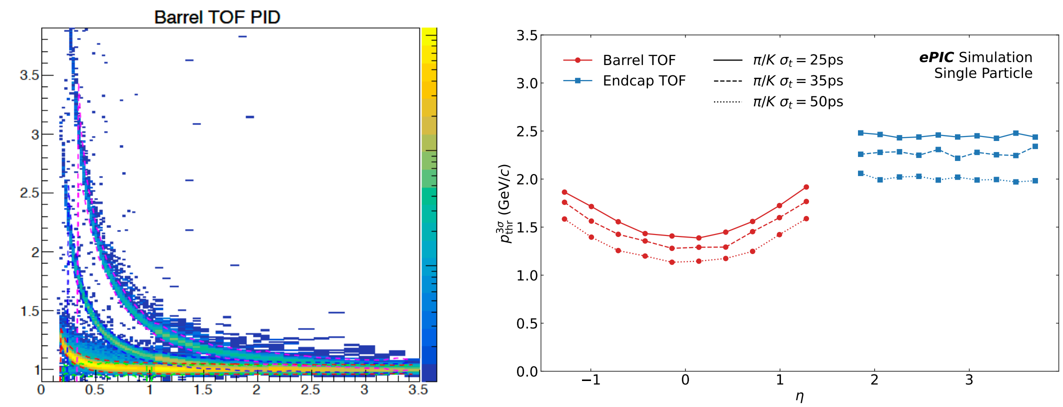

Figure 8.7: BTOF $1/\beta$ as a function of momentum (p) in the simulation performance with PYTHIA DIS events (left). Upper limits on the 3σ particle separation from BTOF and FTOF as a function of pseudorapidity (right).

Much work has been done to characterize and improve the radiation resistance of LGAD gain layers to meet the requirements at the LHC [6] (up to 2.5×10^{15} 1MeV n_{eq}/cm^2). Because of the sensitivity of the sensor performance to the value of the N+ sheet resistance (a feature absent from the conventional LGADs made use of for the LHC), it is possible that AC-LGADs may be significantly less radiation tolerant than their conventional cousins. Indeed, N-type doping is known to be particularly sensitive to hadronic irradiation, with N-bulk sensors inverting to P-bulk before exposure of even 1×10^{14} is accumulated. Furthermore, LHC LGAD detectors are designed to run at -30C to reduce the post-radiation leakage current, while in ePIC, the sensors will be operated at room or slightly lower temperatures for the experiment's lifetime. The leakage current increase due to radiation damage for the fluence in ePIC has to be low enough not to trigger a thermal run-away combined with the power dissipation from the readout chip, especially for the forward and end-cap region where the chips are bump bonded on top of the sensors.

Therefore, a radiation exposure run was performed before the ePIC LGAD design was finalized. Several sensors from HPK and BNL were irradiated at FNAL ITA facility (400 MeV protons) and at the TRIGA reactor in Ljubljana (MeV-scale neutrons) to probe radiation effect from ionizing and non-ionizing particles. The radiation exposure would be done in steps, allowing potential charge-collection pathologies, should they exist, to be mapped out for the development of models and corrections. By studying the sensor performance before and after irradiation, the change in N+ resistivity can be characterized, and this particular risk can be addressed. Sensors irradiated with 1 MeV neutrons were received in the Summer of 2024 and tested; the results are encouraging, as seen in the following sections. Sensors were irradiated at the FNAL ITA facility but are still cooling down from the activation; they will likely be available for testing in early 2025.

Requirements from Data Rates: As the sensors and ASICs differ between the BTOF and FTOF, the rate requirements are presented separately for both of these sub-components. On top of that, the phase space coverage is different (mid-rapidity vs forward rapidity) which mandates different particle rate and background calculations.

BTOF: The BTOF simulations show an average of 5 charged particles per ep collision at the highest center of mass energy. At the 500 kHz collision rate this amounts to a 2.5 MHz particle rate on the

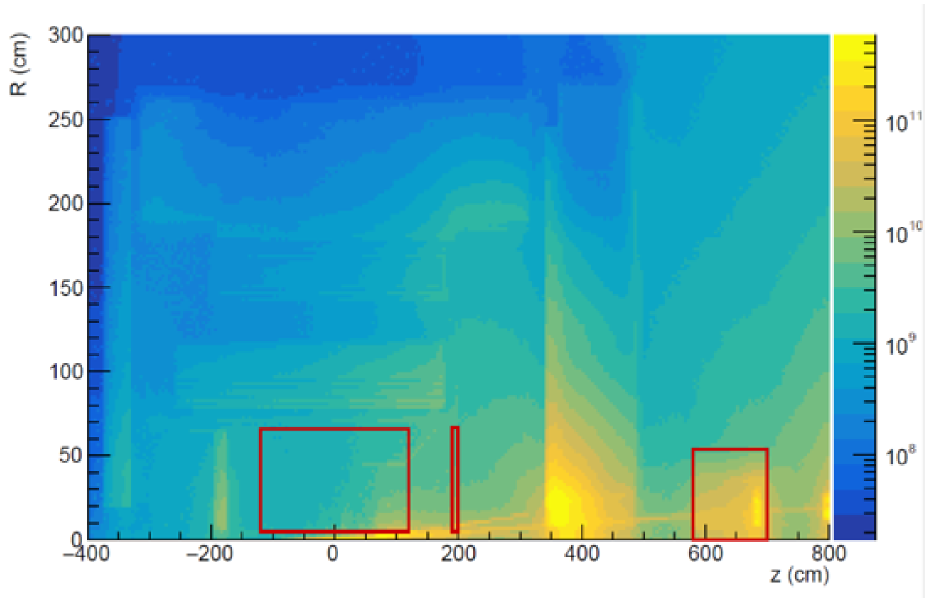

Figure 8.8: Fluence accumulated for 6 months at 100% time, corresponding to one year of data taking, the fluence has to be multiplied by the assumed 10 years of life time of the ePIC detector. Red squares highlight the barrel, end-cap, and B0 trackers detectors.

RAW fluence			
System	Average	Min	Max
Barrel	5.4×10^{10}	3.4×10^{10}	5.9×10^{11}
End-cap	1.3×10^{11}	5.1×10^{10}	1.6×10^{12}
B0 trackers	3.9×10^{11}	3.3×10^{10}	1.8×10^{12}
NEQ fluence			
System	Average	Min	Max
Barrel	3.6×10^{10}	1.1×10^{10}	1.3×10^{12}
End-cap	1.2×10^{11}	3.2×10^{10}	8.4×10^{11}
B0 trackers	4.5×10^{11}	2.7×10^{10}	4.2×10^{12}

Table 8.2: RAW and NEQ fluence per system for the lifetime of the ePIC experiment, assuming 10 years of data taking at 50% time.

surface of the BTOF barrel. BTOF contains 2.4 million channels which give an average hit frequency per channel of 1 Hz. Due to charge sharing of the AC-LGAD strips we expect a particle to generate signals on maximum 3 strips/channels of the readout ASIC.

FTOF: The FTOF simulation shows an average of 2 charged particles per *ep* collision at the highest center of mass energy. At the 500 kHz collision rate this amounts to a 1 MHz particle rate on the surface of FTOF disk. Since FTOF is expected to contain 5.8 million channels the average hit frequency per channel is 0.2 Hz. Due to charge sharing of the AC-LGAD pixels we expect a particle hit to generate signals on maximum 3x3 pixels/channels of the readout ASIC.

Electronics Noise: Noise measurements have consistently shown a rate of 30 Hz per channel. Such a noise rate is achieved with a 5-sigma cut and is deemed to be even somewhat pessimistic but this is the number we plan to use during these calculations.

Data Rates: We will assume a typical CERN-developed ASIC's zero-suppressed data format which is: 32 bits header, Nx32 bits of channel data (ADC, TDC, ch Id) and 32 bits trailer. Such data formats are used in e.g. HGCROC which is a precursor to our expected ASICs.

For BTOF the expected signal rate of bits per second per ASIC is 1 Hz (particle rate) x 5 x 32 (bits for 3 hits) X 64 (channels) = 10 kbps, while the noise rate is 30 Hz (noise) x 3 x 32 (bits for a single hit) X 64 (channels) = 185 kbps. Summing up these 2 contributions we reach the total data rate per-ASIC of 195 kbs. Since an RDO reads out 128 ASICs per half stave we expect a rate per RDO (or fiber) of 24 Mbps. For the entire BTOF which contains 288 half staves we reach a total rate requirement of 7 Gbps.

For FTOF the expected signal rate of bits per second per ASIC is 0.2 Hz (particle rate) X 11 x 32 (bits for 9 hits) X 1024 (channels) = 72 kbps, while the noise rate is 30 Hz (noise rate) X 3 x 32 (bits for a single hit) X 1024 (channels) = 3000 kbps. Summing up these 2 contributions we arrive at the per-ASIC data rate of 3.1 Mbps. For the worst case of 28 ASICs per RDO (or fiber) = 87 Mbs per fiber link to DAQ. For the total FTOF sub-detector of 212 RDOs we reach 18 Gbps.

We note that these rates are very small and well within the reach of ASICs, interconnects as well as fiber interfaces of our electronics and DAQ. We also note that the data rates are dominated by the electronics noise which we can control by raising or lowering the various ADC or TDC thresholds of the ASIC thus adjusting the system performance even ASIC-to-ASIC if required.

Device concept and technological choice: AC-coupled Low-Gain Avalanche Diode (AC-LGAD) is a new silicon sensor technology. Signals produced by charged particles in the sensor active volume are amplified via an internal p+ gain layer near the sensor surface. Signals induced on a continuous resistive n+ layer on top of the p+ gain layer, are AC coupled to patterned metal readout electrodes, which are on the sensor surface and separated by a dielectric layer from the n+ layer. The internal signal amplification and thin active volume enables precise timing measurement, while charge sharing among neighboring electrodes can provide precise position measurement. The AC-LGAD technology has been chosen to use for particle identification, tracking, and far-forward detectors at EIC where precision timing and spatial measurements are needed.

Subsystem description:

General device description: The BTOF consists of 144 tilted staves, each of which is made of two half staves with a total length of around 270 cm sitting at a radial position around 65 cm. AC-LGAD strip sensors are mounted on low mass Kapton flexible printed circuit boards (FPCs), and are wire-bonded with front-end ASICs. The FPCs are glued onto mechanical structures made from low density Carbon-Fiber (CF) materials, and bring power and input/output signals to the sensors and ASICs. The heat generated by the frontend ASICs are removed by an embedded Aluminium cooling tube in the CF structure. The FTOF consists of detector modules made from AC-LGAD pixel sensors bump-bonded with front-end ASICs. These detector modules are mounted from both sides onto a thermal-conductive supporting disk with embedded liquid cooling lines located around 190 cm away from the center of the experiment. Since the irradiation flux at the EIC is much smaller than that at the LHC, it is assumed that the radiation damage will not be a concern and the AC-LGAD sensors can be operated at room temperature.

Sensors: The sensors identified for the TOF timing layer are AC-LGADs that can provide both exceptional position resolution and timing resolution [1, 7–9] while maintaining low channel density. The BTOF will employ strip sensors 1 cm long with a pitch of 500 um and a metal electrode width of 50 um (large pitch up to 1000 um is also under investigation). The sensor thickness will likely be 50 um to reduce the input capacitance to the pre-amplifiers but 30 um thick strip sensors are also under investigation. The full sensor size will be 3.2x2 cm^2 with 1 cm segments. The FTOF will employ pixel AC-LGADs with a pitch of 500 um and metal electrode size of 50 um (large pitch up to 1000 um and electrode size of 150 um are also under investigation). The thickness of the pixel sensors will likely be 20 um to maximize the time resolution reach, as the input capacitance is not a concern for small pixels. Nevertheless, 30 um thick pixel sensors are also under investigation. The full-size sensor will be 1.6x1.6 cm^2 with 0.5x0.5 mm^2 pixels. Studies on smaller-scale devices are presented in [1,7] and in the following. The full-size strip sensor prototypes have been produced for the first time in the most recent HPK fabrication and received at the time of writing. Procurement of the full-size pixel sensor prototypes is still in progress. A complete evaluation of the full size prototype sensors is expected in the middle/end of 2025.

Front-End Electronics (FEE): The FEE for AC-LGAD based detectors is focused on the development of an ASIC and service hybrids. An ASIC featuring a Constant Fraction Discriminator (CFD) chip is being developed at Fermilab for the BTOF. The efforts have been focused on optimizing the analog frontend design to read out AC-LGAD strip sensors. Two versions of the ASICs, FCFDv0 and FCFDv1, featuring single- and multi-channel preamplifier and CFD, respectively, have been fabricated and tested. The new versions, FCFDv1.1 with further improvement to the frontend design tailored to 1 cm AC-LGAD strip sensors, FCFDv2 with digital readout, are under development with an expected deliver date in early 2025 and 2026, respectively. The EICROC project by the French group is focused on designing an ASIC for reading fine-pixelated AC-LGAD sensors, optimized pixel-based AC-LGADs detectors at ePIC such as B0, OMD, Roman Pots, and FTOF. The first version, EICROC0, is a 4x4 channel ASIC with 0.5x0.5 mm^2 pixel size, featuring components like a transimpedance pre-amplifier, 10-bit TDC for timing, 8-bit ADC for amplitude measurement, and an I2C slow control interface. It is designed for low capacitance and sensitivity to low charges (2 fC), operating with 1 mW per channel, and targeting 30 ps timing and 30 μ m spatial resolution. The prototype is currently under testing, with noise issues being addressed for future iterations. The next version, EICROC1 (expected in 2025), will feature a 16x8 channel configuration, followed by the final 32x32 channel version for full-scale implementation.

The service hybrids (SH) consists of a readout board (RB) and power board (PB). A schematic design of service hybrids, which serves 3 modules or 12 sensors/ASICs, for FTOF is shown in Fig. 8.9. The readout board will aggregate data from multiple ASICs to a lpGBT (from CERN) tranceiver chip via e-links, and then convert to optical signals via a VTRx+ chip (from CERN) to be transmitted to the backend data acquisition system. lpGBT and VTRx+ are designed for HL-LHC so have been proven to be sufficiently radiation hard for the EIC environment. The VTRx+ has one uplink up to 10 Gbs (for receiving clock and control signals), and four downlinks (for data transmission), each up to 2.56 Gbs, so it can transmit data up to four lpGBTs. The readout board also hosts interface connectors to the module board (as described later) and power board, as well as to input LV and BV cables. The power board provide low voltages for ASICs (1.2V), as well for lpGBT (1.2V) and VTRx+ (2.5V and 1.2V) on the readout board via DC-DC converters. The CERN bPOL48V module is chosen as the main converter, which takes an input of 15V and converts it into 1.2V and 2.5V. As illustrated in Fig. 8.9, the RB is situated on top of the PB and sensor module. The PB is directly contacting the cooling structure to facilitate efficient cooling of heat dissipation from DC-DC converters. The SH will have three different types with different lengths, serving 3 (12), 6 (24) and 7 (28) modules (sensor/ASICs). This will provide the most efficient coverage of a circular shaped disk while minimizing number of cables and fibers. The example shown in Fig. 8.9

is the shortest version (about 100mm long) which serves 3 modules. The latest layout design for FTOF disk is shown in Fig. 8.6 (right), where different colored boxes indicate different types of SHs. Prototyping of the SH is in an advanced stage. A pre-prototype readout board (ppRDO) has been developed and under testing, based on an Xilinx FPGA chip and a commercial SFP+ optical transceiver. The first prototype RB and PB based on CERN chips will be soon developed, especially based on similar existing design of the CMS endcap timing layer (ETL) detector.

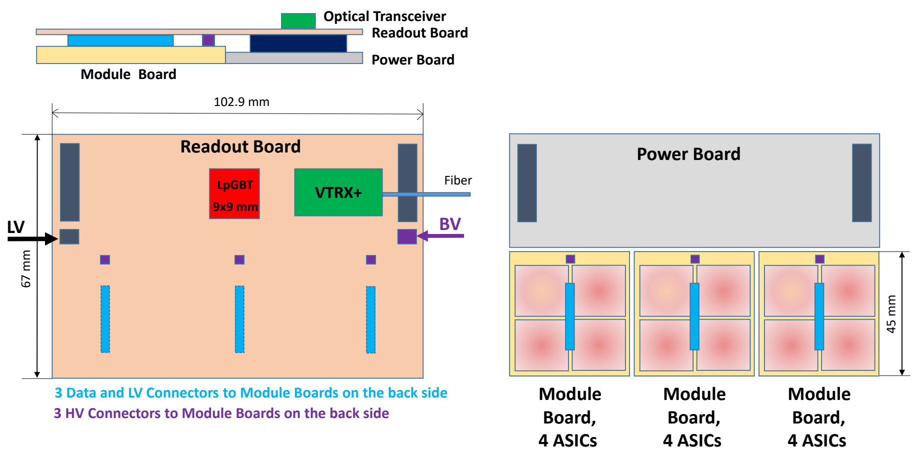

Figure 8.9: A schematic design of service hybrids for FTOF, which serves 3 modules or 12 sensors/ASICs.

Flexible Printed Circuit boards: The Flexible Printed Circuit (FPC) is used to read out data and distribute power to the sensors and ASICs. In the acceptance region, a material budget of 1% X/X_0 is required, meaning the FPC material should be as minimal as possible. Additionally, the FPC must be 135 cm in length. To meet these stringent requirements, careful consideration of the FPC material is necessary, as signal loss is expected with such a long FPC, especially if using polyimide, a standard material in FPCs. The sPHENIX experiment encountered a similar challenge with their Inner Tracker (INTT), a silicon sensor tracker, and successfully addressed it by using Liquid Crystal Polymer (LCP) instead of polyimide as the dielectric material. This technology will be adopted for our detector as well.

BTOF stave design: Barrel staves are divided into two half-staves, with services and connections coming from the outer side. The half-staves consist of a support structure with an integrated cooling pipe, flexible printed circuit (FPC), sensors, and ASICs. Sensors and ASICs are mounted on both the front and back sides of the half-stave, making it double-sided, with enough overlap to achieve 100% coverage in the stave direction. The lateral overlap and tilting ensure 100% coverage in the direction parallel to the staves. In total, there are 64 sensors and 128 ASICs on each side of the half-staves.

FTOF module design: A schematic design of the module for FTOF is shown in Fig. 8.10. Each module consists of 2×2 LGADs sensors and ASICs. It is covered by a module PCB board (MB), which will provide LV power (1.2V) and transmit the data of ASICs via a board-to-board connector to the RB. In addition, the MB also has a BV connector to the RB for providing the BV to LGADs sensors. ASIC readout will be wire-bonded to a metal pad near the edge of the module on the side facing the baseplate and cooling structure, as illustrated in

Fig. 8.10 (right). LGADs sensor and ASIC will be connected via bump bonding. Dimensions shown are preliminary and will be adjusted as the prototyping progress. In the current design, the LGADs sensor is placed underneath the ASIC. The motivation is to have the sensor as close as possible to the cooling structure to ensure lower and stable temperature, which has been proven to be essential for achieving optimal time resolution. An alternative option would be to swap the ASIC and sensor layer, which has the advantage of more efficiently dissipating heat primarily generated by the ASIC. A final choice will be made as the prototype progress, especially after realistic thermal performance studies have been carried out.

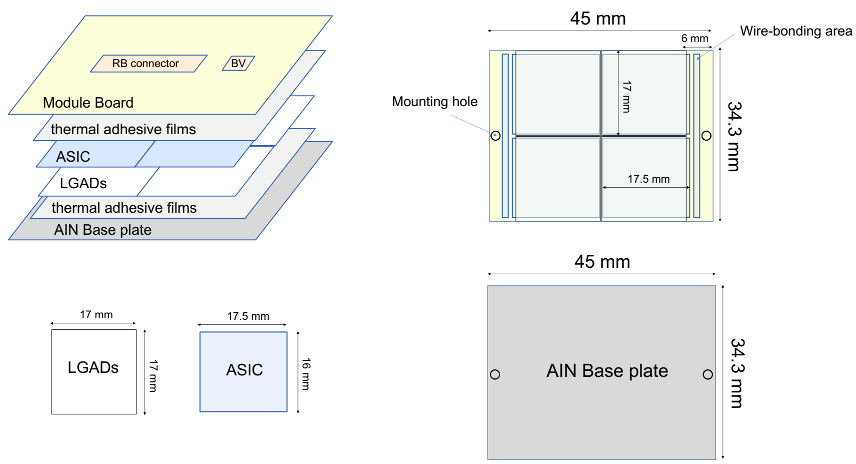

Figure 8.10: A schematic design of the module for FTOF, which consists of 2×2 LGADs sensors and ASICs.

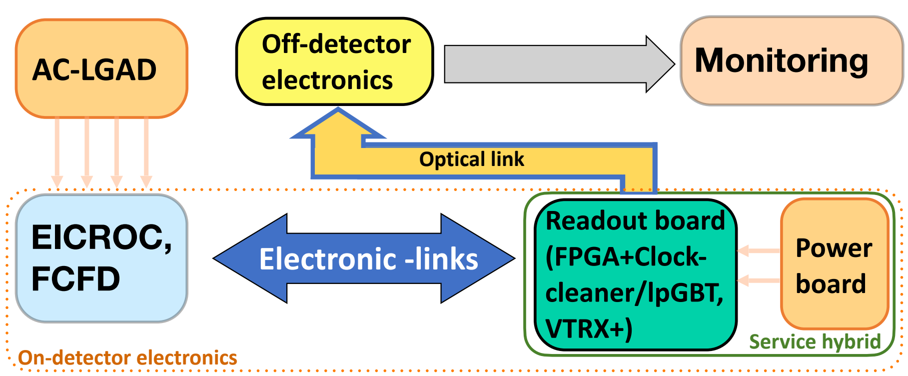

Figure 8.11: Schematic of the AC-LGAD sub-system readout chain. Each component is undergoing design, (pre-)prototyping, testing under various environments, and customization to meet the specific requirements of individual subsystems.

Performance The AC-LGAD systems, including the BTOF, FTOF, and far-forward systems (Roman Pots, OMD, and B0 tracker), share a common readout chain currently under development. Performance evaluations are being conducted in various laboratory environments as part of the ongoing R&D efforts. A schematic of the full readout chain is shown in Fig. 8.11. The effort can be divided into to parts: 1) integrating the sensors with ASIC, 2) development of the readout-board and power board.

The Fermilab team has been developing an ASIC targeting the AC-LGAD strip sensors for BTOF. Studies showed that Constant Fraction Discriminator (CFD) could provide a better timing resolution with small signal amplitude from LGAD than leading edge descriminator [10]. The first single-channel CFD-based ASIC (FCFDv0) wire-bonded to a DC-LGAD sensor achieved 35 ps timing precision with beam, where the dominant contribution is expected from the intrinsic resolution of the LGAD sensor. A 6-channel prototype (FCFDv1) was developed for AC-LGAD sensors, demonstrating 11 ps jitter in charge injection and 50 ps time resolution with 0.5 cm AC-LGAD strip sensor in test beam. Ongoing efforts are focused on optimizing the frontend design for 1 cm AC-LGAD strip sensors for the BTOF.

Assemblies of 4x4 AC-LGAD pixel sensors with 500×500 μm^2 pixelation and 30 μm thickness, and 4x4 EICROC0 ASICs, were completed by the BNL, IJCLab, OMEGA, and Hiroshima groups on test-boards developed by IJCLab/OMEGA. Testing included scans of the analog and digital components using charge injection and beta particles from a Sr-90 source, resulting in a measured jitter of 8-9 ps for charges above 20 fC. Both wire-bonded and flip-chip assemblies were developed for various characterizations. Additional tests using Transient Current Technique (TCT) laser scans were conducted to map out charge distribution, and various tests are still ongoing.

ORNL is developing flexible Kapton PCBs for TOF applications, where sensors and mockup ASICs will be glued, wire-bonded, and co-cured onto a composite structure at Purdue for evaluation. Flip-chip options will be available soon, aiming to support low-cost sensor-ASIC hybridization techniques.

In FY24, BNL, LBNL, and Rice developed a prototype board (ppRDO) for precise clock distribution and ASIC integration for AC-LGAD systems. Key milestones, including schematic designs, part orders, PCB layout, and initial testing, were completed ahead of schedule. Firmware development and performance tests on clock-cleaning, jitter, and power distribution are ongoing. The collaboration aims to continue in FY25, focusing on the development of a readout board (RBv1) and power board (PBv0) for AC-LGAD systems, supporting TOF applications and ensuring DAQ compatibility. The ppRDO includes three components: 1) FPGA, 2) clock cleaner, and 3) SFP+ module. Future versions will adopt lpGBT to replace the FPGA and clock cleaner, and VTRx+ to replace the SFP+ module, improving performance, radiation hardness, and integration.

Implementation

Services: Electric power is distributed to the detector components via the Power Board (PB), which is part of the Service Hybrid (SH). The SH also includes the functionality of the Readout Board (RDO). In the case of BTOF, one SH supports 64 sensors and 128 ASICs, with SHs placed on both sides of the stave. For FTOF, several types of SHs are used, covering 12, 24, or 28 sets of sensors and ASICs. The SH is distributed on the mechanical and support disk, together with sensor modules.

Low Voltage (LV) and High Voltage (HV) cables are connected to the PB, where multiple DC-DC converters step down or adjust the voltages as needed. HV is applied to groups of multiple sensors, rather than distributed individually to each sensor. The size of each sensor group is determined by the design of the sensors and the electronics. Table 8.3 summarizes the service (cables and tubes) necessary for TOF detectors.

subsystem	item	quantity	diameter (mm)	lengths (m)	description
BTOF	FEE LV	24	20	15–25	Rack to Panel, 8AWG (24 AWG sense pairs)
BTOF	FEE LV	72	6.3	8	panel to detector, Alpha PN: 2424C SL005
BTOF	FEE HV	18	14	15–25	Rack to Dist. Panel
BTOF	FEE HV	144x2	1.5	8	panel to sensor
BTOF	cooling tubes	144x2	5	> 2.6	supply/return from panel to stave (Aluminum)
BTOF	cooling tubes	4x2			supply/return to panel
FTOF	FEE LV	212	9.04	25	supply/return LV from FEE to Rack
FTOF	FEE HV	14	14	25	rack to dist. panel
FTOF	FEE HV	212	2.42	10	panel to sensor
FTOF	cooling tubes	2x2	5		supply/return from panel to detector (Aluminum)
FTOF	cooling tubes	2			supply/return to panel

Table 8.3: Summary of BTOF and FTOF low voltage and high voltage powersupply cables to distribution panels and then to the detector FEE (the exact numbers are being checked at the time of writing).

A liquid cooling system is employed to control the temperature of the detector. For the BTOF stave, one or two cooling pipes are integrated into the stave sandwich structure, with liquid flowing in one direction along the length of the stave. In FTOF, a winding liquid pipe is integrated into the support sandwich structure. The flow rate and pipe diameter are determined by the amount of heat generated and the detector's performance requirements, thermal finite element analysis determines the design. The pressure must remain below the surrounding air pressure to ensure safe operation. Fig. 8.12 shows a single BTOF stave with cooling pipe (left) and half of the FTOF structure with cooling pipes (right).

Subsystem mechanics and integration: Both the BTOF and FTOF detector systems are supported by their own support structure, which is integrated and supported by the global support tube (GST). The BTOF is a barrel geometry time-of-flight detector system located at a radius of

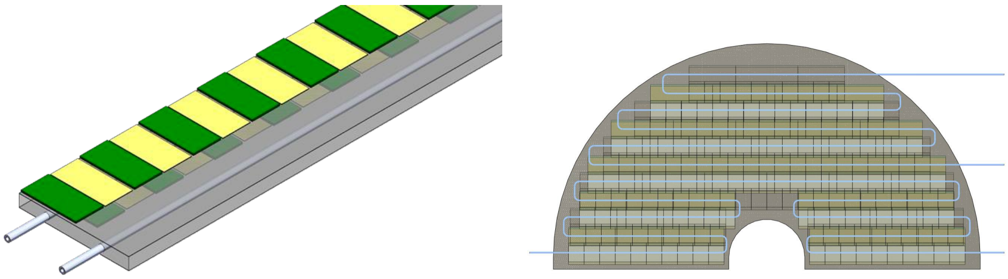

Figure 8.12: schematic drawings of one BTOF stave (left) and half of the whole FTOF (right) cooling pipes.

63cm from $z = -117.5$cm to $z = +171.5$cm along the beam direction as shown in Fig. 8.13. Both detector subsystems have 7.5cm space in radial direction for BTOF and in the beam direction for FTOF. The three engagement rings (each of 5mm width) are made from composite materials as a sandwich and support the BTOF detector - they are itself supported by the GST. A first concept was developed for a BTOF stave mounting mechanism employing the engagement rings by clips with staves at an 18 degree angle. Staves are removable individually to ease maintenance. The FTOF detector is designed in two half disc structures, or dee's, that are kinematically mounted to the GST. Services (readout, power, cooling) of the BTOF and FTOF are routed either way and supported itself by the GST. Table 8.4 lists the positions of BTOF and FTOF relative to the global ePIC geometry.

subsystem	z_{min} (cm)	z_{max} (cm)	inner radius (cm)	outer radius (cm)	stave angle
Barrel TOF	-117.5	171.5	62	69.5	18^o
Forward TOF	185	192.5	10.5	60	0

Table 8.4: BTOF is designed with a barrel geometry surrounding the beam pipe and interaction point, while FTOF is a disk geometry perpendicular to the beam direction on the hadron side (positive z).

Calibration, alignment and monitoring: **Calibration and alignment:** For spacial calibration and alignment, the TOF layer is essentially treated as a layer of the overall tracking system. Therefore, spacial alignment will be carried out as part of the entire tracker. This is typically based on the match between tracks reconstructed in other layers of the tracking, then extrapolated to the TOF and the hits in the TOF. By combining the information from many tracks, high precision can be achieved.

To exploit timing in the reconstruction of the charged tracks, the different TOF channels will have to be synchronised to a precision of a few picoseconds. The absolute time calibration (or phase shifts relative to the beam clock) is not a particular concern, as all the event reconstruction relies on the relative time between tracks within the same collision event. The time offsets of the TOF channels can be inter-calibrated using all the tracks collected online through a fast reconstruction stream. The distribution of the reconstructed time at the vertex of these tracks – assuming they are pions – should an rms spread of approximately 50 ps, including the time spread of the luminous region and detector resolution. The mean time of this distribution over many tracks provides the reference calibration points. Non-pion particles will contribute to the tail of the distribution, which

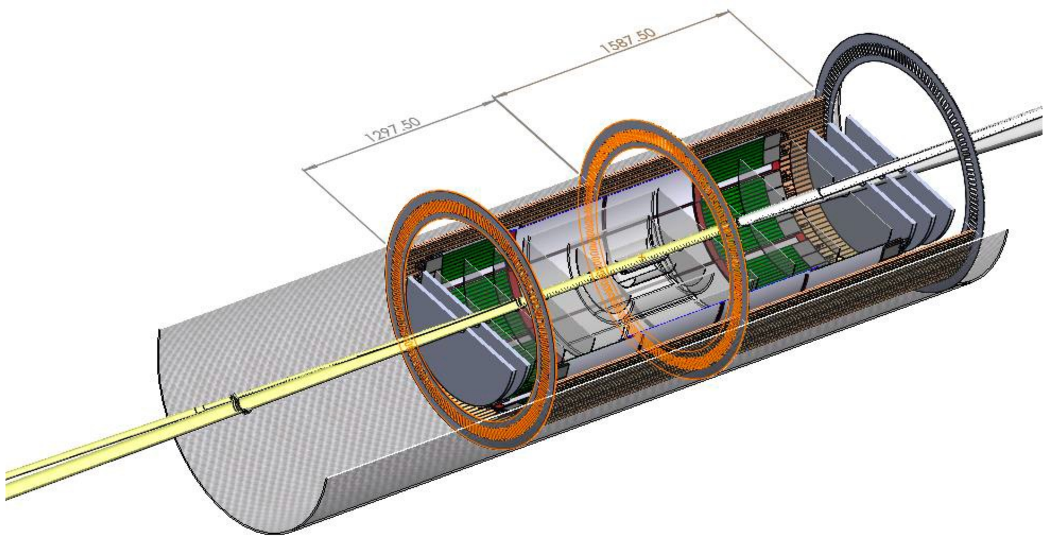

Figure 8.13: Barrel TOF supporting mechanic structure with engagement rings situatued and supported by the EPIC global support tube structure (GST). The width of each of the three engagement rings is 5mm.

can be cleaned up using an iterative procedure but not necessary. These calibrations can be made available for the prompt reconstruction of the events and updated frequently.

Monitoring: In the readout scheme of the TOF, a common clock is distributed to the individual channels belonging to the same service hybrid. The time stability of the clock distribution can be monitored with a precision of a few ps every second.

Status and remaining design effort: eRD112 and eRD109

eRD112: Sensor R&D effort A brief summary of eRD112 activities is reported in this section, for a more detailed review of the sensor development effort consult the 2024 erd112 report document. HPK sensors from the latest production have been tested at the Fermilab test beam facility; the results are summarized in Ref. [1]. The summary best results are reported in Fig. 8.14. The same HPK production was tested in laboratory with focused laser TCT and showed similar results as reported in Ref. [8]. The presented strip sensors (Fig. 8.14, Left) show a constant time resolution of around 35 ps, which is within the requirements for the ePIC TOF. The strip reconstructed position resolution is between 10-20 μm, which is also within the ePIC TOF requirement of 30 μm. The best result for pixel sensors (Fig. 8.14, Right) shows an homogeneous time resolution of 20-25 ps, well within ePIC TOF requirements. The position resolution instead is 20-70 μm across the device; the charge-sharing mechanism allows for precision reconstruction in between metal electrodes, but the resolution is significantly worse for hits directly on the metal electrodes.

The position resolution requirement for the FTOF is 30 μm. Therefore, pixel technology needs to be refined to meet the requirements. The new HPK production (expected by the end of the year) includes smaller electrode sizes and larger gaps between electrodes that could provide good reconstruction across the sensor. However, it was observed that a larger gap decreases the total S/N

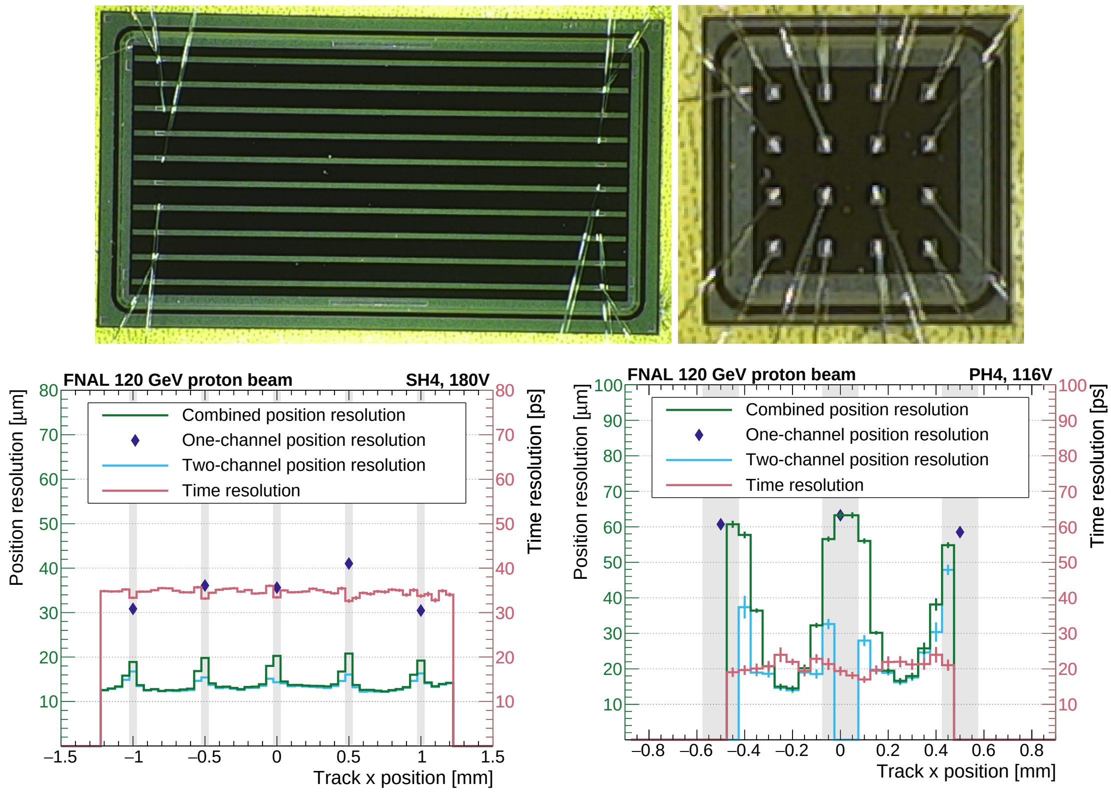

Figure 8.14: Left: Picture and beam test results for HPK strip sensor, 1 cm long, 500 μm pitch, and 50 μm metal electrode width. Right: Picture and beam test results for HPK pixel sensor, 4x4, 500 μm pitch, and 150 μm metal electrode width. Plots from Ref. [1].

between electrodes, which might degrade the overall performance of the sensors. Results from a BNL production provide a promising alternative to square metal pixels. The S/N is better across the sensor for a cross-shape electrode given the same central metal shape, allowing for better reconstruction using charge sharing. HPK did not include cross-shape geometry in the latest production, but it might be included in the next one. Another producer of cross-shaped AC-LGADs is Fondazione Bruno Kessler (FBK). The FBK prototypes were investigated with a laser TCT, and a similar behavior was observed for cross-shaped devices [9].

The sensors irradiated at the Triga Reactor with 1 MeV neutrons were received in Spring 2024 and characterized both for electrical proprieties (capacitance and current over voltage) and with the laser TCT station. Gain degradation can be probed with measurements of capacitance over voltage by identifying the gain layer depletion point (V_{GL}). Fig. 8.15, Left, shows the change in the gain layer for the irradiated HPK AC-LGADs from several wafers, with different N+, oxide and active thickness, up to 1×10^{15} Neq; in the region of interest for ePIC $< 10^{13}$ Neq the gain layer is unchanged. The charge-sharing proprieties after irradiation were tested using a focused IR laser in the laboratory. As seen in Fig. 8.15, Right, the spatial response of the sensor is unchanged after irradiation up to 5×10^{14} Neq. The current increase in the irradiated HPK sensors is also negligible until $< 10^{13}$ Neq, as shown in Fig. 8.15, Bottom. The measurements were done at room temperature; therefore, no cooling will be necessary to reduce the dark current, which would increase the sensor power dissipation in ePIC. In conclusion, no change in the behavior of the sensors is expected during the lifetime of the ePIC detector due to radiation damage.

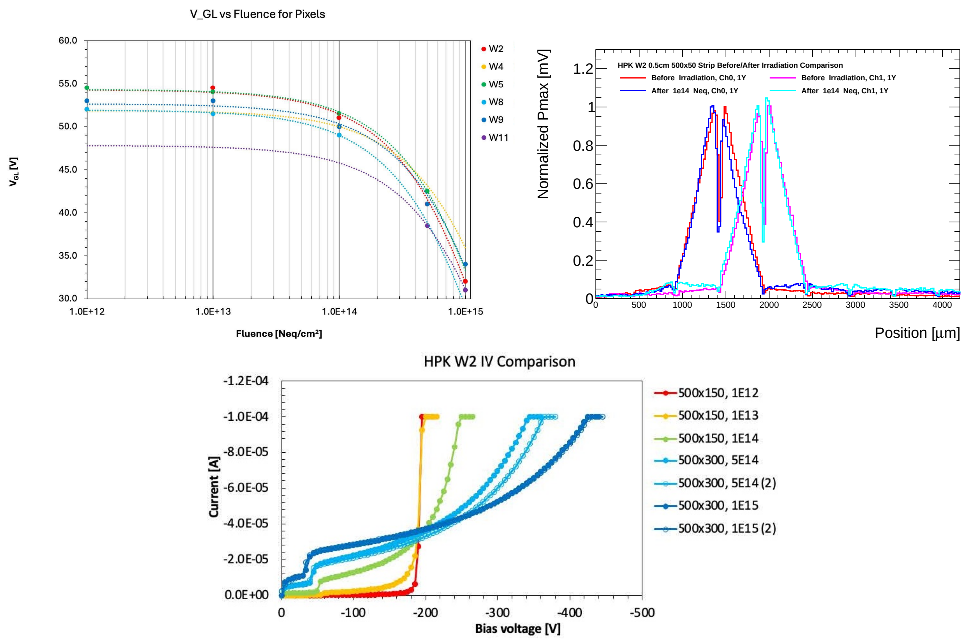

Figure 8.15: Left: Degradation of the gain layer for AC-LGADs of several wafer (with different N+, oxide and active thickness) from HPK latest sensor production, showing no change in gain layer doping up to 10^{13} Neq, which is an order of magnitude over the ePIC TOF radiation requirement. Sensors were irradiated at the TRIGA reactor (Lubjiana) with 1 MeV neutrons. Right: Normalized comparison of response profile of two nearby strips for two HPK 0.5 cm length, 500 μm pitch, 50 μm strip width: one before irradiation and one after 1×10^{14} Neq, even if the total signal is degraded the charge sharing profile is unchanged. Bottom: Current over voltage measurement for irradiated HPK sensors.

eRD109: readout R&D effort A more detailed review of the electronics development effort can be found in the 2024 eRD109 report document. In the following section, a brief summary will be provided.

The Fermilab team has continued the development of the FCFD ASIC prototype and, in FY23, has designed the first multi-channel prototype with this approach, labeled as FCFDv1. Numerous technical improvements were implemented based on the experience with FCFDv0, aimed at addressing the stability and performance of the system. The FCFDv1 ASIC was submitted for production in September 2023, and received in January 2024. A specialized readout board was designed to accommodate the FCFDv1 connected to a 0.5 cm HPK AC-LGAD strip sensor. Initial measurements of the performance were done using internal charge injections performed with an LGAD-like signal. With input capacitance ∼3.5 pF a jitter of around 11 ps was achieved, as shown in Fig. 8.16, left. Test beam campaigns have been performed to study the performance of the FCFDv1 in June 2024. The newly introduced amplitude readout was found to function well, and results show 100% efficiency when combining neighboring strips. The time resolution measured from the beam test was around 50 ps. A further design improvement is foreseen in FCFDv1.1 to accommodate 1 cm AC-LGAD strip sensor and improve the timing resolution.

The development of the EICROC0 chip is proceeding as planned. In 2024, an updated PCB ("2024" PCB), has been designed by OMEGA. This updated PCB features improved testability and grounding, as well as the removal of supplementary PLLs. The chip shows good homogeneity between channels and Jitter <35 ps for an injected charge of >4 fC, both for the pre-amplifier and for the discriminator output, as seen in Fig. 8.16, Left. A large correlated noise still remains with the updated "2024" PCBs (already observed in the "2023" PCB), which leads to large TDC jitters, over 50 ps, when by design, the TDC jitter is expected to be of the order of 10 ps. Nevertheless, the intrinsic performance of the preamplifier, the TDC, and the ADC, taken individually, is confirmed to be in agreement with the design and within the ePIC detector specifications.

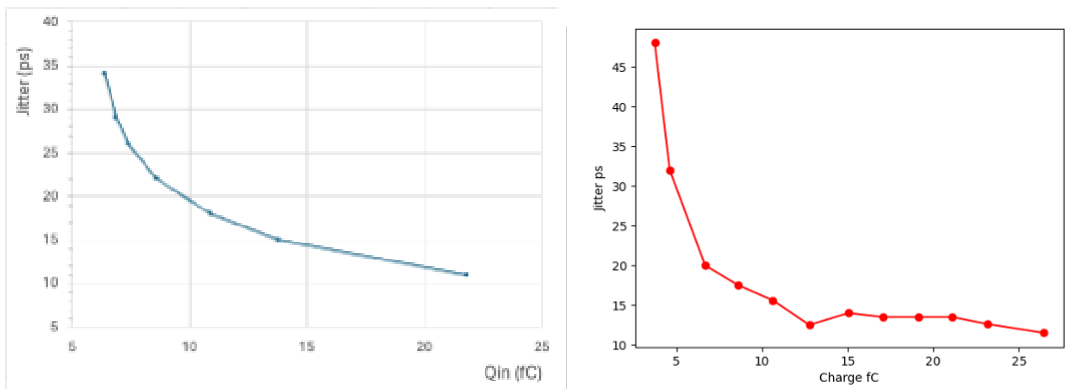

Figure 8.16: Left: FCFD Jitter measurements with 3.5 pf input capacitance and charge injection. Right: EICROC Discriminator jitter versus the injected charge, determined from data on an oscilloscope. Left: FCFD Jitter measurements with 3.5 pf input capacitance and charge injection. Plots from the erd112 and erd109 2024 reports.

The development of pre-prototype readout board (RDO) with high precision clock distribution has been completed. Figure 8.17 shows a picture of the ppRDO. It is connected with the CMS ETL module board v0, which consists of the full-sized ETROC2 chip for testing purpose. The ppRDO will be evolved into the prototype RB for FTOF next that consists of lpGBT and VTRx+ chips, instead of FPGA and SFP+. Those efforts will be carried out under engineer designs as described later.

E&D status and outlook: E&D activities

Thermo-Mechanical demonstrator: The fabrication of a demonstrator stave following the double-sided design, as seen in Fig. 8.19, is ongoing. The demonstrator will be a thermal/mechanical demonstrator of the assembly procedure and chip/sensor power dissipation. A mock-up stave, example in Fig. 8.18, will be co-cured with a readout flex with a cooling pipe in the center, and a series of Si heaters and full-size HPK sensors from the latest production will glued to the stave, then wire-bonded together and to the readout flex. The demonstrator will be used to probe the power dissipation, the temperature gradient across the stave, and the mechanical assembly procedure. Demonstrator results are expected by Q1 2025.

Environmental, Safety and Health (ES&H) aspects and Quality Assessment (QA planning: We also carried out QA long-term and stress-test reliability studies of LGADs as a stepping-stone towards studies on AC-LGADs. The tests were conducted in an ambient chamber at various environmental conditions. We kept the sensors under bias voltage over periods of weeks, at different temperatures, ranging from -60 to +80 degrees Celsius and under different humidity conditions.

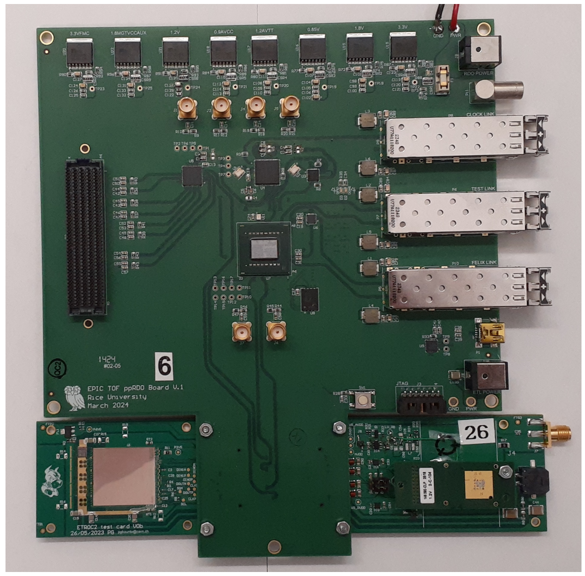

Figure 8.17: Picture of ppRDO connected with CMS ETL module board v0 for testing.

Figure 8.18: Assembled stave prototype at Purdue.

Under these extreme conditions we carried out I-V scans. At intervals of time between temperature cycles, we also collected signals from beta particles from a Sr-90 source at room temperatures to study any deterioration in noise or charge collection. The results were presented at IEEE conference: While we saw an impact of humidity and temperature on current and breakdown voltage, the sensors recovered their original performance in subsequent cycles. In addition, we also studied the impact of passivation on sensors to minimize charge build-up and early mortality. We confirmed that passivation is critical to minimise the impact of humidity on sensors and prevent early mortality. Such tests were critical after issues have been observed in silicon sensors used for tracking detectors in other experiments, such as those at the HL-LHC. As part of our QA strategy, we also sent to colleagues of UNM BNL-made AC-LGADs to have them irradiated at various fluences in a proton beam at ITA, in a gamma beam at SANDIA and with neutrons at the TRIGA reactor. The first results are shown in the previous sections.

For both sensors and readout chips, it is imperative to evaluate the yield of the test productions to adjust the final production orders. The QA plans to evaluate the yield of the sensor productions are as follows: each produced sensor will be tested in the laboratory in a probe station with simple current over voltage (IV) and capacitance over voltage (CV) tests. AC-LGADs have a single point of DC connection on the N+, so only 1 or 2 needles are necessary for the test; a probe card is not necessary for QA. The IV test will allow us to check the current level and the breakdown voltage for each produced device; the current level has to be $<< 1\mu A$ to not introduce power dissipation issues. The breakdown voltage of all devices has to be within **10%?** to avoid issues in the HV distribution. The CV test will allow to probe the gain layer depletion voltage and demonstrate that all devices have homogeneous gain; for LHC prototypes [6], the gain homogeneity was within 1%. A selection of devices from the full production will be characterized by mounting them on analog front-end boards with laser TCT and at test beam facilities to ensure the homogeneity of the charge-sharing response.

To evaluate the yield of the chip (EICROC, FCFD) productions, a sample of chips from each batch will be tested and probed for homogeneity in all the channels using a calibration input. All channels have to be within **10%?** of homogeneity. A selection of chips will be coupled (wire bonded or bump bonded) with a matching working sensor and mounted on a prototype PCB to probe correct and homogeneous operation in a realistic configuration. Then the boards will be tested with a laser TCT or at test beam facilities.

Once the state of sensors, readout chips, and flex is advanced, a fully loaded demonstrator stave is envisioned. The mounting procedure will already be tested during the assembly of the thermo-mechanical demonstrator. The full demonstrator will then be tested with radioactive sources in laboratory or at test beams.

Construction and assembly planning: The BTOF detector has a cylindrical shape, consisting of 144 tilted staves. These staves are assembled at designated sites within class-7 or higher clean rooms before being transported to BNL for final construction. Each stave is approximately 270 cm long and is divided into two half-staves of 135 cm. A half-stave includes a support structure with an integrated cooling pipe, a flexible printed circuit (FPC), sensors, and ASICs. The sensors and ASICs are mounted on both sides of the half-stave, with 64 sensors and 128 ASICs on each side. Wire-bonding is used to connect the ASICs to the sensors and electronics. Only components that pass various quality inspections—such as visual checks, metrology, and electrical tests—proceed to the assembly stage. During the half-stave assembly, one FPC is glued onto the support structure (Fig.8.19 (a)). To ensure precise alignment, a specialized tool is used, featuring pins and holes that guide the placement of the FPC and the correct application of glue. After assembly, the staves undergo both electrical and mechanical tests. Subsequently, sensors and ASICs are installed on the FPC surface using alignment tools similar to those used during the FPC mounting process (Fig.8.19 (b)). These tools help position the components and apply adhesive. Electrical connections are verified, and the ASICs are bonded to the sensors using wire-bonding, followed by wire encapsulation (Fig.8.19 (c)). 2 support structure with wire-bonded sensor, ASIC, FPC which is corresponding to front and back side, are attached to each other (Fig.8.19 (d)). Upon completing the installation on both sides (Fig.8.19 (e)), the final round of testing is conducted. Fully tested staves are then shipped to BNL for integration into the global support structure of the ePIC detector, which contains 144 slots for precise alignment of the staves within the global coordinate system.

The FTOF is constructed in a double-sided disk shape by populating modules with dimensions indicated in Fig. 8.10. Each module includes 4 sensors, 4 ASICs, a module board, and an Aluminum Nitride (AlN) base plate, which acts as a thermal conduit to the cooling system. The modules are connected to a service hybrid (SH) that consists of a power board (PB) and a readout board (RB). As mentioned earlier, three different configurations of SH are used, depending on the number of modules being supported: 3 modules (RB3), 6 modules (RB6), and 7 modules (RB7). There are about 780 modules in total to patch the disk shape. Sensor and ASIC are connected by bump-bonding. The module board is connected to the ASICs through wire bonding and has a connector to interface with the RDO. Assembly of the modules occurs in class-7 (or higher) clean rooms, while the PB and RB can be assembled under standard conditions. The assembly of each module begins with the connection of one sensor to one ASIC using bump-bonding technology (Fig.8.20 (a)). Automated machines are used for sensor and ASIC placement, alignment, and bonding. After bonding, the electrical performance of the sensor-ASIC hybrids is tested. Following this, 4 sensor-

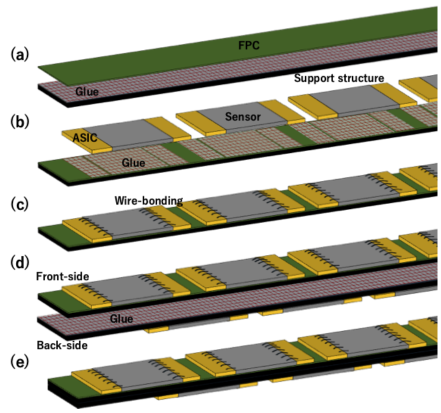

Figure 8.19: Assembly process of BTOF stave. Note, the scale is not real.

ASIC hybrids are mounted on the module board, using a dedicated tool to ensure precise alignment (Fig.8.20 (b)). Thermal adhesive films are placed between the hybrids and the module board to ensure efficient heat dissipation. Once mounted, the ASICs are wire-bonded to the module board, and the wires are encapsulated for protection. After the bonding process, the AlN base plate is attached to the opposite side of the hybrid (Fig.8.20 (b)), with thermal adhesive films again used between them to aid heat transfer. The thermal adhesive films are also put between them. The modules undergo thorough quality checks before moving on to SH assembly. The RBs and PBs are manufactured using standard circuit board techniques and come with dedicated connectors for integration. SHs are available in configurations supporting 3, 6, or 7 modules, with the RB and PB connected via dedicated interfaces (Fig.8.20 (c)). Once assembled (Fig.8.20 (d)), the modules and SHs are tested for connectivity and performance. After passing all tests, the modules and SHs are shipped to BNL, where they are attached to the disk-shaped support structure. Specialized tools ensure the accurate placement of the components. Modules and SHs are mounted on both sides of the support structure to eliminate acceptance gaps between sensors. When installing the modules and SHs on the opposite side, a fixture is used to maintain the required clearance between components. Finally, the fully assembled disk is installed into the ePIC detector.

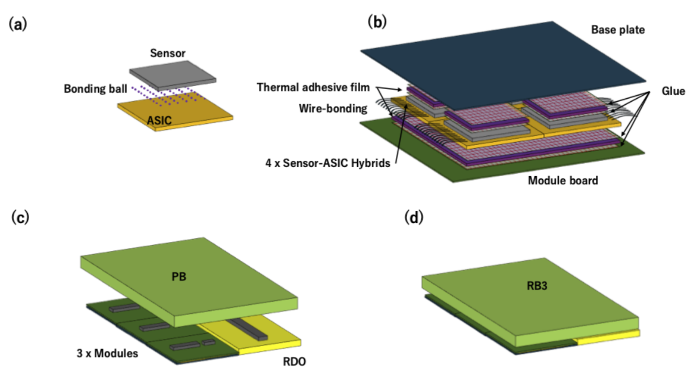

Figure 8.20: Assembly process of FTOF modules. RB3 type is shown as an example. Note, the scale is not real.

Institute	Contact Person	NOW (TDR->Project)
Brookhaven National Laboratory	Prithwish Tribedy tribady@bnl.gov	DAQ readout chain readout, sensor-ASIC integration, sensor with FF AC-LGAD; EICROC testing
Fermi National Accelerator		FCFD ASIC (no ePIC)
Los Alamos National Laboratory	Xuan Li xuanli@lanl.gov	
Rice University	Wei Li wl33@rice.edu	B/FTOF FEE?, Backend electronics (postdoc) , simulation and reconstruction
Oak Ridge National Laboratory	Oskar Hartbrich hartbricho@ornl.gov	sensor-ASIC integration, frontend electronics (waffle probing), module assembly
Ohio State University	Daniel Brandenburg Brandenburg.89@osu.edu	BTOF/FTOF: module assembly; backend electronics
Purdue University	Andreas Jung anjung@purdue.edu	Module assembly
Univ. of California, Santa Cruz	Simone Mazza simazza@ucsc.edu	Sensor, sensor-ASIC integration, module assembly (no in-kind)
University of Illinois at Chicago	Olga Evdokimov mailto:evdolga@uic.edu	
Hiroshima University	Kenta Shigaki shigaki@hiroshima-u.ac.jp	FTOF EICROC testing, sensor testing (30%), simulation
RIKEN	Yuji Goto. goto@bnl.gov	BTOF: module assembly
Shinshu University	Kentaro Kawaide kawade@shinshu-u.ac.jp	Sensor testing, simulations
University of Tokyo	Taku Gunji gunji@cns.s.u-tokyo.ac.jp	DAQ streaming readout
South China Normal University	Shuai Yang syang@scnu.edu.cn	
Univ of Sci. and Tech. of China	Yanwen Liu	
Indian Institute of Tech., Mandi	Prabhakar Palni prabhakar.palni@unigoa.ac.in	FTOF Module Assembly/QA, sensor testing
National Inst. of Sci. Edu. Res.	Ganesh Tambave ganesh.tambave@niser.ac.in	Module Assembly
National Central University		FF AC-LGAD (sensor QA)
National Cheng-Kung University	Yi Yang yiyang@ncku.edu.tw	Mechanics and cooling systems
National Taiwan University	Rong-Shyan Lu rslu@phys.ntu.edu.tw	FF AC-LGAD; module assembly
Univ. Técnica Federico Santa María		Simulations
LBNL	Zhenyu Ye yezhenyu2003@gmail.com	BTOF ASIC testing; SH
Kent State University	Zhangbu Xu zxu22@kent.edu	Simulation, readout test, machine shop (in-kind)
Nara	Takashi Hachiya hachiya@cc.nara-wu.ac.jp	BTOF module assembly/validation/FPCB

Figure 8.21: Collaboration institutions and their responsibilities.

Collaborators and their role, resources and workforce: Table 8.21 shows the participating institutes with their role, the contact person and potential commitments. This shows substantial participation by the international collaborators outside of the U.S.. We also anticipate substantial funding support from the international collaborators for the BTOF detector as well.

Risks and mitigation strategy: Our R&D results (eRD112) show that the performance of the sensors would meet physics requirements for TOF subsystems. Those studies were done with smaller chip dimension. The production for R&D study with full-size sensor chip is underway. There is a potential risk that the performance of sensors with larger size would be worse. The mitigation is to reduce the sensor size.

The HPK sensors for R&D (eRD112) is of small quantity. A mass production would be a risk in terms of chip yield and schedule delay. The mitigation is to explore other possible production sites (Taiwan/FBK).

FCFD ASIC design (eRD109) currently only has analog signal readout. The design and test of the digitization component is underway and expected to have first pass early next year. Additional resource may be need to mitigate potential schedule delay and cost increase. In addition to the baseline chips EICROC and FCFD, third-party ASICs are also taken into consideration: FAST

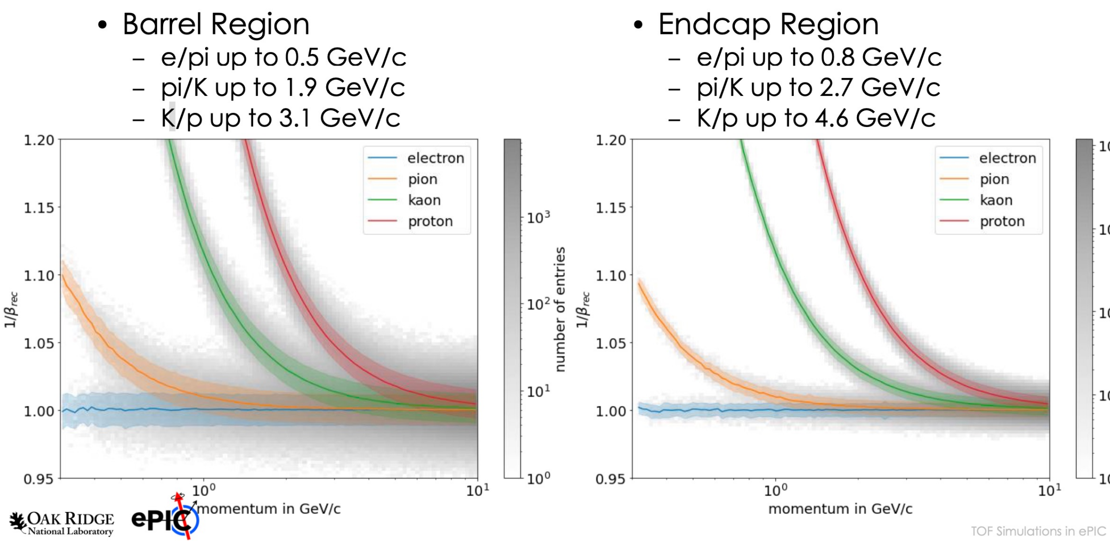

Figure 8.22: simulation of $1/\beta$ as a function of particle momentum for BTOF and FTOF performance.

(INFN Torino), AS-ROC (Anadyne Inc. + UCSC), and HPSoC (Nalu + UCSC). The most advanced one is the High-Performance System-on-Chip (HPSoC) ASIC, designed by Nalu Scientific [11], in close collaboration with SCIPP, and fabricated in 65 nm CMOS by TSMC. HPSoC comprehends a fast analog front end and, unique to all other current LGAD readout ASICs, will capture the full signal waveform at a sampling rate of 10-20 GS/s. Together, these are expected to address the EIC goal of 25 ps timing resolution or better per measured space point. V2b of the chip has a working digital back-end and is currently under review.

We have performed heat conductivity and cooling simulations, and R&D test on cooling capacity (currently with PED funding). Those show promising outcome for meeting the cooling needs. The potential risk is that the cooling capacity is not sufficient to maintain a stable and relatively uniform temperature. A possible mitigation strategy is to use different material for cooling pipe with better heat conductivity and higher flow rate.

Additional Material

8.3.4.2 The proximity focusing RICH

Requirements

Requirements from physics: The ability to identify different species of hadronic particles (pions, kaons, and protons) and to separate these from electrons will be essential for realizing much of the EIC physics program. Particle identification capabilities in the electron going endcap region of the ePIC detector ($-3.5 \leq \eta \leq -1.5$) will be provided by a proximity focusing ring imaging Cherenkov detector (pfRICH). Hadrons in this region generally originate from collisions probing low x at a given Q^2, which is a phase space of great interest for studies in both e+p and e+A configurations. In e+A collisions this is the kinematic region where the onset of gluon saturation is expected. Saturation generally describes novel QCD phenomena originating from the overlap of the gluon wavefunctions, which is thought to happen at low x where gluon densities are high. This is also a region that has never been explored by polarized e+p experiments before and measurements of identified kaons in the backward region, for example, will provide information on the polarized strange quark distributions.

Studies of physics requirements in the EIC Yellow Report define the particle identification (PID) requirements in the backwards region. Driven mostly by SIDIS measurements, the requirements in the pseudorapidity range $-3.5 \leq \eta \leq -1.5$ demand 3σ separation or better of $\pi/K/p$ for momenta $p < 7$ GeV/c. Evaluations of particle yields and coverage of the relevant SIDIS phase space have shown that the lack of hadron PID capability for $p > 7$ GeV/c in the pfRICH acceptance will have little effect on the EIC physics program.

The Yellow Report enumerated overall requirements on the e/h ratio and identified the need for hadron suppression on the order of 10^4 in the backward region. At high momenta, this suppression will be predominantly provided by the electromagnetic (EM) calorimeter but it is clear that at lower momenta the electron ID capabilities of the backward EM calorimeter will not be sufficient to achieve the overall required electron purity. The extra suppression power can only be met by additional PID capabilities from the RICH detector, especially in the region below 3 GeV/c where the hadron distributions are at their maximum. To access low Q^2, it is essential to provide PID in this region which includes $Q^2 = 1$ up to $\eta = -2$ and lower Q^2 up to the quasi-real photoproduction regime further backward. As low-Q^2 is correlated with low-x (at high inelasticity), e/h separation is essential to access the lowest x for the reasons outlined above.

The original baseline design of the ePIC detector included ToF detectors based on AC-LGAD technology in the forward, backward, and barrel regions. Their purpose was to provide PID in the momentum region below the aerogel threshold ($\lesssim 1$ GeV/c). While physics measurements exist that require PID at low momenta in the forward and barrel region, there are no such arguments for the backward range. The main argument for the presence of a ToF detector for $\eta < -1$ was to aid in providing the start time, t_0, for all ToF measurements in ePIC, mainly by utilizing the scattered electron. It was determined that the pfRICH, utilizing HRPPD sensors with a single photon timing resolution performance of $\sim$30-40 ps, could provide the same t_0 performance as a dedicated ToF system by using the copious amounts of Cherenkov photons produced as charged particles traverse the sensor fused silica windows. Thus, the dedicated backward ToF detector was removed from the ePIC baseline design meaning the pfRICH will need to provide the necessary t_0 with a resolution of $\sigma_t < 25$ ps. This, in conjunction with vertex-time correlations, will provide a high quality t_0 for events where the scattered electron is detected in the backward region. It will also provide input in cases where the t_0 has to be derived from a bootstrap method using all timing detectors in the full ePIC coverage.

Requirements from Radiation Hardness: Add text here.

Requirements from Data Rates: Add text here.

Justification

Device concept and technological choice: The operation of a generic proximity focusing RICH detector is based on a very simple set of principles. A charged particle passing through a thin layer of radiator (often aerogel with an appropriate refractive index) with a velocity higher than the speed of light in that medium emits Cherenkov light (photons) at an angle which is solely determined by the particle mass, momentum, and refractive index of the radiator. The 3D momentum of the particle is typically provided by a tracking system. If the average refractive index of the radiator is also known, measurements of the Cherenkov light emission angle can determine the particle mass, thus allowing identification of different particle species, e.g. distinguishing electrons, pions, kaons, and protons.

The ePIC pfRICH was designed as a conceptually simple detector, based on proven principles, providing a high degree of performance that is practically uniform over the whole available angular acceptance in η and ϕ. In order to reach the performance requirement of 3σ separation or better of $\pi/K/p$ for momenta $p < 7$ GeV$/c$, the pfRICH design was optimized in the following ways: (1) the proximity gap length was maximized as much as possible within the volume available in ePIC; (2) the radiator thickness was taken to be small enough to reduce the contribution to the single photon angular resolution to below $\sim$5 mrad, yet produce enough photons per track to robustly reconstruct the Cherenkov angle; (3) the HRPPD pixellation was chosen such that it contributes at most $\sim$2 mrad to the angular resolution; and (4) the acrylic filter cuts off all UV light produced in the aerogel below $\sim$ 300 nm, where the $dn/d\lambda$ dependency is strongest. In addition to satisfying the PID requirements in the backward direction, the small material budget of the pfRICH design minimizes the impact on the the resolution of the endcap electromagnetic calorimeter which sits directly downstream.

Subsystem description:

General device description: The layout of the proposed ePIC pfRICH detector is shown in Fig. 8.23. It consists of a 1.3 m diameter and $\sim$49 cm long cylindrical vessel with the outer and inner walls made from a lightweight honeycomb carbon fiber sandwich and front and rear plates made of a carbon fiber reinforced plastic (CFRP). The vessel sits 123.6 cm from the nominal interaction point. Forty-two 2.5 cm thick aerogel tiles of a trapezoidal shape are installed in individual opaque compartments in a container mounted on the upstream side of the vessel. A thin acrylic filter is installed immediately after the aerogel container. The vessel is continually flushed with dry purified nitrogen. Sixty eight HRPPD photosensors are installed in individual slots in the rear CFRP mounting plate with their fused silica windows facing the aerogel. Inner and outer conical mirrors cover the cylindrical sides of the vessel in order to increase the η acceptance of the Cherenkov photons produced in the aerogel radiator. Readout boards equipped with four 256-channel EICROC ASICs are mounted on the rear ceramic anode plates of each of the HRPPDs.

Sensors: An improved version of the Micro-Channel Plate Photomultiplier Tubes (MCP-PMTs) manufactured by Incom Inc. [12], the so-called High Rate Picosecond Photon Detectors (HRPPDs), will be used as the photosensor solution. The sensor dimensions will be 120 mm x 120 mm, with a 104 mm x 104 mm fully efficient active area in the center (75% geometric efficiency) and will have slightly tapered 5 mm thick UV-grade fused silica windows, and 3 mm thick multi-layer ceramic anode base plates. A DC-coupled variety of these sensors will be used, with the inner side of the anode base plate patterned into 32 x 32 square pixels, corresponding to 1024 channels per sensor, and a pitch of 3.25 mm. The sensors will be equipped with a UV-enhanced high quantum efficiency (QE) bialkali photocathode, with peak values exceeding 30% at 350 nm [13]. The HRPPDs will be fitted with a pair of 600 μm thick MCPs with a pore diameter of 10 μm, open area ratio in excess of 70%, and bias angle of 13 degrees in a conventional chevron configuration. These will be operated at an amplification voltage of up to $\sim$700 V to comfortably achieve an overall detector gain above 10^6 if needed. HRPPDs will have a single photon Transit Time Spread (TTS) of $\sim$30-40 ps. The an-

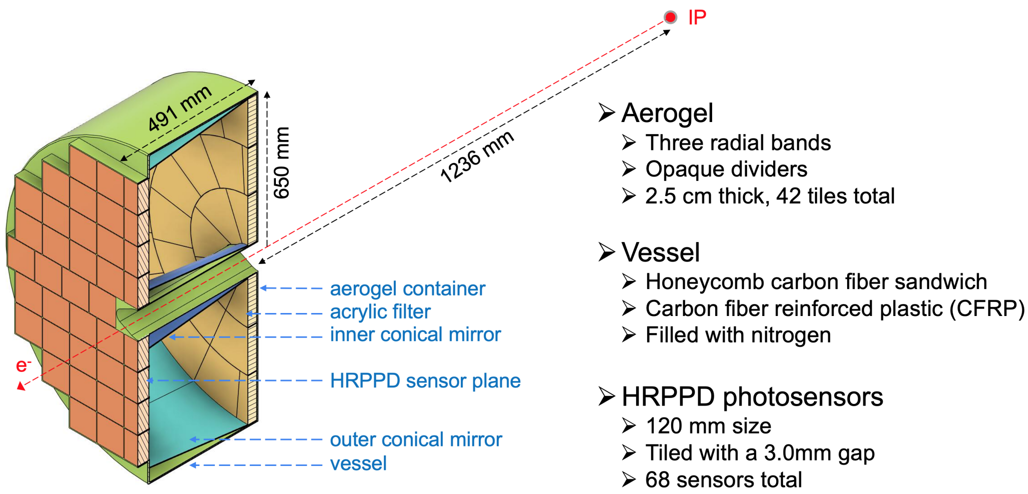

Figure 8.23: The proposed pfRICH detector. See the text for more details.

ode base plates will be manufactured from multi-layer High Temperature Co-fired Ceramic (HTCC) by Kyocera (Japan). They will have a custom design, matching the uniform 32 x 32 pixellation on the inner (vacuum) side of the sensor, short shielded traces inside of the ceramic stack, and a pattern of square pads with a smaller pitch on the outer side, matching the readout PCB design.

FEE: Each sensor will be equipped with four 256-channel EICROC ASICs [14], designed by the OMEGA group [15], each serving one quadrant of the sensor. EICROC ASICs will be built via a 130 nm technology process, with an expected power consumption of 1-3 mW/channel [14]. They will provide a Time of Arrival (TOA) and an ADC measurement with a dynamic range of 1 pC for each pixel, which should be sufficient for both single photon hits (both imaging and timing) and multi-photon hits (timing only) at a moderate HRPPD gain of a few times 10^5. The ASICs will be able to measure the TOA with a resolution better than 20 ps per pixel assuming detector capacitance on the order of $\sim$10 pF, leading edge length of the HRPPD signal below 500 ps, and collected charge of a few dozens fC achieved by tuning the MCP gain [15]. These ballpark parameters seem to be easily within reach for pfRICH HRPPD sensors.

The ASICs will be bump bonded to the readout PCB in a "flip-chip" fashion to minimize the parasitic capacitance of the traces inside of the PCB stack. Preliminary estimates show that in such a scheme, where four 16 x 16 primary pixel arrays with a pitch of 3.25 mm are first "compressed" to a 2.0 mm pitch inside the HRPPD ceramic base plate and then further reduced to a 500 μm pad size in the readout PCB stack in order to ultimately match the EICROC ASIC pitch, the combined pad and trace capacitance should not exceed 10 pF. This is well within the expected operating range of the ASICs.

Each ASIC will be connected via a dedicated copper link to its respective readout unit (RDO), located on the outer circumference of the rear side of the pfRICH vessel. Each RDO will serve 16 EICROC ASICs, for a total of 17 RDOs. The RDOs will then be connected to a single Data Aggregation Module (DAM). The DAM board is envisioned to be a FrontEnd LInk eXchange (FELIX) board [16] installed in the DAQ. The RDO will be connected to the DAM via a high speed optical link capable of at least 5Gb/s throughput. The RDOs will follow the same design used by the ePIC pixelated AC-LGAD detectors. These boards will utilize lpGBT for aggregation of ASIC data and VTRX+ to provide the fiber interfaces. The RDO should deliver timing signals synchronized to the beam crossings with jitter < 5ps.

Other components: In addition to the vessel structure and sensors described above, two other components will be critical to the pfRICH: the aerogel radiators and mirrors. The pfRICH will be equipped with aerogel tiles produced by Chiba Aerogel Factory Co., Ltd. [17] with a nominal refractive index, $n \sim 1.040$ and a thickness of 2.5 cm. The aerogel will be cut using a water jet technique into trapezoidal tiles providing a required radial and azimuthal segmentation with minimal dead area. This type of aerogel will replicate the performance of the material used in the Belle II experiment [18], and in particular, will be very transparent in the near UV range, with an absorption length and Rayleigh scattering length in excess of 5 mm down to $\sim$275-300 nm. The aerogel tiles will be installed in segmented containers (slots) with $\sim$500 μm thick walls and held in place with a thin filament. The container walls will be opaque to suppress stray photons leaking out of the aerogel tile side facets, which are not expected to be of a high optical quality after water jetting.

The pfRICH will also utilize three types of mirrors to increase the active acceptance of the detector. The outer mirror cone consists of 12 segments approximately 40 cm in length which sit just inside the outer wall of the pfRICH vessel. These mirrors will recover Cherenkov photons from charged particles with large polar angles which pass through the aerogel but would exit the vessel before reaching the sensor plane. Similarly, a set of inner mirrors which wrap around the beam pipe and surrounding support structures will reflect photons emitted by small angle charged particles (close to $\eta \approx -3.5$) back onto the sensor plane. Finally, small pyramidal mirrors will be placed on top of the HRPPD side walls to reflect (funnel) photons hitting this area back into the sensor acceptance. The mirrors themselves will have a reflectivity of approximately 90% for wavelengths between 300 and 600 nm and will be produced at Stony Brook University using an evaporator with the CFRP substrate material provided by Purdue University.

Performance

Implementation

Services: Services relevant for the pfRICH include High Voltage (HV) and Low Voltage (LV) systems to operate the photosensors and power the front-end electronics, respectively, a cooling system to regulate the temperature of the electronics and sensors, and a gas system to maintain the proper environment inside the pfRICH vessel.

The HV and LV modules will be located on the electronics platform, about 15 meters away from the pfRICH detector, in a low Total Ionizing Dose (TID) environment. Therefore, standard off-the-shelf units can be used. The high-voltage system will consist of 340 individual stackable negative HV channels. Twenty three CAEN A1515BV 16-channel 1.4kV/1mA floating ground modules [**?**] will be used. The HV modules will be housed in a pair of CAEN SY4527 mainframes [**?**], equipped with additional 1200 W power module boosters. Each of the twenty three modules will be connected to an enclosed box distribution PCB installed on the rear side of the pfRICH vessel. The box is fed from individual 15 m long multi-conductor high voltage cables. For the HV interconnect, CERN-approved 52-pin Radiall cable connectors and receptacles will be used throughout the system. The distribution PCB will arrange five of the isolated channels of the A1515BV in a manner to provide five individual stacked voltage levels and a common ground referenced return to each HRPPD. The respective five bias levels and ground will be connected to the pads on the rear side of the HRPPDs via narrow profile Teledyne Reynolds shielded 26 AWG coaxial cables, conductive vias in the Front End Board (FEB) stackup with a matching pad pattern, and custom Samtec compression interposers.

The EICROC ASICs will require 1.2 V low-voltage power. Under the assumption of up to 3 mW/channel power dissipation this corresponds to 3 W power (or up to 2.5A current) per photosensor FEB. Accounting for other electronics components present on such a FEB, and providing a 20% safety margin, we estimate the total power consumption to be less than 300 W for the whole system. This number is used as input for designing the cooling system discussed below. We will be using a single Wiener MPOD Mini LX crate with a MPOD-C controller and four MPV4008I1 4-channel LV modules [**?**]. One Low Voltage channel will serve four FEBs. 15 m long tray rated 10 AWG jacketed cables with 20AWG (sense wires) will run between the electronics platform and a LV distribution panel on the rear side of the pfRICH vessel. From there, 18 AWG multi-conductor cables will distribute power to the individual FEB cards.

The pfRICH cooling system will consist of several off-detector components and a few on-detector thermal interfaces and assemblies. The primary heat dissipating components will be the ASICs, which are anticipated to produce just over 1 W each (4 W per module), or about 300 W for the 68 total modules. In addition to the ASICs, the sensors are anticipated to dissipate just under 1.5 W each or 100 W total. Conservatively, the total power output will be roughly 400 W. Following the geometry, each row of sensors will have its own pair of titanium cooling tubes directly over the ASICs. The pair of tubes that contact the same row of sensors will be in series, and all rows will be in parallel with each other. The tubes will be attached to aluminum plates with thermal epoxy, and a gap pad between the plate and ASIC will maximize thermal contact. Using a stock tube of 0.25″ OD and 0.218″ ID and maintaining a minimal temperature gradient in the water allows the mass flow rate to be calculated. From there the Reynolds number and pressure drop can be determined, confirming the viability of the system. Additionally, a finite element analysis (FEA) was performed to confirm the water temperature difference and determine the thermal gradient across the various components. With the described configuration, the sensors reach a maximum temperature of about 32 C in the analysis.

The three primary off-detector elements of the cooling system are a Polyscience chiller, Chilldyne circulator, and a distribution panel. The Polyscience chiller will allow the water to be slightly colder than room temperature, or about 15 C, which is the lowest recommended temperature without nearing the dewpoint in the interaction region. The unit is also capable of flowing about 10 liters per minute (lpm), dissipating about 800 W at that temperature and maintaining the temperature within +/-0.1 C. The Polyscience chiller would be paired with a Chilldyne negative pressure system capable of circulating water at about 8 lpm and $\sim$10psi. It offers a significant advantage over a positive pressure solution, as if there is a leak in the system, it will draw air into the tube instead of letting water out and potentially damaging electrical components.

The gas system for the pfRICH detector is designed to circulate dry nitrogen at precise pressure and flow rates to remove moisture from within the pfRICH chamber. High-purity nitrogen (H_2O $< 3\ ppm$) will be supplied from cryogenic sources. To provide secondary protection, moisture traps such as silica gel dryers will be installed near the nitrogen source. The system will maintain both the required moisture levels and gas purity by ensuring that it is sufficiently gas tight and that the chamber is kept at a slight overpressure (4 mbar) above atmospheric pressure, preventing any infiltration of ambient air. A 0.5 μm filter will be added near the source to capture dust particles. A standby nitrogen source will be available to ensure continuous operation in the event of a primary source failure. To manage fluctuations in the source pressure, a digital pressure outlet controller will be used. Additionally, nitrogen flow will be regulated by a non-pressure-limiting digital mass flow controller. The nitrogen flow rate is expected to allow several complete volume exchanges per hour, with the precise rate to be finalized later.

Pressure inside the chamber will be controlled using a tank blanketing pressure regulator, which maintains a positive internal pressure relative to varying atmospheric conditions. An overpressure protection bubbler will serve as a safeguard against excessive pressure within the chamber. To ensure uniform nitrogen distribution and prevent localized air pockets, nitrogen will be introduced into the chamber at two locations near the top side of the pfRICH vessel, closer to the aerogel plane, and exhausted through two openings near the sensor plane at the bottom. All exhausted gases will be vented outside the experimental area. The entire gas system will undergo pressure testing at 1.5 times the operating pressure to ensure integrity. For monitoring and troubleshooting, pressure gauges and transmitters will be installed, with critical data such as chamber pressure and flow archived for reference.

Subsystem mechanics and integration: Add text here.

Calibration, alignment and monitoring: Add text here.

Status and remaining design effort:

R&D effort: Add text here.

E&D status and outlook: Add text here.

Other activity needed for the design completion: Add text here.

Status of maturity of the subsystem: Add text here.

Environmental, Safety and Health (ES&H) aspects and Quality Assessment (QA planning: Add text here.

Construction and assembly planning: Add text here.

Collaborators and their role, resources and workforce: Add text here.

Risks and mitigation strategy: Add text here.

Additional Material Add text here.

8.3.4.3 The high performance DIRC

Requirements

Requirements from physics: Add text here.

Requirements from Radiation Hardness: Add text here.

Requirements from Data Rates: Add text here.

Justification

Device concept and technological choice: Add text here.

Subsystem description:

General device description: Add text here.

Sensors: Add text here.

FEE: Add text here.

Other components: Add text here.

Performance

Implementation

Services: Add text here.

Subsystem mechanics and integration: Add text here.

Calibration, alignment and monitoring: Add text here.

Status and remaining design effort:

R&D effort: Add text here.

E&D status and outlook: Add text here.

Other activity needed for the design completion: Add text here.

Status of maturity of the subsystem: Add text here.

Environmental, Safety and Health (ES&H) aspects and Quality Assessment (QA planning: Add text here.

Construction and assembly planning: Add text here.

Collaborators and their role, resources and workforce: Add text here.

Risks and mitigation strategy: Add text here.

Additional Material Add text here.

8.3.4.4 The dual radiator RICH

Requirements

Requirements from physics: Add text here.

Requirements from Radiation Hardness: Add text here.

Requirements from Data Rates: Add text here.

Justification

Device concept and technological choice: Add text here.

Subsystem description:

General device description: Add text here.

Sensors: Add text here.

FEE: Add text here.

Other components: Add text here.

Performance

Implementation

Services: Add text here.

Subsystem mechanics and integration: Add text here.

Calibration, alignment and monitoring: Add text here.

Status and remaining design effort:

R&D effort: Add text here.

E&D status and outlook: Add text here.

Other activity needed for the design completion: Add text here.

Status of maturity of the subsystem: Add text here.

Environmental, Safety and Health (ES&H) aspects and Quality Assessment (QA planning: Add text here.

Construction and assembly planning: Add text here.

Collaborators and their role, resources and workforce: Add text here.

Risks and mitigation strategy: Add text here.

Additional Material Add text here.

8.3.5 Electromagnetic Calorimetry

Add text here.

8.3.5.1 The backward endcap electromagnetic calorimeter

Requirements

Requirements from physics: Add text here.

Requirements from Radiation Hardness: Add text here.

Requirements from Data Rates: Add text here.

Justification

Device concept and technological choice: Add text here.

Subsystem description:

General device description: Add text here.

Sensors: Add text here.

FEE: Add text here.

Other components: Add text here.

Performance

Implementation

Services: Add text here.

Subsystem mechanics and integration: Add text here.

Calibration, alignment and monitoring: Add text here.

Status and remaining design effort:

R&D effort: Add text here.

E&D status and outlook: Add text here.

Other activity needed for the design completion: Add text here.

Status of maturity of the subsystem: Add text here.

Environmental, Safety and Health (ES&H) aspects and Quality Assessment (QA planning: Add text here.

Construction and assembly planning: Add text here.

Collaborators and their role, resources and workforce: Add text here.

Risks and mitigation strategy: Add text here.

Additional Material Add text here.

8.3.5.2 The barrel electromagnetic calorimeter

Requirements

Requirements from physics: The Barrel Electromagnetic Calorimeter (BEMC) must meet the stringent physics requirements set by the EIC program. It needs to identify scattered electrons and measure their energy, particularly in high Q^2 events, and also detect decay electrons from vector or heavy flavor meson decays, as well as DVCS photons (G-DET-ECAL-BAR.1). Electron identification, including electron-pion separation, is required up to 50 GeV and down to 1 GeV (F-DET-ECAL-BAR.1), with an energy resolution better than $10\%/\sqrt{E} \oplus (2–3)\%$ (P-DET-ECAL-BAR.1). Additionally, the BEMC must provide photon reconstruction from 100 MeV to 10 GeV (F-DET-ECAL.9, F-DET-ECAL-BAR.2). The system must also achieve photon-pion discrimination (γ/π^0 separation) up to 10 GeV, with the ability to distinguish two showers with an opening angle down to 30 mrad (P-DET-ECAL-BAR.3). Furthermore, the BEMC will assist with muon identification (G-DET-ECAL-BAR.3) and provide a charged tracking point behind the DIRC to help with charged hadron PID (P-DET-ECAL-BAR.4), with a spatial resolution of less than 150 μm. Lastly, the system must have sufficient dynamic range to detect MIP signals (P-DET-ECAL-BAR.5).

Requirements from Radiation Hardness: The BEMC must be designed to operate in an environment where it may experience radiation levels of up to about 3.9×10^9 1-MeV neutron equivalent per cm^2 per year of running (6 months), corresponding to full luminosity and background conditions (F-DET-ECAL.6). All components, including sensors, electronics, and structural materials, must be sufficiently radiation-hardened to maintain performance under these conditions. This includes ensuring that the sensor response, energy resolution, and position reconstruction capabilities remain stable throughout the detector's operational lifetime.

Requirements from Data Rates: The BEMC and its readout technology must be designed to handle the high event rates expected at full luminosity, ensuring stable performance under expected background conditions, including radiation doses and neutron flux (F-DET-ECAL.6). The system must provide sufficient timing resolution to accurately discriminate between different bunch crossings (F-DET-ECAL.10), ensuring precise event separation and minimizing pile-up effects. The chosen detector and readout technologies must be capable of processing the high data rates without compromising performance or data integrity.

Justification

Device concept and technological choice: The ePIC BEMC is called the Barrel Imaging Calorimeter (BIC). The BIC combines two proven technologies to meet the stringent requirements of the EIC physics program. The first is a lead-scintillating fiber (Pb/ScFi) sampling calorimeter, providing robust energy measurement through light collection, based on the well-established GlueX Barrel Calorimeter (BCAL) design. This technology offers a reliable solution for high-resolution energy measurements, benefiting from its extensive use in other experiments.

The second key component is the AstroPix monolithic CMOS silicon sensors, which are interleaved with the Pb/ScFi layers to provide precise 3D imaging of particle showers. This hybrid approach enables excellent spatial resolution and position reconstruction, critical for separating particle showers and achieving the necessary photon and electron identification capabilities. AstroPix sensors, developed for the NASA space mission AMEGO-X, offer low power consumption, radiation tolerance, cost-effectiveness, and scalability, making them ideal for large-area applications in a high-radiation environment. For the AstroPix chip parameters refer to Tab. 8.5.

This combination of Pb/ScFi for energy resolution and AstroPix for spatial resolution was chosen to balance performance, cost-effectiveness, and long-term reliability under the expected operational conditions at the EIC.

Parameter	AMEGO-X Mission Requirements	BIC Requirements
Pixel size	500 μm x 500 μm	same
Power usage	$<$ 1.5 mW/cm^2	$\sim$ 2 mW/cm^2 acceptable
Energy resolution	10% @ 60 keV	same
Dynamic range	25-700 keV	same
Passive material	$<$ 5% on the active Si area	same
Time resolution	25 ns	3.125 ns (available in v5)
Si Thickness	500 μm	same

Table 8.5: Comparison of AstroPix requirements for AMEGO-X and BIC.

Subsystem description: The Barrel Imaging Calorimeter (BIC) consists of 48 trapezoidal sectors, with End-of-Sector Boxes (ESBs) at each end for readout. The calorimeter spans 17.1 radiation lengths (X_0) at central pseudorapidity, with the first layer being an AstroPix imaging layer, which provides a tracking point behind the DIRC. Each sector has six slots for AstroPix imaging layers, separated by 1.45 X_0 of Pb/ScFi at $\eta = 0$. In the baseline configuration, slots 1, 3, 4, and 6—counting radially outward—are filled with AstroPix sensors, while slots 2 and 5 are designated for future upgrades. Figure 8.24 presents the overall structure of BIC and its sectors.

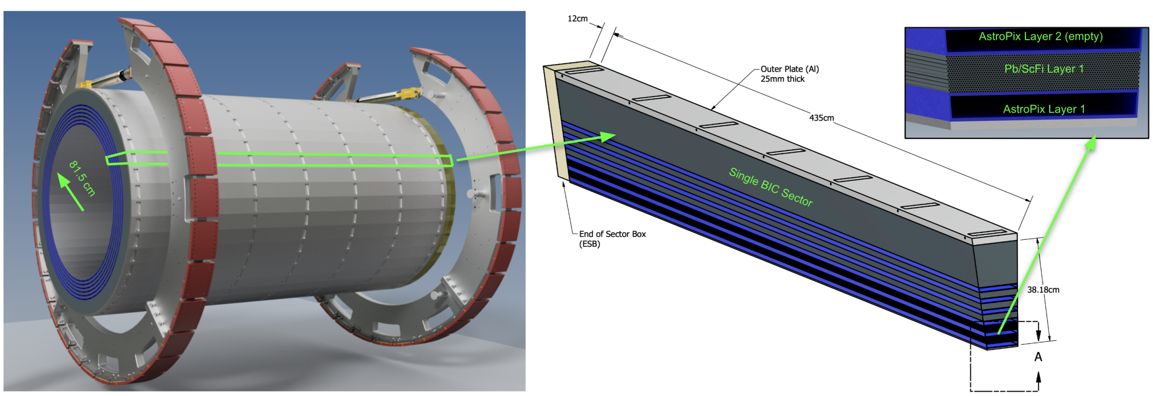

Figure 8.24: Drawing of the Barrel Imaging Calorimeter with its 48 sectors. The central drawing shows the structure of a single sector, featuring interleaved Pb/ScFi layers and slots for trays holding AstroPix chips, followed by the Pb/ScFi bulk section. On the right, a zoomed view of the first radially layers is presented.

Scintillating fibers for Pb/ScFi: The Pb/ScFi calorimeter system is based on the GlueX model with fibers positioned parallel to the z-direction with 2-sided readout for energy measurement and position reconstruction along the fiber. We will use single-clad scintillating fibers with 1 mm diameter embedded in lead and glue to provide reliable energy measurement through light collection.

Sensors for Pb/ScFi: The light from the scintillating fibers is subdivided into 12 rows of 5 columns per sector-end by light guides, which are optically coupled with cookies to the

SiPMs. These sensors have a 50 μm pixel pitch to optimize dynamic range and photon detection efficiency.

FEE for Pb/ScFi: The FEE for the Pb/ScFi system, based on the CALOROC ASIC, processes the signals from the SiPMs. It provides sufficient time resolution for determining the z-position of events within the scintillating fiber, while maintaining low noise and high radiation tolerance.

Sensors and modules for imaging layers: The imaging layers use AstroPix monolithic silicon sensors with a 500 μm pixel pitch, interleaved with the Pb/ScFi layers. These sensors are glued on a base plate and daisy-chained on a flexible PCB to form a module containing 9 chips, providing high-resolution spatial information for 3D imaging and particle identification.

Staves and trays: Each stave is formed by daisy-chaining 12 AstroPix sensor modules. A tray holds 6–7 staves based on the layer position, with each tray being half of the sector length and read out at its respective end in the ESB. This modular structure allows for flexible scaling and future upgrades to the system.

End-of-Tray Card (ETC): The ETC functions as the RDO unit in the ePIC DAQ scheme. It manages signal processing, data formatting, and communication with the DAM, ensuring efficient and reliable data flow from the sensors.

Detector parameters	**Value**
Active length (z-direction)	435 cm
Inner radius	81.5 cm
Number of sectors	48
η coverage	$-1.71 \lesssim \eta \lesssim 1.31$
Radiation Length X_0	1.45 cm
Total depth in X_0	from 17.1 ($\eta = 0$) to 42 ($\eta = -1.55$)
Molière radius	4.5 cm
Total sampling fraction of Pb/ScFi layers	about 9.5%, see Fig. 8.25
Total sampling fraction of AstroPix layers	$< 0.4\%$
Scintillating fibers	$\varnothing$ 1 mm, single clad fibers
Light guide length	5 cm
Number of light guides	60 per sector per side
Monitoring system	Blue LED, one LED per light guide
SiPMs	1.2×1.2 cm^2 arrays, 50 μm pixel
Number of SiPMs	60 arrays per sector per side

Table 8.6: Selected BIC Parameters.

Performance Performance of BIC and its components has been tested at the bench and in beam tests at Fermilab Test Beam Facility and Hall D of Jefferson Lab. Selected performance results based on realistic simulations benchmarked against data are presented in this paragraph. Results from the beam and bench tests are covered in the R&D paragraph.

The realistic BIC geometry was implemented, including a detailed Pb/SciFi matrix with single cladded fibers embedded in lead and glue, following the GlueX model. The AstroPix layers were implemented as staves, with AstroPix chips placed in realistic dead areas, and materials accounted for the sensors, electronics, cables, insulation, glue, and support structure. Realistic digitization and reconstruction were applied. For the Pb/SciFi component, an effective model for light attenuation in the fibers, photoelectron statistics, light guide efficiency, and SiPM thresholds was implemented based on beam and bench measurements as well as optical simulations. For AstroPix, each digitized readout unit corresponds to one pixel, while for the Pb/SciFi component, each readout cell covers the area of one light guide with an attached SiPM. More details about the specific implementations, benchmarks, and simulated performance described in the following paragraphs can be found in the Additional Material.

Energy resolution The energy resolution of the Pb/ScFi layers has been simulated within the full ePIC framework for different rapidity ranges and photon and electron energies. The energy response, corrected for the sampling fraction, was fitted using the Crystal Ball function, and the energy resolution was extracted as the σ of the Gaussian core of the fitted function. The obtained energy resolution is presented in Fig. 8.25 (a) and the results of the fitted stochastic and constant parameters a and b of the energy dependence $\sigma/E = a/\sqrt{E} \oplus b$ are presented in Tab. 8.7. The sampling fraction defined as energy deposited in the scintillating fibers divided by the true energy of generated photons is presented in Fig. 8.25 (b). The contribution of the low-energy tail of the energy losses was quantified and is presented in Additional Material together with the results for electrons. The expected energy resolution fulfills the detector requirements.

η **range**	$a/\sqrt{E}$ **[%]**	b **[%]**
$(-1.7, -1.3)$	6.60 ± 0.03	0.66 ± 0.04
$(-1.3, -0.88)$	6.11 ± 0.01	1.24 ± 0.01
$(-0.88, -0.4)$	5.91 ± 0.02	1.24 ± 0.02
$(-0.4, 0)$	5.85 ± 0.01	0.88 ± 0.02

Table 8.7: Fitted energy resolution parameters for photons in BIC for different η ranges.

Energy response to both electromagnetic and hadronic showers has been also tested in the beam test environment with a 60 cm long and 15.5 X_0 deep Pb/ScFi bulk-section prototype based on GlueX BCAL geometry, termed *Baby BCAL*. At Hall D of Jefferson Lab, Baby BCAL was exposed to 3-6 GeV positrons hitting it at different impact angle and position depending on beam energy. Figure 8.26 (a) presents the measured energy resolution measured in those conditions. Note that the highest energy points reflect positrons hitting the prototype close to the end and at the impact angle that causes partial shower leakage. At Fermilab Test Beam Facility, Baby BCAL was exposed to mixed electron-pion-muon beam at energies of 4, 6, 8 and 10 GeV. The energy response to pion beam has been benchamrked in simulation of Baby BCAL implemented in ePIC environment, same as used for the BIC simulations. Fig. 8.26 (b) shows comparison between collected data and simulations benchmarking their realism.

Angular resolution The angular resolution for photons has been estimated using the AstroPix layers, based on full detector simulations across different rapidity ranges as a function of energy. The difference between the true and reconstructed azimuthal (θ) and polar (ϕ) angles has been extracted to assess the resolution as full-width-at-half-maximum (FWHM). In the current reconstruction algorithm, the angles are reconstructed from the hit with the maximal energy deposit in the AstroPix layer where the shower started. The resolutions for θ and ϕ are presented in Fig. 8.27. The results indicate a small dependence of the angular resolution on η. In all regions,

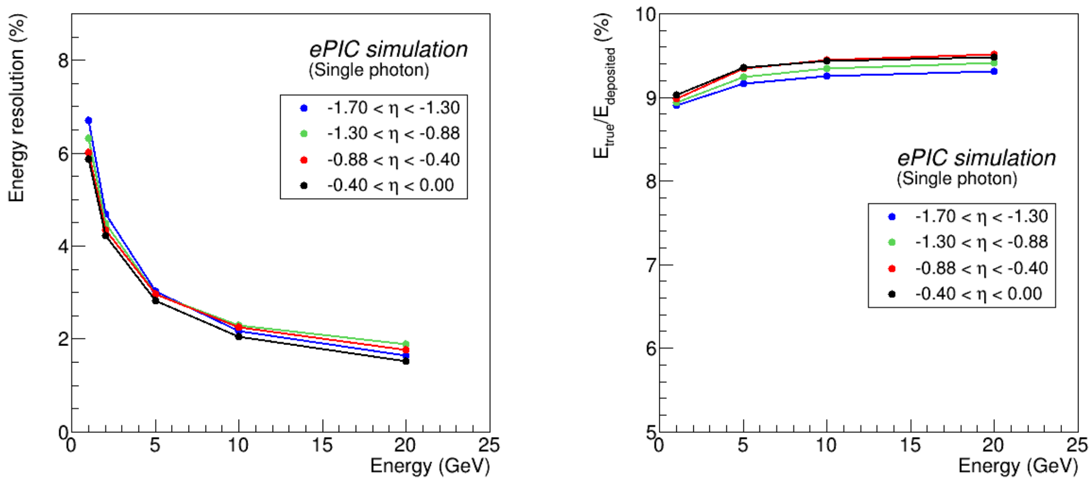

(a) (b)

Figure 8.25: (a) Simulated energy resolution in from Pb/ScFi extracted as a σ of the Gaussian core of the Crystal Ball fit to the energy deposits of photons in different rapidity ranges at BIC. (b) Sampling fraction for photons, defined as energy losses in scintillating fibers divided by the true photon energy, as a function of photon energy in different rapidity ranges. (To be replaced with matching η regions and adjusted y-axis)

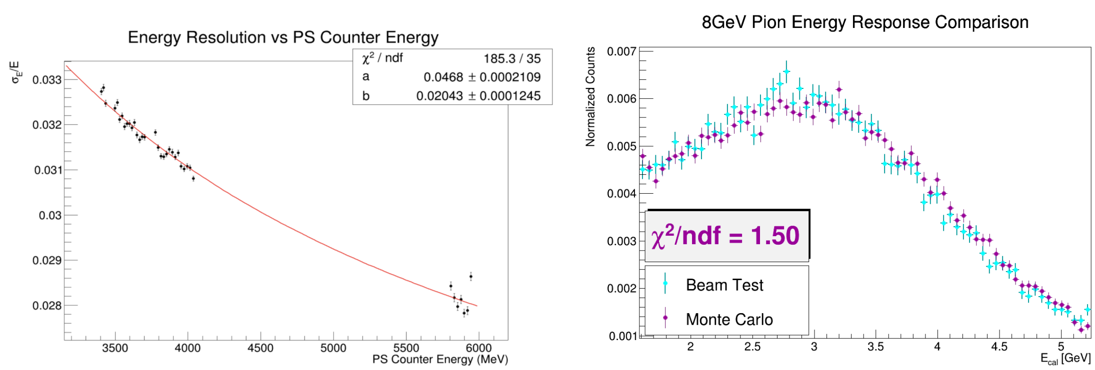

(a) (b)

Figure 8.26: (a) Preliminary energy resolution of Baby BCAL exposed to 3-6 GeV positrons at Hall D of Jefferson Lab, with varying impact angles and positions depending on beam energy. The highest energy points correspond to positrons striking near the end of the prototype and at angles causing partial shower leakage. Red line shows the fitted function $\sigma/E = a/\sqrt{E} \oplus b$. (b) Preliminary energy response of Baby BCAL to an 8 GeV pion beam at the Fermilab Test Beam Facility. The plot compares the collected data (light blue) with simulations (purple) implemented in the ePIC environment, as used for BIC simulations, benchmarking the realism of the simulation model.

the angular resolution remains well below 0.1 degrees, which is on the level of single pixel resolution. The example fit of the θ resolution in the rapidity region of $-0.88 < \eta < -0.4$ gives $(0.040 \pm 0.004)\ \mathrm{deg}/\sqrt{E} \oplus (0.016 \pm 0.003)$ mm The ϕ resolution is worse than the θ resolution due to the smearing of shower particles by the magnetic field. Overall, the results show significantly better performance than what can be achieved with any tower-like calorimetry systems and fulfills the requirements for the barrel electromagnetic calorimetry for the EIC.

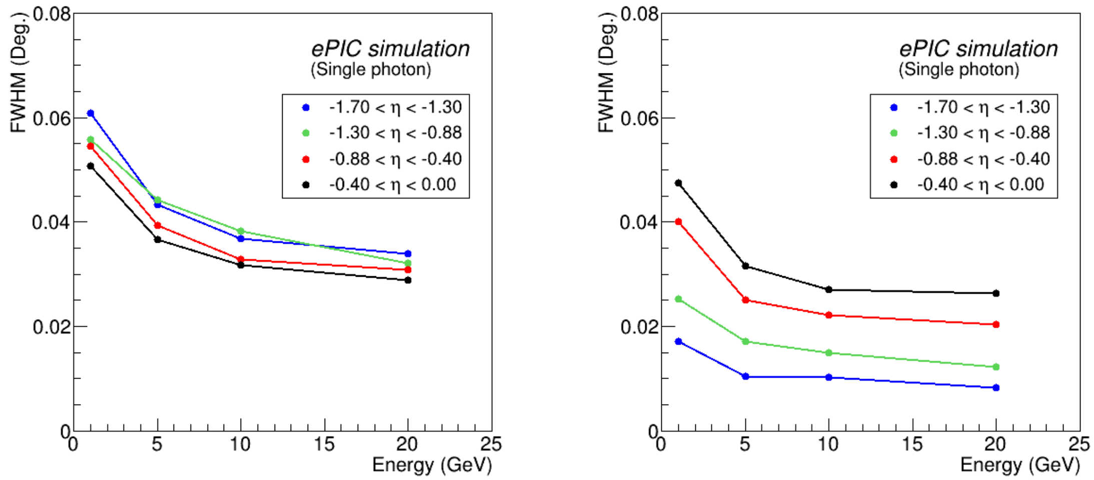

(a) (b)

Figure 8.27: Simulated angular resolution for photons at different energies for the ϕ (a) and θ (b) angles reconstructed form the maximal-energy pixel from the first AstroPix layer where the shower started. The resolution is taken as FWHM from the distribution of the difference between true and reconstructed angle.

Particle identification The design of the barrel calorimeter aims to provide high π^-/e^- separation, particularly in the momentum region below 5 GeV. The AstroPix layers capture snapshots of electromagnetic and hadronic showers, allowing for the reconstruction of a 3-dimensional profile of the shower development, supported by the longitudinal energy profiles from the Pb/ScFi layers. A deep-learning algorithm is employed alongside the traditional E/p cut to achieve accurate electron identification, meeting the detector requirements.

Charged pion rejection is carried out in a two-step process. First, an E/p cut is applied to the cumulative energy deposit in the Pb/ScFi layers. This cut is deliberately loosened to ensure high electron efficiency. The "cleaned" samples, following the E/p cut, are then fed into a classification neural network for supervised training to distinguish between electrons and pions. We used a 10-layer Visual Geometry Group-style Convolutional Neural Network to analyze combined AstroPix and Pb/ScFi data. The network utilizes energy and position features from both technologies capturing energy and spatial shower details. Future improvements may come from using Graph Neural Networks or Point Clouds.

The charged pion suppression factor for $\eta = 0$ rapidity is shown in Fig.8.28 (a), for a target 95% electron efficiency. The rejection exceeds 10^3 at low to mid energies, where rejection is most critical. For comparison, results from the upgraded system with six imaging layers are also presented.

The upper limit of the probability of merging two γs from a π^0 decay into one cluster at $\eta = 0$ is shown in Fig. 8.28 (b). Neutral pions decaying into two γs were simulated with various momenta. In different calorimeter technologies based on tower geometry, as outlined in the EIC Yellow Report [2], the separation criterion requires that the two γs be separated by at least one tower size. However, for the BIC technology, which uses granular position information from AstroPix, a different criterion has been established. The probability of merging two γs was determined using a separation of 6 times the FWHM of the shower profile, measured at the third imaging layer (where more than 90% of photons with energies above 0.5 GeV register at least one hit), providing a conservative estimate.

The upper limit for γ/π^0 separation is expected to be well above 10 GeV, based on studies incorporating AstroPix's position resolution and shower profile data. Additionally, initial results from a neural network approach, similar to the e/π studies but simplified for neutral pion identification, were applied using full detector simulations. Preliminary results suggest a pion rejection rate of approximately 82% at 90% electron efficiency for 10 GeV pions, based on the current status of model training.

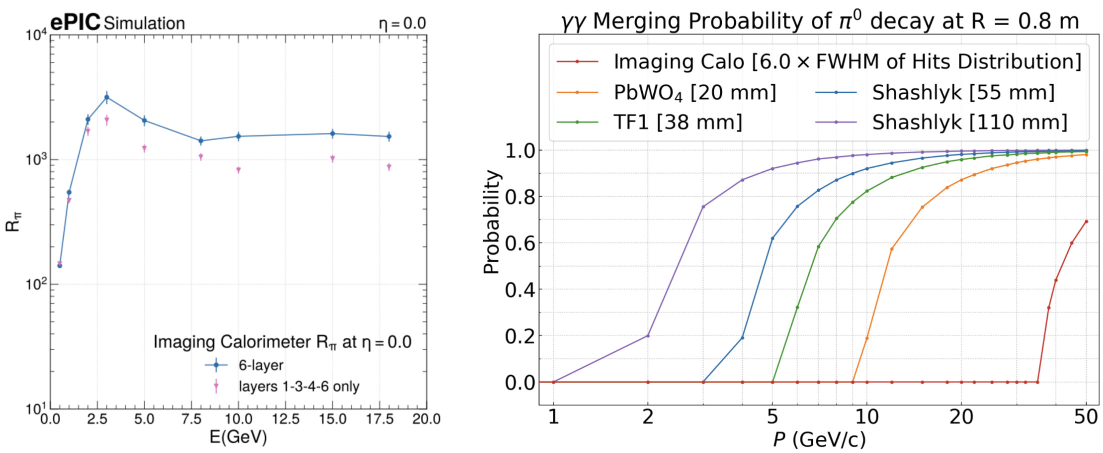

(a) (b)

Figure 8.28: Simulated performance on particle identification from BIC. (a) The charged pion suppression factor for $\eta = 0$ rapidity for 95% electron efficiency as a function of particle energy E. Pink points show the baseline performance where slots 1, 3, 4, and 6, counting radially, of imaging layers are filled with AstroPix trays, blue points show performance with 6 imaging layers. (b) Upper limit on cluster merging at $\eta = 0$ (shortest distance for particles to travel about 80 cm) from 2 photons from π^0 decay at particular π^0 momentum P. For calorimeter technologies based on tower geometry from [2] the separation by at least one tower size is required. For BIC the separation based on shower profile was assumed (see text). (To be replaced by the NN results with full simulation when ready)

Low energy response The performance of the Barrel Imaging Calorimeter (BIC) for detecting minimum ionizing particles (MIPs) was evaluated through simulations using 5 GeV muons at various rapidities. The deposited energy per readout cell, represented by the most probable value of the MIP peak, was extracted from simulations with Single-Clad Kuraray fibers that meet the FDR fiber specifications. This was compared against the 4-sigma pedestal peak from S14161-3050-04 SiPM array simulations, which also fulfill FDR specifications. Even with the dark count rate corresponding to the irradiation level of 1×10^9 1-MeV neq/cm^2, the MIP signal remains well-detectable with a 4-sigma cut on the pedestal. Figure 8.29 shows the extracted most probable value (MPV) of the MIP peak in terms of the number of photoelectrons (nphe) for muons at $\eta = 0$, which is the case where we observe the least photoelectrons from muons due to the combination of the distance the light has to travel in the fibers and the energy muons deposit at this angle in one Pb/ScFi layer. The pedestal 4-sigma value is marked in red. An example pedestal and MIP signal spectrum for 9 and 12 phe MIP signals, showing the worst-case scenario for the back Pb/ScFi layer of the BIC, is also presented.

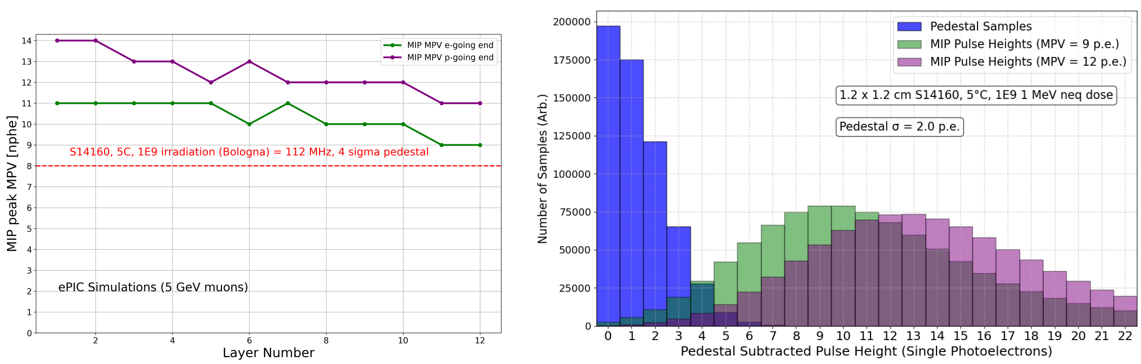

(a) (b)

Figure 8.29: Simulated performance on MIP response in BIC. (a) The most probable value of the MIP peak in terms of the number of photoelectrons for 5 GeV muons at $\eta = 0$ at each of the BIC layers. The red line corresponds to 4 sigma of the pedestal simulated with realistic S14160 family SiPM responses at 5 degrees Celsius, irradiated with a dose of 1×10^9 1-MeV neq/cm^2. The green line corresponds to the electron-going end, while the purple line corresponds to the proton-going end readout cells. (b) An example spectrum of the pedestal and MIP pulses at 9 and 12 phe signals, showing the worst-case scenario from plot (a) for the back Pb/ScFi layer of the BIC at $\eta = 0$.

AstroPix chip performance studies The AstroPix chip has been extensively tested in both bench and beam environments. The AstroPix_v3, the first full-size chip with a 500 µm pixel pitch and row-and-column readout (35 rows and columns in a strip-like format), has demonstrated strong performance, as summarized, for example, in [19]. Key tests included a noise study and a radiation source test. In the noise study, less than 0.5% of the pixels exhibited a noise rate exceeding 2 Hz, with the chip's dynamic range starting at 25 keV, allowing thresholds over 200 mV above the baseline. These results meet the BIC's requirements for low energy thresholds and masked pixel yield. The radiation source test, using isotopes with calibration points ranging from 22.2 keV to 122 keV, as shown in Fig. 8.30, showed that 44% of pixels met the 10% energy resolution requirement at 59.5 keV, and 92.4% of pixels achieved the required 25 keV sensitivity for BIC. Although the AstroPix_v3 chip is not fully depleted, it demonstrated promising performance. The upcoming AstroPix_v5, designed with a dynamic range extending to 700 keV, is expected to meet energy resolution requirements for all pixels.

Beam tests at Fermilab further validated the AstroPix_v3 chip in both single- and double-layer configurations. In the single-layer test, data collected with a 120 GeV proton beam was used to match corresponding row and column hits, using matching timestamps and ToT to reveal a hit map that showed the proton beam profile presented in Fig. 8.30. Although the AstroPix_v3 does not yet have pixel-level granularity (which is implemented in AstroPix_v4 and higher), it demonstrated a pixel-level position resolution. In the double-layer configuration, two daisy-chained layers of

AstroPix_v3 were tested, successfully reading events in coincidence and pinpointing hit pixel locations, providing a proof-of-concept for layer integration in a beam environment.

The characterization of AstroPix_v3 is ongoing, with specific tests designed to meet the ePIC detector requirements. Results show the chip is well-suited for the Barrel Imaging Calorimeter (BIC) and aligns with project goals. Remaining improvements, including enhanced dynamic range and energy resolution, will be addressed in the upcoming AstroPix_v5, which is expected to be fabricated by early 2025.

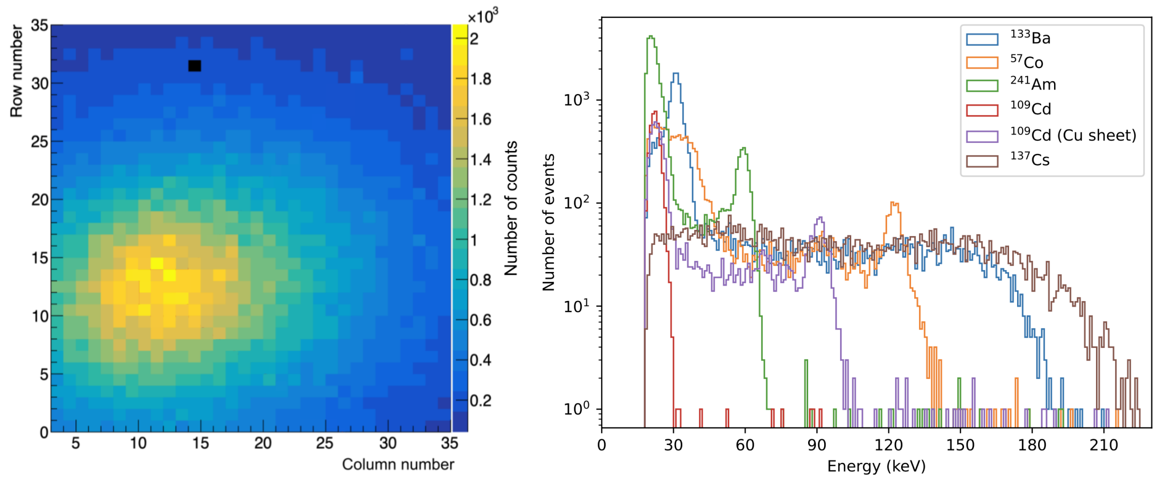

(a) (b)

Figure 8.30: (a) Beam hit map recorded in the 120 GeV proton run in Fermilab Test Beam Facility with a AstroPix_v3 chip. The masked pixel has been marked in black. (b) Calibrated energy responses form an example pixel of a AstroPix_v3 chip. Plot from [19].

Implementation

Subsystem mechanics and integration: The 48 BIC sectors are arranged in a self-supporting Roman arch configuration. Once assembled, the full calorimeter is supported by the solenoid cryostat support rings. In the hadron-going direction, a small gap must be bridged between the end of the BIC and the support ring, while in the lepton-going direction, the system slightly overhangs, creating a cantilevered structure.

A BIC sector consists of six carbon fiber frames for the imaging layers, interleaved with five single layers of a Pb/ScFi matrix (17 fibers tall), followed by a bulk segment consisting of seven Pb/ScFi matrix layers. The back of the sector consists of an aluminum support plate with connectors designed to link the sectors together, affix the ESB, and integrate with the global BIC support structure. The sector is constructed as a monolith, with all components epoxied together to ensure structural integrity.

The inner face of each BIC sector consists of a 0.5 cm thick aluminum plate, designed to connect the inner support rails to the detector. The inner support rails hold the inner detector support structure, maximizing the use of available space while avoiding obstruction of the ESBs (the readout boxes), ensuring that individual imaging layers can be added or removed as necessary for future upgrades or servicing. Hence, the BIC plays a critical role in supporting the overall inner detector structure.

Detailed FEA to validate the mechanical integrity of the sector design is ongoing. The design of the support that connects the BIC to the solenoid cryostat support rings is still under development, ensuring it meets the mechanical stability requirements while maintaining accessibility to readout electronics and other critical components.

Calibration, alignment and monitoring: The BIC calibration approach treats the Pb/ScFi and AstroPix imaging layers as two separate systems, each calibrated independently. For the Pb/ScFi calorimeter, we will follow well-established in-situ calibration methods, starting with MIP-based calibration, then refining with meson decays, electrons, and kinematic techniques derived from experiences with GlueX and HERA experiments. The energy calibration is further refined using decay photons from neutral pion events ($\pi^0 \rightarrow \gamma\gamma$).

For the AstroPix layers, the calibration process occurs in three steps. First, an absolute pixel energy calibration is performed during stave assembly using a radioactive source. Next, in-situ position and alignment calibration will be conducted similarly to standard tracker procedures, utilizing cosmics. Finally, the overall imaging cluster energy calibration will be matched with the Pb/ScFi calorimeter, leveraging the energy reconstruction methods described above.

Metrology will be used for alignment during installation, though very precise alignment is not critical, given the calorimeter's purpose. Cosmic and physics events will be used to calibrate the relative positioning of detectors and sensors, ensuring accurate reconstruction.

Calibration stability during operation will be ensured by using LED-based relative light monitoring systems for continuous monitoring, along with additional checks on linearity and timing using both cosmics and dedicated calibration runs.

Services: Add text here.

Status and remaining design effort:

R&D effort: The R&D efforts for BIC focus on demonstrating the combined performance of Pb/SciFi and AstroPix in EIC-like environments. This involves measuring higher than GlueX energy response up to about 10 GeV, benchmarking high-energy electron and pion simulations, testing AstroPix in high-rate environments, and integrating the Pb/SciFi with AstroPix sensor layers. In FY23, responses to 6 GeV positrons in 60 cm long Pb/ScFi prototype were measured in Hall D of Jefferson Lab, showing a constant term of about 2%, consistent with simulations. The Baby BCAL was commissioned with proton, pion, and electron beams during a June 2024 FBTF test, where data collected allowed for pion simulation benchmarking. A proof-of-concept synchronization of AstroPix with Baby BCAL was achieved by triggering on the AstroPix analog signal. With extensive data from previous AstroPix tests in FY23, the R&D is ready for multi-layer beam tests, to be conducted in early FY25 pending delays at FTBF.

E&D status and outlook: The Project Engineering Design phase of our project that started with granting the funding to the participating institutions starting Q4 2024, encompasses a detailed roadmap for the design, testing, and integration of key components for BIC. Early milestones focus on the design and development of the Pb/SciFi sector, including short and long test articles and the structural framework needed for housing these components. Alongside this, efforts are directed toward the design and prototyping of the end-of-sector box, which includes light guide and light monitoring systems integration. The tracking layer, which features AstroPix sensors, undergoes simultaneous development. This includes performance characterization of the AstroPix chips, module design and assembly, and testing of components such as bus tapes and end-of-tray cards. By mid-PED-phase, both the Pb/SciFi and tracking layers will undergo rigorous integration testing to ensure seamless functionality within the full detector system. The final phase focuses on validating the designs and performing full integration testing of staves, modules, and tracking layers. Quality control procedures will be established for each component, ensuring that everything meets performance specifications before final assembly. The PED phase is expected to finish in Q1 2026.

Other activity needed for the design completion: Within the small-scale R&D and design funding in Korea, a focused effort is underway during the period from August 2024 to April 2027, covering the PED phase and pre-production phase. The primary objectives include the development of testing and assembly systems for the AstroPix chip, particularly emphasizing automatic wafer testing and module assembly. Additionally, this work involves designing the readout box for the Pb/SciFi system and producing test modules to conduct performance studies.

Status of maturity of the subsystem: The maturity of BIC is currently estimated to be between 30% and 60%, depending on the specific component. The entire BIC underwent an incremental Preliminary Design Review (PDR2) in September 2024. Scintillating fibers and SiPMs have reached the final design stage, as they are classified as long-lead procurement items. Recognizing the extensive requirements for these materials—around 4500 km of scintillating fibers and a large quantity of SiPMs for ePIC—the project identified the need for early procurement. The Final Design Reviews (FDR) for both the scintillating fibers and SiPMs were successfully passed in September 2023. The first portion of the scintillating fibers was included in CD3a, with further procurement scheduled for CD3b. Vendor selection is nearly complete, and the first long-lead orders are expected by Spring 2025.

Construction and assembly planning:

Pb/ScFi Sectors Construction: The production of Pb/ScFi sectors will take place at Argonne, where there will be two production lines. The sectors will be constructed by embedding single-clad scintillating fibers in lead sheets, arranged in a stepped "Mayan pyramid" configuration, following the GlueX model. Carbon fiber frames will be integrated with the sector as it is built, with each frame assembled from two C-channel-like sides and a top and bottom plate. The sector construction process will proceed at a pace of 0.5 to 1 matrix layer per day, with the ability to build two sectors in parallel. Once a sector is fully assembled, it will be sent to an external machine shop for precise machining. Upon return to Argonne, the sector will undergo metrology and QC before being prepared for shipment to BNL.

ESB Manufacturing: The construction process for the ESB is still in development. ESB construction will include large-scale SiPM testing, SiPM mounting, light-guide manufacturing, light-monitoring system integration, construction of structural and cooling components, and manufacturing of electronics boards. There will be at least two ESB production sites: one in Canada at U. Regina and one in Korea. As the procedure is finalized, further details on assembly and integration will be specified.

AstroPix Wafers: The AstroPix wafers will be produced at the AMS foundry. Due to the large scale of the detector, automatic wafer-level testing will be conducted at two sites: PNU (South Korea) and Argonne. This testing will ensure the functionality of each chip before dicing, including measurements of pixel performance, noise levels, and defect detection early in the production process. After testing, the wafers will be diced into individual AstroPix chips.

AstroPix Modules and Trays: AstroPix chips will be assembled into modules at three production sites: Argonne, UC Santa Cruz, and PNU (South Korea). Each module will consist of nine AstroPix chips, daisy-chained on flexible PCBs. After assembly, each module will undergo initial testing to ensure proper chip-to-chip communication, pixel functionality, and noise levels. Modules that pass this stage will be integrated into staves, with 12 modules per stave. To keep the production process scalable and efficient, only one flavor of stave will be used across the entire system. The staves will then undergo additional QC testing. Once validated, the staves will be integrated into trays. There are two flavors of trays: one for the hadron-going side and the other for the lepton-going side of the detector, with each being a mirror image of the other. Each tray will contain 6–7 staves. These trays will then undergo final QC prior to shipping to BNL. The entire production and QC procedure is designed to catch any defects early and ensure that the trays are fully operational before final integration into the BIC sectors.

Assembly Planning: The assembly of the BIC will follow a carefully planned sequence. Upon arrival at the integration site, the Pb/ScFi sectors will be unpacked and prepared for assembly. The first step will involve attaching the light guides to the sectors. Once the initial sectors have been prepared, we can begin the barrel assembly while continuing to unpack and attach light guides to the remaining sectors. The BIC barrel will be assembled next to the solenoid and then inserted into the solenoid using existing sPHENIX tooling. Following the installation of the barrel, the imaging layer trays will be inserted using specialized tooling that is still under development. After all trays are installed, the electrical and cooling connections will be made, and the rest of the ESB will be installed to complete the installation. This phased approach ensures that all components are properly integrated before the system is brought online for testing.

Quality Control (QC) Planning: QC will be implemented at multiple stages of the BIC production and assembly process to ensure system integrity and performance. The system, particularly the imaging layers, is designed with both modularity and scalability in mind, allowing for efficient production, easier upgrades, and reworkability. Key QC procedures include:

Pb/ScFi Sector Assembly: The Pb/ScFi sectors will undergo thorough inspection during assembly. Scintillating fibers and lead sheets will be inspected for defects before embedding. After each matrix layer is completed, visual and metrological inspections will ensure proper alignment and uniformity. Final metrology checks will be performed after external machining to confirm dimensions prior to shipment.

AstroPix Wafer Testing: Automatic wafer-level testing will be conducted to assess chip functionality, including pixel performance, noise levels, and defect detection. Once tested, wafers will be diced, followed by additional electrical tests on individual AstroPix chips to ensure reliability before moving to the module assembly phase.

Module and Tray QC: Modules will be assembled from AstroPix chips and undergo functional tests to verify chip-to-chip communication, pixel functionality, and noise levels. Defective modules will be identified and replaced before progressing to stave assembly. Staves will be tested for electrical continuity, power consumption, and thermal performance under load. QC for staves and trays will use the actual readout electronics (ETC) to perform these tests. Once integrated into trays, final testing will check for alignment, electronic connectivity, and cooling performance, ensuring that trays operate as intended under operational conditions.

ESB QC: SiPMs will undergo rigorous testing to ensure proper photon detection efficiency, dark count rates, and timing precision before being integrated into the ESB. ESB integration with the sector first article will test the complete system, including electrical connections, data acquisition, and cooling systems, to ensure seamless functionality with the Pb/ScFi sectors.

Final Integration and Barrel Assembly: After attaching light guides to the Pb/ScFi sectors, alignment and metrology checks will be conducted during barrel assembly to ensure sector and tray alignment within tolerances. Electrical and cooling system checks will be completed post-installation to confirm proper functionality. System-wide tests, including cosmic ray runs and electronic readout, will validate the entire system before commissioning.

Environmental, Safety and Health (ES&H) aspects The BIC design incorporates standard safety and environmental practices across all production sites. We will strive for standardized safety protocols while adhering to internal work planning and control processes at each institution to identify hazards, implement mitigations, and document safety procedures. Main hazards associated with the BIC include:

Lead handling: The handling of lead sheets for the Pb/ScFi matrix requires careful consideration. We are working closely with experts to determine the appropriate safety steps. These steps may include specific protocols to mitigate any hazards and the potential enrollment of personnel in continuous health monitoring programs to ensure long-term safety.

Epoxy usage: Standard procedures for handling, mixing, and applying epoxy will be followed, with work conducted in fume hoods to ensure safety. Part of our PED work aims to deploy a custom mixing nozzle to reduce air contaminants and epoxy waste while improving consistency in the application process.

Scintillating fibers: The fibers are made of flammable polystyrene, and with the total fiber mass exceeding 3.9 tons, proper fire safety measures and storage protocols are essential.

Pinch/nip hazards: Automated systems, such as robots for wafer probing, pick-and-place, and glue application, present pinch hazards. Controls, such as guards and procedures, will be in place to mitigate these risks.

Crush hazards: The use of presses and swaging equipment introduces crush hazards during assembly processes. Strict safety protocols, including the use of guards and operator training, will mitigate these risks.

Radioactive sources: The use of radioactive sources for calibration introduces additional handling requirements, and proper shielding and storage protocols will be implemented as necessary.

Electrical safety: Electrical safety procedures will also be applied for all electronics and power systems associated with the BIC production tooling and detector components.

Collaborators and their role, resources and workforce: Add text here.

Risks and mitigation strategy: As outlined in the In the default scenario, sector production will take place at Argonne using two production lines, with one staffed by Korean collaborators. ESB production and quality control will be managed by Canada and Korea. Wafer testing will occur in both Korea and the US. AstroPix module and stave production will be distributed across three or more sites in the US and Korea. Depending on the level of in-kind funding, the baseline plan is to produce four to six layers. In the unlikely event of no in-kind funding, the project will cover all sector production labor costs, including Korean collaborators, and consolidate production to a single ESB site (Canada) and a single wafer testing site (US). AstroPix module/stave production will be limited to two sites in the US, requiring an increased workforce at each site or potentially facing a one-year delay to deliver the four baseline layers.

Additional Material

Subsystem description

- More detailed description of subsystems: sector, ESB, tray, module, chip
- More details on AstroPix chip with timelines
- More details on SiPMs
- More details on readout scheme ETC and CALOROC

Performance

Realism of simulations

- Geometry implementation description
- How light response is simulated: folded in measurements of nphe/GeV, fiber attenuation length, simulations of light guides and optical cookie, SiMP PDE and simulations
- Comparison of data from beam tests and simulations benchmarking their realism: response to electrons and pions

Energy resolution

- Evaluation of the energy response tail
- Simulated energy response to electrons
- Energy resolution for low energy photons
- Energy resolution from FTBF FY24 beam test.

The contribution of the low-energy tail of the energy losses was quantified by calculating the difference between the area under the fitted Crystal Ball function and that of its Gaussian core marked in red in Fig. 8.31 (a). The tail contribution to the overall energy loss area is shown in Fig. 8.31 (b) and (c) for electrons and photons, respectively. The results of energy resolution and total sampling fraction as a function of energy for electrons is presented in Fig. 8.32.

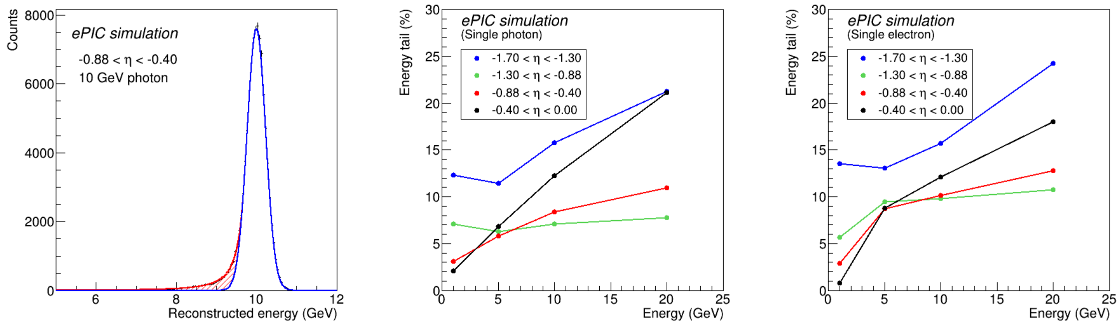

(a) (b) (b)

Figure 8.31: (a) Simulated energy losses in scintillating fibers of BIC for 10 GeV photons in the rapidity range $-0.88 < \eta < -0.4$. The distribution has been fitted with the Crystal Ball function; the Gaussian core of the function is marked in blue, and the power-law tail area is marked in red. (b) Percentage contribution of the low-energy tail–red area in plot (a)–to the overall area under the Crystal Ball fit to the energy losses of photon in Pb/ScFi as a function of photon energy and rapidity. (c) Same as (b) but for electrons.

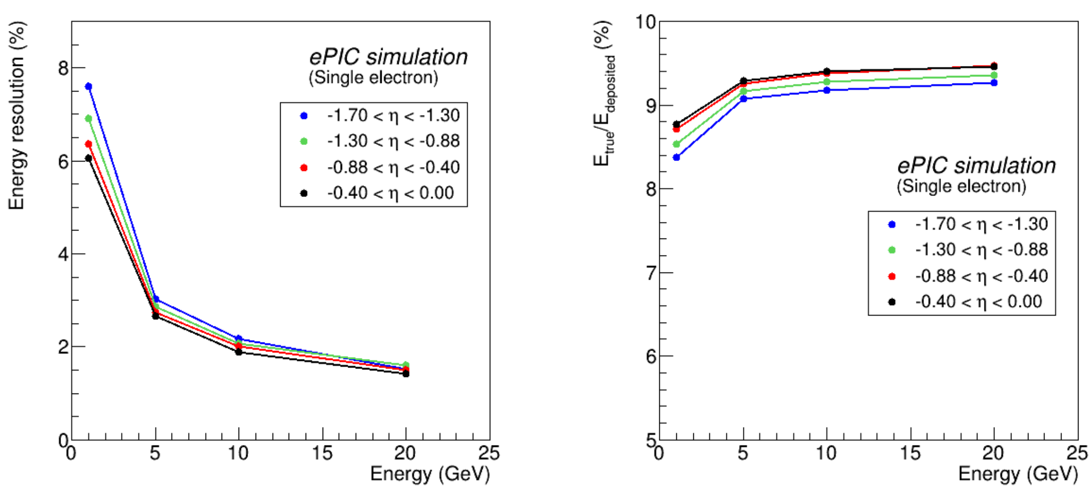

(a) (b)

Figure 8.32: (a) Simulated energy resolution in from Pb/ScFi extracted as a σ of the Gaussian core of the Crystal Ball fit to the energy deposits of electrons in different rapidity ranges at BIC. (b) Sampling fraction for electrons, defined as energy losses in scintillating fibers divided by the true photon energy, as a function of photon energy in different rapidity ranges. (To be replaced with matching η regions and adjusted y-axis)

Particle identification

- More details about the NN methodology
- Performance for different rapidity ranges and electron efficiencies
- Muon detection efficiency

For our π^-/e^- separation studies, we utilized a 10-layer Visual Geometry Group (VGG)-style Convolutional Neural Network (CNN) to process combined data from the AstroPix and Pb/ScFi parts of the calorimeter. This CNN architecture consists of 5 convolutional layers interspersed with 2 pooling layers, followed by 3 fully connected (dense) layers. Each event is formatted into an input array with dimensions $N_{\text{layers}} \times N_{\text{hits}} \times N_{\text{features}}$, where 4 primary features: energy deposit, η, ϕ, and radial position of the hit inside the calorimeter, to capture both energy deposition and spatial information about the particle shower.

We trained the network using supervised learning with a data set composed of a 10:1 ratio of pions to electrons. This ensured a sufficient number of pions remained after applying the energy-over-momentum (E/p) cut, which was crucial for training accuracy. Each training cycle consisted of 20 epochs, with data split into 70% for training, 10% for validation, and 20% for testing. On average, between 100,000 and 200,000 events were included in each training set, drawn from over 2TB of official singles productions simulations.

The CNN's performance is measured with uncertainties based on binomial statistics, providing robust estimates of classification accuracy. A similar but simplified approach was used for neutral pion identification. Initial results demonstrate promising pion rejection rates, which could be further enhanced by implementing algorithmic improvements. Future iterations of the model may explore Graph Neural Networks or Point Clouds to better capture the spatial and relational data inherent in these complex events.

MIP measurement capability

- More details about the SiPM simulations
- Performance for different rapidity ranges

Services and subsystem mechanics and integration

- More details about integration and services

Calibration, alignment and monitoring

- More details about calibration

Status and remaining design effort:

- Detailed timeline on R&D and PED efforts

Environmental, Safety and Health (ES&H) aspects and Quality Assessment (QA planning:

- Remaining details on ES&H

Construction and assembly planning:

- Full construction plan with sites, FTEs, yelds, etc

Collaborators and their role, resources and workforce:

- Full org chart

8.3.5.3 The forward endcap electromagnetic calorimeter

Introduction The ePIC forward electromagnetic calorimeter (fEMCal) is part of the hadron endcap calorimeter system, complementing the forward hadronic calorimeter. Complete calorimetric coverage in ePIC is essential for detecting photons and electromagnetically decaying mesons, which are crucial for reconstructing parton-scattering kinematics through jets and to identify DVCS photons. fEMCal provides full azimuthal coverage within a pseudorapidity range of approximately $1.4 \lesssim \eta \lesssim 3.9$. At lower pseudorapidity, fEMCal overlaps with BEMC, ensuring continuous coverage by electromagnetic calorimeters in the hadron side of the ePIC detector. Coverage at higher pseudo-rapidity is restricted due to mechanical limitations (clearance required to accommodate the accelerator beam pipe).

The design requirements for the fEMCal were established through extensive studies of various detector concepts proposed for the EIC over the past decade. These concepts originated from the designs presented in the EIC White Paper [20] and Yellow Report [2], evolving through the ECCE [21] and ATHENA [22] proposals and culminating in the ePIC detector concept discussed here. It was concluded that an energy resolution of approximately $12\%/\sqrt{E} \oplus 2\%$, along with high granularity needed to distinguish single photons from DVCS events and photon pairs from π^0 decays up to 50 GeV, would meet the EIC's measurement objectives.

Though numerous electromagnetic calorimeter technologies were considered, as noted in the EIC Yellow Report [2], the stringent space limitation in ePIC detector (an integration length of only 27 cm along the Z-axis for fEMCal) ruled out all but one technology for the fEMCal: WScFi. This technology, developed during the generic EIC detector R&D program [23], has also been successfully implemented in the recently constructed barrel electromagnetic calorimeter of the sPHENIX experiment [24], which is comparable in scope with the ePIC fEMCal.

Some of the key requirements and parameters for the fEMCal are summarized in Table 8.2. The most critical challenges include the limited integration space and the need for a very large dynamic range, approaching 7000:1. Radiation doses and neutron fluxes are not expected to pose significant challenges for current technologies. For instance, the forward calorimeter system (FCS) constructed for the STAR experiment at RHIC has been successfully operational since 2021 under conditions—both in terms of radiation and neutron flux—similar to those anticipated at the highest luminosities of the EIC. The choice of photodetectors and front-end readout electronics for the fEMCal is partially based on the readout system developed for the STAR FCS.

Table 8.8: Some requirements on performance of fEMCal and its parameters

Parameter	Requirements	Comments
Geometrical Acceptance	$1.4 \lesssim \eta \lesssim 3.9$	$R_{out} \sim 190$ cm, $Z_{frontface}$ ~341 cm
		Hole for the beam pipe 30×30 cm^2
Integration envelope	R_{max}=205 cm, Depth = 27 cm	
E_{min} in a single tower	15 MeV	Minimal shower energy 50 MeV
E_{max} in a single tower	100 GeV	18×275 GeV, ep
Maximum rate in a single tower	10 kHz	E_{thr}=15 MeV, 10×275 GeV ep
		500 kHh collision rate
Radiation doses	15 kRad	Integrated over 10 years
Neutron fluxes	4×10^{11} n/cm^2	1 MeV eq, integrated over 10 years
Energy resolution	$\lesssim 12\%/\sqrt{E} \oplus (2)\%$	Verified in the test beams
γ/π^0 separation	up to 50 GeV	$\sim$ 5% mis-identification at 50 GeV
Depth	23 X_0	Minimize leakages
Detector parameters	**Units**	**Comments**
X_0, R_m	7 mm, 19 mm	Rad. length, Moliere radius
f_{samp}	2%	e/h $\simeq$1 above 10 GeV
Scintillating Fibers	$\varnothing$ 0.47 mm	Single clad sc. fibers
Light yield	$\sim$ 1600 pixels/GeV	Test beam results.
Transverse size of tower	2.5 cm $\times$ 2.5 cm	Matches R_m
Transverse size of installation block	10 cm $\times$ 10 cm	Block of 16 towers
Total number of towers	18320	Readout channels
Photodetector	S14160-6015PS	Four 6×6 mm^2 SiPMs per tower
		15 um pixels size
Monitoring system	Blue LED	LED integrated on SiPM board.
		One LED per four towers

Device concept and technological choice: Figure 8.6 depicts the front face of the ePIC hadron end-cap in its closed position, which is divided into two halves to allow access to the inner ePIC detectors in its open position. The end-cap features 1,145 fEMCal installation blocks, each of which is mounted to a one-inch-thick steel plate situated between the hadronic and electromagnetic calorimeters. Each installation block comprises 16 fEMCal towers and weighs approximately 18 kilograms, bringing the total weight of the fEMCal to around 21,000 kilograms. A 0.250 mm air gap separates each fEMCal installation block to accommodate production and installation fixtures tolerances. The readout system for the fEMCal is located at the front face of the blocks, ensuring easy access to the electronics. Cables and utilities run horizontally along each row of blocks to the perimeter of the fEMCal, where they bunched and passed through few openings in the light-tight external shell and connected to the RDOs positioned on the sides of the hadron end-cap.

Each fEMCal installation block is composed of four "production blocks," with each production block consisting of a 2×2 arrangement of towers. All production blocks are identical, and precise mechanical tolerances are ensured by using identical production molds fabricated to high tolerances, within a few tens of micrometers. The epoxy layer between production blocks is typically less than 100 micrometers thick. These thin epoxy layers, along with air gaps between installa-

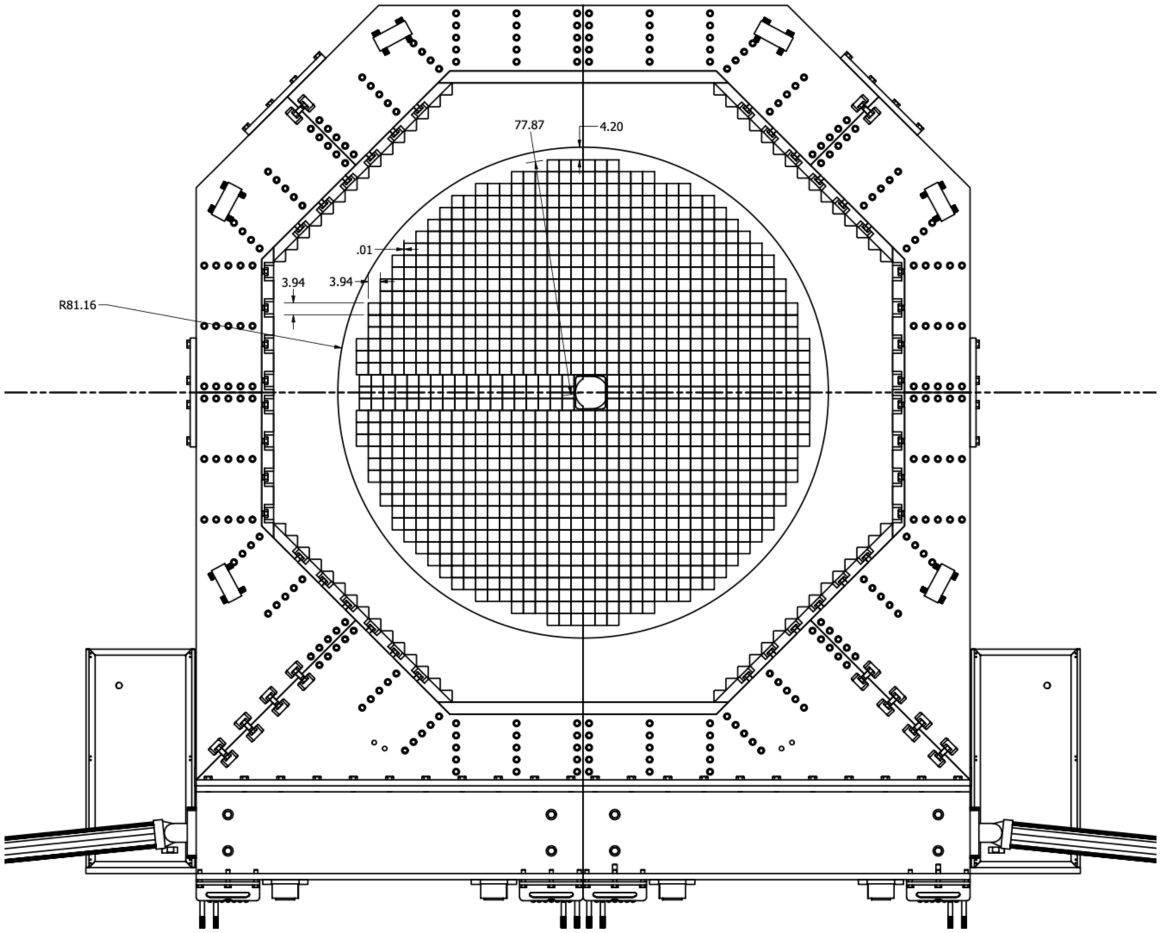

Figure 8.33: The front face of the ePIC hadron end-cap.

tion blocks, represent the only dead material within the fEMCal volume. These dead zones have a negligible impact on the overall performance of the fEMCal.

The primary reason for using tungsten powder and scintillating fiber technology for fEMCal is that it is the only practical method to meet the stringent requirements outlined in Table 8.2. Specifically, the desired energy resolution with extremely compact tower dimensions can only be achieved by combining a small sampling fraction with a high sampling frequency. This high sampling frequency is attained by using 780 thin, 0.47 mm diameter scintillating fibers in each tower, arranged in a staggered pattern with a center-to-center distance of approximately 0.955 mm. Both the fiber diameter and spacing were optimized through Monte Carlo simulations to ensure fEMCal is nearly compensated and maintains the required energy resolution. Tungsten powder is used as the base material for the absorber structure to make the technology viable in practice. A set of specifications for tungsten powder and scintillating fibers for ePIC were established during generic detector R&D program for EIC and experience of constructing sPHENIX barrel EMCal utilizing WScFi technology.

Despite the apparent simplicity of fiber calorimeters, constructing them is not straightforward. Detector components must be produced with extremely tight tolerances to maintain uniformity.

Historically, techniques like extrusion, machining, or rolling were used to manufacture absorber plates, but these processes were complex and often required the creation of specialized machinery and tools. Building fiber calorimeters has traditionally been a labor-intensive process, with individual detector elements being handled one at a time, driving up costs compared to scintillating plate detectors. Moreover, traditional methods face challenges with increasing sampling frequency, as thinner absorber layers and fibers become more difficult to produce and manage. For example, construction and assembly techniques for H1 fiber calorimeter detailed in [25].

Our approach differs in that we first create a matrix of fibers and then pour the absorber material into the matrix. Unlike previous methods, this technique eliminates the need to handle individual calorimeter elements separately. Figure 8.7 shows a matrix of scintillating fibers and SEM image of tungsten powder used to build fEMCal prototypes. This powder has a particle size distribution of 90% between 70 and 160 microns, a tap density of 11.5 g/cm^3, and a purity of W $\geq$ 99.9%, with Fe, Ni, and Co combined at $\leq$ 0.1%. Additionally, this tungsten powder exhibits excellent fluidity, a crucial property for our application. The only operation required for the absorber material is measuring the correct amount of powder before pouring it into the fiber matrix.

Figure 8.34: Matrix of scintillating fibers prepared to build production fEMCal blocks and SEM image of tungsten powder.

The second key element is a straightforward method for forming the scintillating fiber matrix. This matrix is defined by a set of precision brass meshes produced via photo-etching. These meshes have mechanical tolerances of 30 microns on their overall dimensions for 300-micron thick meshes and about 15 microns for the center-to-center distances between the holes for the scintillating fibers. The fibers are cut to the desired length using a thermo-cutter, which melts the fiber ends to form small drops that act as stoppers, preventing the fibers from slipping through the mesh holes. Once the meshes are stacked, approximately 500 fibers at a time can be dropped into the container holding the meshes, and with slight tapping, the fibers will flow through the set in seconds. For our recent prototypes, a trained student could form a fiber matrix for a 2x2 tower production block with 3,120 fibers in around 30 minutes.

The total production volume of scintillating fibers for the forward EMCal (fEMCal) is 3,000 km.

Only two companies, KURARAY and Luxium (formerly St. Gobain, BICRON), are capable of producing the necessary fibers. Both companies' fibers were previously used to construct and beam-test several WScFI EMCal prototypes for the EIC, with St. Gobain fibers also utilized by the sPHENIX collaboration for their barrel EMCal. Recently, Luxium optimized the composition of their standard BCF-12 fibers specifically for the shorter 17 cm fibers required for fEMCal, resulting in a 20% improvement in light yield compared to their standard fibers. This was achieved by adjusting the concentrations of primary and wavelength-shifting fluors, bringing them to the same performance level as KURARAY fibers. Table 8.3 outlines the technical specifications and requirements for the fEMCal fibers.

Table 8.9: Requirements and Technical specifications for fEMCal scintillating fibers.

Parameter	Requirements	Comments
Light Yield (LY)	$\geq$ 8000 photons per MeV	Acceptance QA with Sr90 source
		Compared to a standard sample
Nominal Diameter	0.47 mm $\pm$ 0.0094 mm RMS $\leq$ 0.02 mm	QA sampled on 10% boxes
		100% at ramp-up prod. stage
Attenuation Length	$\geq$ 3 m	QA with UV LED
Batch-to-batch LY variation	$\leq$ 10%	QA with Sr90
Emission spectrum	Blue-green light	To match QE of SiPMs
Scintillation Decay Time	$\leq$ 3 ns	Bunch structure at EIC
Delivery Method	In cans, length of fibers +2%, -0%	Length $\geq$ 1 m, increment 20 cm

To create a scintillating fiber matrix, it is essential that the fibers remain straight when placed into the mesh framework. Fibers processed from spools tend to retain a bend due to "memory," which leads to significant friction between fibers flowing through a set of meshes, which complicates the assembly process. Among suppliers, only Luxium agreed to a delivery method that addresses this issue, making them the sole provider of fibers for the fEMCal. These scintillating fibers are a long lead procurement item, with a pre-production batch expected to arrive at ePIC by the end of 2024, followed by monthly deliveries of the remaining fibers. Both the production and acceptance sites will adhere to agreed-upon QA and acceptance protocols to ensure that the fibers meet fEMCal specifications. Some of these QA steps are outlined in Table 8.3.

The concept of using tungsten powder as an absorber was briefly explored by the UCLA group in 2003, when they constructed and tested a small electromagnetic prototype at SLAC. At the time, the tower structure required a thin-walled brass container to hold the dry powder and fibers in place. However, this assembly technique proved imperfect, leading to significant transverse non-uniformities in detector response due to variations in the sampling fraction and potential displacement of fibers during packing. A compact calorimeter demands strict mechanical tolerances and a highly uniform internal structure to achieve theoretical energy resolution. To address these issues, we introduced intermediate meshes to secure fibers along the towers and developed a vacuum-assisted method to infuse epoxy into the tungsten powder/fiber assembly. Once assembled, the structure becomes rigid, eliminating the need for external containers and dead material in the tower. The homogeneity of the WScFi structure was verified by cutting multiple samples on small pieces which were analyzed and was found to exceed 1%. The mechanical properties of the WScFi structure were measured and they are comparable to construction steel.

This refined technique, with slight variations, was then employed in constructing the sPHENIX barrel EMCal and all recent fEMCal R&D prototypes.

Light Collection scheme and Photosensors The light collection scheme and photosensor setup adhere to the general requirements outlined in Table 8.2. The back of each installation block features a thin layer of optical epoxy (1.8 mm thick) mixed with 10% TiO_2, which acts as a diffuse optical reflector for the scintillating fibers and provides a surface for bonding the 13 mm-thick aluminum "strong back." This strong back plate is then bolted to the steel interface plate connecting the EMCal and HCal. On the front side of the installation block, a 21 mm-long light guide (LG) plate is attached. Made from a single piece of optically clear cast acrylic, this LG plate has 64 trapezoidal light guides to direct light from the fibers to the SiPMs. The front and back views of the LG plate with SiPMs attached can be seen in Fig. 8.8. The light collection efficiency of this setup is approximately 80%, which is sufficient to detect 15 MeV in a single tower, corresponding to 24 fired pixels. However, due to the short length of the light guide (typically much longer in fiber calorimeters), light "mixing" from individual fibers is minimal, resulting in spatial non-uniformities in light collection at the 10% level, as measured with a point light source.

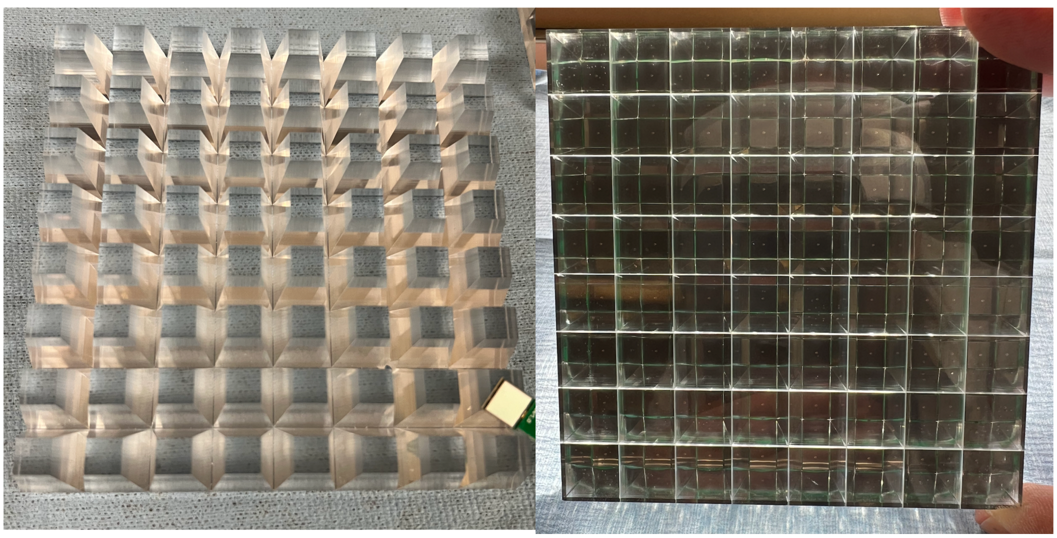

Figure 8.35: Front and back wievs of LG plates with installed SiPMs.

The chosen photodetector for the fEMCal is the SiPM (Silicon Photomultiplier). Over the past 15 years, extensive R&D programs across the globe—including the generic detector R&D program for the EIC—have worked to bring SiPM technology to a mature and reliable level. Today, hundreds of thousands of SiPMs are in use in various high-energy physics and nuclear physics experiments. These detectors are extremely compact, robust, and well-suited for calorimetry readout in moderate radiation environments, such as the forward region of the ePIC detector, as shown in Table 8.2. The failure rates of SiPMs in calorimeter operations at facilities like JLab, BNL, and CERN have been remarkably low, typically less than 0.1%. Notably, the STAR Forward Calorimeter System (FCS) experienced zero SiPM failures during three years of operation under conditions similar to those expected in the high-luminosity EIC. Although neutron-induced damage will lead to increased leakage current and noise levels, these effects remain within tolerable limits. For example, it is anticipated that the equivalent noise level for fEMCal at ePIC will rise to around 6 MeV after 10 years of operation, particularly in areas near the beam pipe. This projection is based on scaling from the results observed in the STAR FCS. After this period, replacement of some of the SiPM boards near the beam pipe may be necessary. These considerations informed the design of the fEMCal readout system, ensuring a straightforward integration with the detector. The technical specifications and performance details of the SiPMs for the fEMCal are summarized in Table 8.4.

Table 8.10: Requirements and Technical specifications for fEMCal SiPMs.

Parameter	Requirements	Comments
Active Area	6 mm $\times$ 6 mm	Efficiency of light collection, E_{min}15 MeV
Pixel Size	15 or 20 um	Dynamic Range, E_{max}100 GeV
Peak Sensitivity	$\sim$ 420 nm	Match scintillating fibers spectra.
PDE	$\geq$ 30%	Efficiency of light collection, S/N
Gain	$\sim 2\times10^5$	at 3 V overvoltage, S/N
DCR	$\leq$ 3000 kcps	at 3 V overvoltage, 25 C, S/N
Temperature Coefficient	$\leq$ 40 mV/C	Stability, Unifformity
Direct Cross Talk	$\leq$ 1%	Radiation, dark current
Terminal Capacitance	$\leq$ 2 nF	FEE coupling
Packing Granularity	Multiple of 4 per tray	4 SiPMs per tower at same V_{op}
V_{op} variation within a tray	$\pm$ 0.02 V	Uniformity of response

Mechanical Integration The mechanical integration, installation procedures, and structural tests for the fEMCal were validated using installation blocks at BNL. These blocks were produced following the final production protocols and using the same components that will be used for the actual installation. Structural tests on smaller samples demonstrated that the safety factor for the proposed mounting scheme is greater than 48. A full structural test (Fig. 8.9) was conducted by mounting an installation block on a mockup plate and applying five times the expected load. The deflections at the readout end of the fEMCal block were measured to be less than 100 um, confirming that each installation block is self-supporting and does not exert any load on the blocks beneath it. Simple installation fixtures were designed, and the installation procedures were verified to ensure safety. Specifically, it was crucial to confirm that the fEMCal blocks could be safely installed with the SiPM-carrying boards glued to the LG plates. The tests confirmed that the blocks can be safely mounted onto the hadron end-cap without causing any damage to the SiPM boards.

Performance The performance of the fEMCal prototypes has been tested in several test beams at FNAL over the past few years, initially as part of the generic detector R&D for the EIC and later as part of the ePIC R&D program. In the summer of 2024, one installation block featuring the latest version of the light guide (LG) and SiPM readout was tested at FNAL. Energy scans were conducted at various impact angles covering the entire fEMCal acceptance range. As expected, some variation in response across the surface was observed, as shown in Fig. 8.10, due to the compact nature of the LG. However, this variation represents an improvement compared to earlier versions [26]. Position-dependent corrections, based solely on the data from fEMCal, were applied to account for non-uniformities. This method is similar to the approach used in the 2014 test [26] and for the sPHENIX barrel EMCal. As anticipated, the uniformity of response improves with shallower impact angles. The energy resolution, shown in Fig. 8.10, corroborates previous measurements with this type of electromagnetic calorimeter [26] and aligns with the performance requirements outlined in Table 8.2. The measured absolute light yield is 1580 pixels/GeV.

The remaining performance parameters were extensively tested using MC simulations, incorporating the full ePIC simulation chain with the latest detector geometry updates. A material scan indicated the presence of approximately 0.2 X_0 of "dead" material in front of the fEMCal in ePIC, but its impact on performance was found to be negligibly small. Simulations conducted with PYTHIA8,

Figure 8.36: Structural and installation tests at BNL.

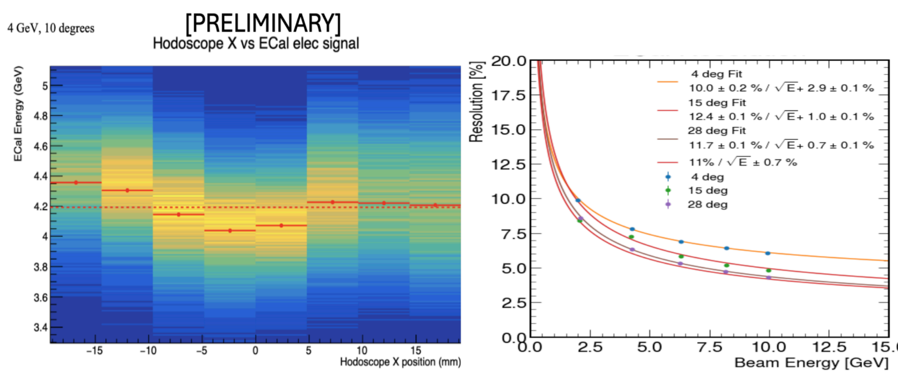

Figure 8.37: Response of calorimeter vs position in hodoscope (left panel). Energy resolution for different impact angles (right panel).

using minimal Q^2 cuts for all energy configurations at the EIC, examined occupancy, rates, and dynamic range. These studies informed the set of requirements listed in Table 8.2.

An initial investigation into γ/π^0 separation, based on the traditional shower shape analysis method outlined in the EIC Yellow Report (Fig. 11.46, [2]), revealed potential for improvement. A significant enhancement in γ/π^0 separation was achieved by applying machine learning algorithms. As shown in Fig. 8.11 (left panel), the misidentification rate at 60 GeV dropped to approximately 10%, compared to 80% with traditional methods [2].

Readout Electronics The fEMCal readout electronics face three primary challenges: achieving a large dynamic range of 7000:1, ensuring precise discrimination for streaming small signals (24 pixels) amidst dark counts of up to 45 GHz caused by radiation damage to SiPMs, and integrating everything within a compact space—around 5 cm for SiPM boards, front-end boards (FEBs),

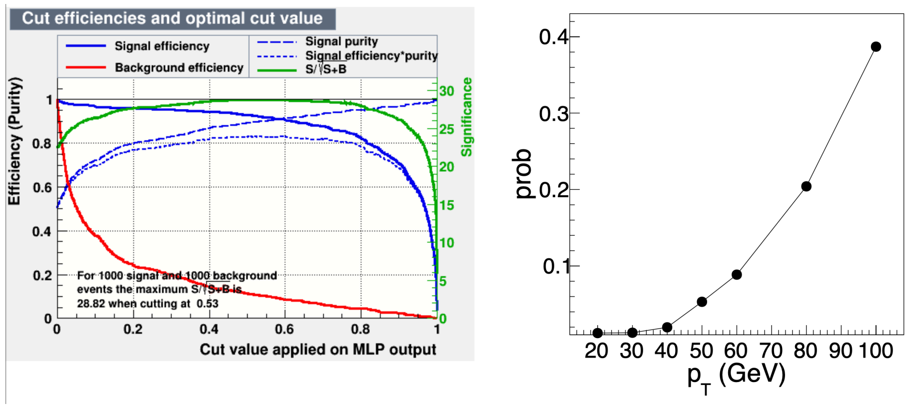

Figure 8.38: Signal (single photon) efficiency and background (merged di-photons) contamination for different cut value of the NN output for 60 GeV (left panel). Probability of misidentifying π^0 as a single photon vs energy (right panel)

cooling, and cables. Table 8.7 summarizes requirements for the FEB.

Table 8.11: Requirements for the FEB

Parameter	Requirements	Comments
SiPM & overvoltage	4xS14160-6015PS, 2-3V	
Min signal	15 MeV (@ 1.6 pix/MeV)	
Max signal	100 GeV	
Hit rate	10 kHz	per channel
Charge reso.	$\sim$210%/$\sqrt{npix}$ $\oplus$ (0.9)%	contribute 10% of fEMCal resolution
Charge nonlinearity	$\leq$ 1%	
Time resolution	$\ll$ 10 ns	for $\geq$100 MeV signals only
SiPM bias voltage stability	$\leq$ 10 mV	including T compensation
Bias voltage setting range	33 to 47 V	sufficient for meaningful IV curve
Bias current range & mon. resolution	2 mA, 200 nA	4 SiPMs per tower at same V_{op}
LED drive control	var. amplitude, masks	fired by global command

Building on the successful design of the STAR FCS readout, fEMCal's readout system transfers SiPM signals to a low impedance load, shapes and amplifies the resulting voltage, and digitizes the waveform. Hits are detected in the digital waveform via threshold crossing (which may be filtered). In streaming readout mode, regions of interest in the digital waveform are identified, timestamped, and sent to an output FIFO/merging scheme, before being transmitted to the readout (RDO) board. At the RDO, data from up to 16 FEBs are buffered, merged, and sent to the DAM. Feature extraction, converting raw waveform samples to estimated pulse amplitude and timing, may be done either at the FEB or RDO level to reduce data volume. If hardware feature extraction is not used, this will be performed during preliminary online analysis.

Waveform digitization for fEMCal will operate at either 39.4 MSPS or 49.25 MSPS. The digitization clock must be phase-locked to the beam bunch crossing clock at 98.5 MSPS to extract hit timestamps in real-time within the streaming DAQ system. Sampling at 98.5 MSPS is not feasible due to power and FPGA resource constraints. To meet the 15 MeV readout threshold and achieve the dynamic range, the ADC resolution must be 14 bits. The analog waveform will be shaped before digitization

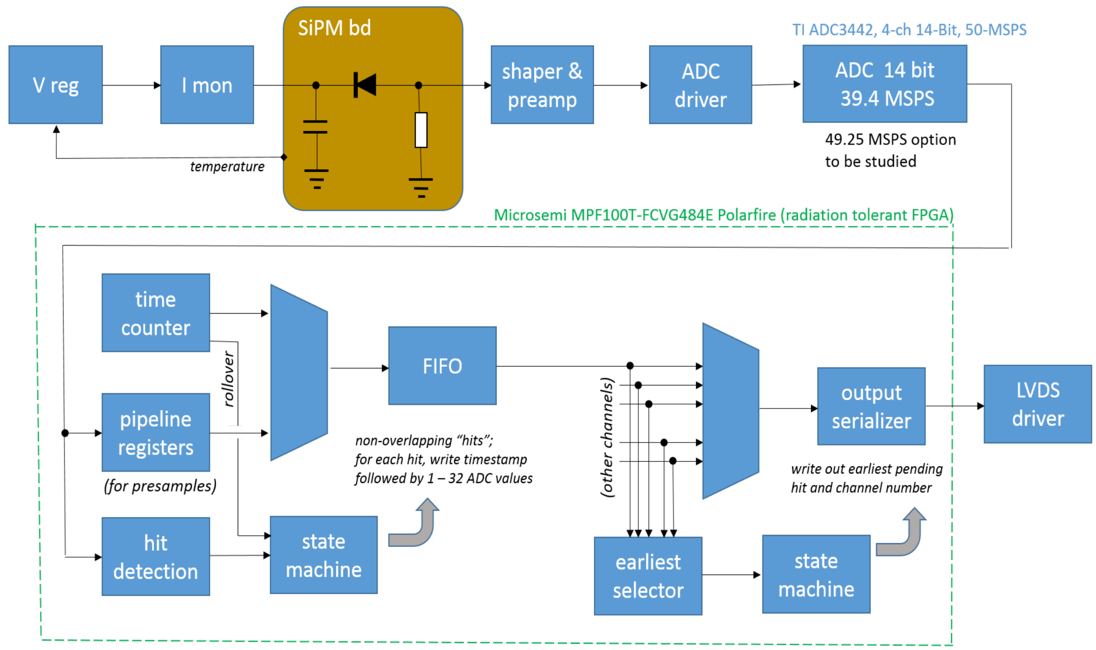

Figure 8.39: fEMCal front end electronics.

to achieve a peaking time of approximately 2.8/f_SAMPLE, which ensures less than 1% error in pulse amplitude measurement while minimizing noise from dark count pileups. For instance, a 57 ns peaking time is optimal at 49.25 MSPS.

The FEB will individually regulate bias voltage for each tower, providing temperature compensation for each SiPM board (covering 2 × 2 towers) and monitoring current with built-in protective current limits. Each tower's four SiPMs will be connected in parallel, sharing a common bias voltage, requiring precise matching of the breakdown voltages (V_BR) among the four SiPMs to ensure uniform gain. The bias regulation circuits, developed from the STAR Forward Calorimeter, have proven effective, though radiation sensitivity in a voltage reference IC was noted. To mitigate this, fEMCal's bias regulator will use a remote reference on the power distribution boards, ensuring the required 0.03% stability. Less critical internal voltage references require only 1% stability. The bias regulation channels provide sharp current limiting to protect the SiPMs from overload, maintaining 10 mV bias voltage stability up to the current limit (2 mA).

Signal routing from the SiPM boards to the FEBs is achieved through board-to-board connectors, eliminating the need for cables. These connectors can accommodate mechanical tolerances of +/- 0.5 mm between the FEB and SiPM boards and overlap with space allocated for the cooling water tube. Should radiation damage impact the innermost FEBs, a backup plan would route SiPM signals via 2m coaxial cable bundles to FEBs mounted at the block periphery.

Connections between the FEBs and RDO will use shielded Cat6 Ethernet cables, routed horizontally through the FEB rows and out of the magnet to racks housing the RDOs. One rack will be placed north of the north detector half, and another south of the south detector half. Cable lengths are estimated at 15 meters, and it has been confirmed that LVDS signals can be properly received at 200 Mb/s over this distance, meeting performance requirements.

Each rack will also house a Wiener MPOD crate with low-voltage (LV) power supplies, with one crate serving the north half and one for the south half of the detector. Each FEB will require approximately 250 mA at +16 V, 180 mA at -2 V, and up to 67 mA (depending on SiPM radiation damage) at +50 V.

The FEBs will be cooled conductively via a copper bracket attached to the main board (housing the ADCs, FPGA, and power supply circuits) and connected to a water cooling line. The water line will consist of standard ¼ inch (potentially 3/16 inch) diameter copper tubing. A negative pressure system will mitigate the risk of water leaks. Two rows of FEBs will be served by a single water line in a U-shaped loop, with no fittings at each FEB, only at the loop ends. Reliable flare fittings will be used for the connections. Custom water manifolds, located in the "service gap" at the outer perimeter of the calorimeter blocks, will manage water distribution. The arrangement will likely consist of two supply and return manifold sets—one for the upper and one for the lower half of the detector.

Each water circuit will need to cool about 750 W of power from 148 FEBs, requiring chillers with at least 1.5 kW capacity for each half of the detector. One chiller will serve the north half and another the south, cooling two water circuits each.

Slow controls for fEMCal will fall into two categories: hardware registers on the FEBs (communicated through DAQ software and the DAM/RDO) and controls for commercial equipment such as the water chillers and power supplies (Wiener MPOD), connected via Ethernet. SoftIOC interfaces will manage EPICS variables, providing GUI control, logging, and alarms.

Table 8.8 summarizes the control and status registers for the FEB.

Table 8.12: Control and status registers on the FEB

Function/description	Qty per FEB	R/W	Notes
SiPM bias voltage (base)	32	R/W	
Bias temp. comp. slope	1	R/W	
actual compensation	8	R	i.e. temperature
SiPM current monitor	32	R	extra diagnostic info
input LV supply monitor	2	2	
FEB temperature monitor	3	R	
FEB & SiPM board serial numbers	9	R	read once at startup
firmware revision	1	R	read once at startup
firmware update interface	1	R/W	maintenance use only
hit threshold channel mask	32	R/W	
hit detection options registers	4	R/W	
LED firing mask	1	R/W	
hit scalers	32	R	
fifo overrun scalers	32	R	
ADC configuration interface	1	R/W	might be internal use only

Calibration The fEMCal faces the hadron beam, and at mid to high energies, its signals will predominantly come from photons produced by π^0 decays. Tower-by-tower absolute energy calibration of the forward electromagnetic calorimeter will be performed by reconstructing π^0 mesons through the invariant mass of two photons from π^0 decays. It is expected that π^0 calibration for each tower can be achieved in approximately one day of data collection, followed by semi-online analysis using only forward fEMCal data. The method involves associating reconstructed

π^0 mesons with the tower showing the highest response, adjusting the tower's gain based on the π^0 mass location, and repeating the process over several iterations. This technique has been successfully implemented in forward calorimeters at RHIC, including the STAR FCS.

Electrons from DIS events, combined with tracking information, can be used to cross-check the calibration. However, this approach requires a large dataset and will be performed offline. Additionally, Minimum Ionizing Particle (MIP) signals from hadrons can be utilized for calibration at the low-energy end. For high energies, where the two photons from π^0 decays are too close together for the forward EMCal to distinguish them, η mesons can be used to verify energy non-linearity.

Monitoring system An LED system will be installed on the FEE boards to illuminate four towers using a trigger pulse. The LEDs will be preselected to provide equal light output to the towers, serving as a critical monitoring system. This will be essential for initial testing during installation, verifying mapping, and ensuring long-term stability of the detector, SiPMs, and FEE board gain, as well as detecting any potential radiation damage. A dedicated short LED run will be performed daily to monitor the calorimeter's performance.

Additionally, the current and voltage on the FEE boards will be continuously monitored. Periodic I-V curve measurements will be conducted, on a weekly or bi-weekly basis, to assess the health of the SiPMs and FEE boards.

Status and remaining design effort:

R&D effort: eRD106 will be completed in early 2025 with finalizing analysis of the test beam data.

E&D effort: Detailing of mechanical design, and formalizing production drawings.

Other activity needed for the design completion: Produce and test first versions of final design FEB and SiPM boards.

Status of maturity of the subsystem: $\sim 70\%$

8.3.6 Hadronic Calorimetry

Add text here.

8.3.6.1 The backward endcap hadronic calorimeter

Requirements

Requirements from physics: Add text here.

Requirements from Radiation Hardness: Add text here.

Requirements from Data Rates: Add text here.

Justification

Device concept and technological choice: Add text here.

Subsystem description:

General device description: Add text here.

Sensors: Add text here.

FEE: Add text here.

Other components: Add text here.

Performance

Implementation

Services: Add text here.

Subsystem mechanics and integration: Add text here.

Calibration, alignment and monitoring: Add text here.

Status and remaining design effort:

R&D effort: Add text here.

E&D status and outlook: Add text here.

Other activity needed for the design completion: Add text here.

Status of maturity of the subsystem: Add text here.

Environmental, Safety and Health (ES&H) aspects and Quality Assessment (QA planning: Add text here.

Construction and assembly planning: Add text here.

Collaborators and their role, resources and workforce: Add text here.

Risks and mitigation strategy: Add text here.

Additional Material Add text here.

8.3.6.2 The barrel hadronic calorimeter

Requirements

Requirements from physics: Add text here.

Requirements from Radiation Hardness: Add text here.

Requirements from Data Rates: Add text here.

Justification

Device concept and technological choice: Add text here.

Subsystem description:

General device description: Add text here.

Sensors: Add text here.

FEE: Add text here.

Other components: Add text here.

Performance

Implementation

Services: Add text here.

Subsystem mechanics and integration: Add text here.

Calibration, alignment and monitoring: Add text here.

Status and remaining design effort:

R&D effort: Add text here.

E&D status and outlook: Add text here.

Other activity needed for the design completion: Add text here.

Status of maturity of the subsystem: Add text here.

Environmental, Safety and Health (ES&H) aspects and Quality Assessment (QA planning: Add text here.

Construction and assembly planning: Add text here.

Collaborators and their role, resources and workforce: Add text here.

Risks and mitigation strategy: Add text here.

Additional Material Add text here.

8.3.6.3 The forward endcap hadronic calorimeter

Requirements

Requirements from physics:

Requirements from Radiation Hardness:

Requirements from Data Rates:

Justification

Device concept and technological choice:

Subsystem description:

General device description:

Sensors:

FEE:

Other components:

Performance

Implementation

Services:

Subsystem mechanics and integration:

Calibration, alignment and monitoring:

Status and remaining design effort:

R&D effort: Add text here.

E&D status and outlook: Add text here.

Other activity needed for the design completion: Add text here.

Status of maturity of the subsystem: Add text here.

Environmental, Safety and Health (ES&H) aspects and Quality Assessment (QA planning:

Construction and assembly planning:

Collaborators and their role, resources and workforce:

Risks and mitigation strategy:

Additional Material Add text here.

8.3.7 Far forward detectors

The ePID far-forward detectors are required to enable essentially the entirety of the exclusive physics program at the EIC, where final-states involve protons, neutrons, and various other particles at $\eta > 4.5$. There are four subsystems, all integrated with the outgoing hadron beamline between $\sim$5.5 and 39 meters from the interaction point. The far-forward subsystems are summarized in Fig. 8.40, and details are presented in subsequent subsections.

8.3.7.1 The detectors in the B0 bending magnet

Requirements

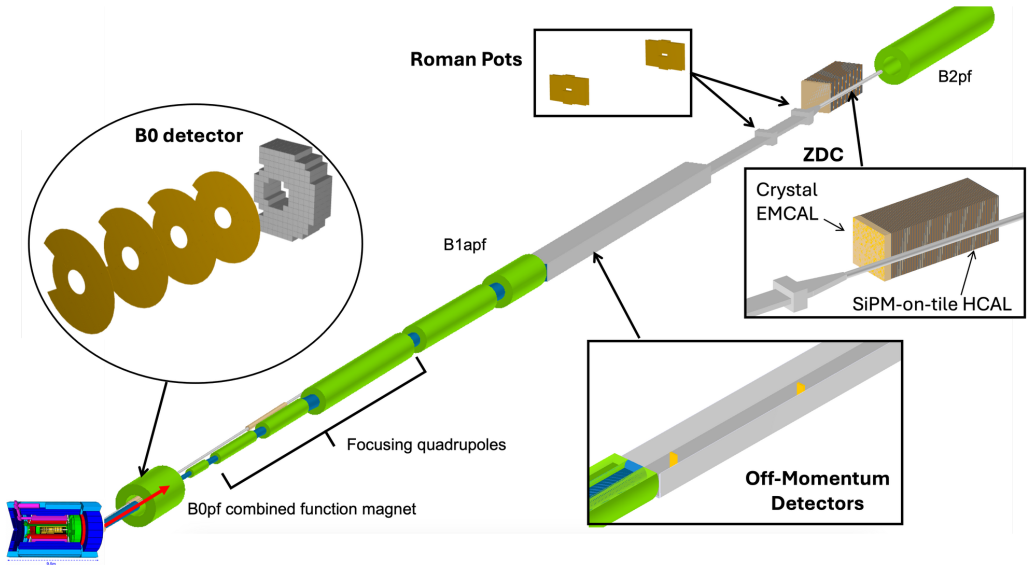

Figure 8.40: All four far-forward subsystems in the outgoing hadron beam direction. The green cylinders are accelerator dipole and quadrupole magnets.

Requirements from physics: The B0 magnet bore will contain two detectors: a charged particle tracker and an electromagnetic calorimeter. Both will have acceptance covering the angular region from 5.5 to 20 mrad. Given the mechanical constraints imposed by the detectors' location in the magnet (and respecting the beam lines themselves) the detectors will be highly asymmetric for angles greater than $\sim$13 mrad. To maximize acceptance it's required that there be minimal dead areas in the instrumentation especially for angles less than $\sim$13 mrad. The tracker should have momentum resolution up to 6% for protons, and timing precision sufficient to deal with vertex smearing. The calorimeter should be sensitive to both soft, O(100 MeV), and hard, O(100 GeV), photons. The energy resolution should be less than $8\%/\sqrt{E} \oplus 4\%$. We note that for some analysis use cases the calorimeter will function as a photon 'tagger' rather than an actual calorimeter, and so in some regions of acceptance (where the mechanical constraints are acute) this resolution may not be achieved but having the acceptance instrumented is still valuable.

Requirements from Radiation Hardness: The expected non-ionizing radiation dose at a longitudinal distance of 692 cm from the interaction point (near the fourth tracking layer and the front of the calorimeter) is approximately 3.1×10^{11}) 1 MeV neutron equivalent per square centimeter for 100 fb^{-1}. At this location the ionizing dose can reach O(100) kRad.

Requirements from Data Rates: Add text here.

Justification

Device concept and technological choice: The charged particle tracker will be composed of four layers instrumented with silicon. The layers are approximately equidistantly placed at distances between 590 and 690 cm from the interaction point, which given the field inside the magnet allows satisfactory proton measurement and momentum reconstruction. The electromagnetic calorimeter is composed of 135 scintillating $PbWO_4$ crystals, each one 2 x 2 x 20 cm^3 (the long direction is on the z axis). We note that the crystals are the same as those used in the EEEMCal.

Subsystem description:

General device description: Each tracking layer has a transverse layout to cover as much of the angular acceptance as possible given the mechanical constraints, as illustrated in Figure **??**. The crystals of the calorimeter are arranged in a similar way for the same reason.

Sensors: For the tracking detectors AC-coupled low-gain avalanche diodes (AC-LGADs) are chosen due to their capability to provide both high-precision space and time information. In order for the spatial resolution to meet the performance requirements charge sharing must be implemented in the reconstruction. We note that this technology is broadly in use within ePIC, and its particular implementation for the B0 detectors should be very similar to the Roman Pots/Off Momentum Detectors. For the calorimeter the $PbWO_4$ crystals produce light peaking at $\sim$ 420 nm, which will be read out by SiPM. Four 6x6 mm^2 SiPM will be used per crystal, 3 with 15 micron pitch and one with a 10 micron pitch (likely Hamamatsu S14160-6015PS and S14160-6010PS, respectively). The larger pitch SiPM have fewer pixels but higher efficiency making them appropriate for smaller signals, whereas the smaller pitch SiPM will be utilized for the higher energy particle signals.

FEE: Following the Roman Pots/Off Momentum Detectors, the ASICs will be readout using LPGBT in-place of FPGAs due to the high-radiation environment in which these detector will be located. AC-LGAD + ASIC modules will be connected to the LPGBT, which will be coupled to a VTRX+ to convert the signals to a fiber to send off to the DAW system. The electronics to process the SiPM signal are still to be worked out but expected to follow closely the scheme of the EEEMCal.

Other components: Add text here.

Performance The key physics task of the B0 tracker system is the measurement of protons, and this is summarized by the acceptance and transverse momentum resolution shown in Figure 8.41. The B0 calorimeter's acceptance for photons is shown in Figure 8.42. The calorimeter seeks to measure photons over a very large range. The performance of the detector, in particular the energy resolution, is shown separately for low and high energy photons in Figure 8.43. The higher energy photons are evaluated based on a signal to a single 10 micron pitch SiPM, whereas the lower energy photon performance assumes three 15 micron pitch SiPM per crystal.

Implementation

Services: For the trackers low voltage ($\sim$3V) and high voltage ($\sim$150V) supplies for the operation of the ASICs and the bias supply, as well as slow controls for the voltages and the DAQ system. The SiPM for the calorimeter need a bias of ($\sim$5V) .The cooling system is still to be worked out, but is expected to be air based (unlike the in-vacuum challenge of the similar instrumentation for the Roman Pot/Off Momentum Detectors).

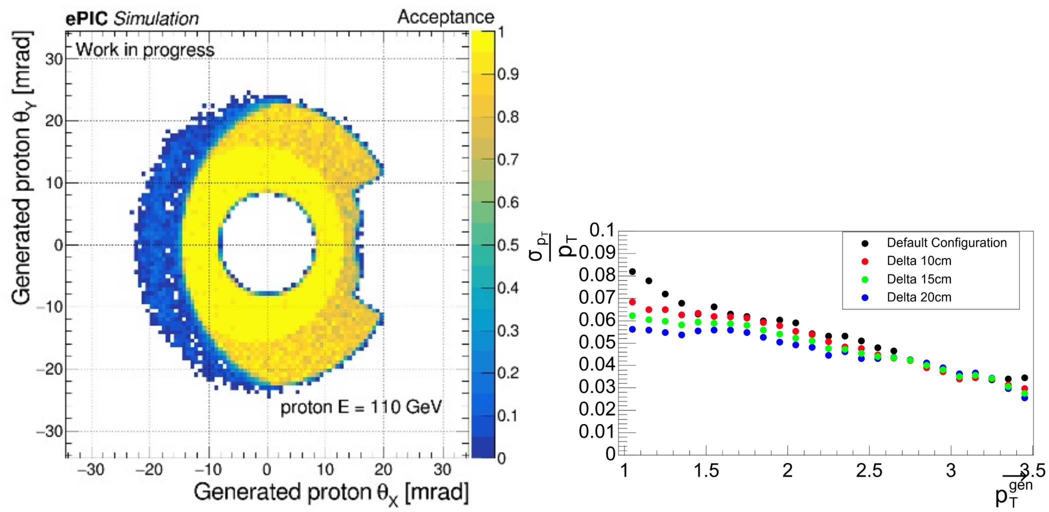

Figure 8.41: Left: The B0 tracker's acceptance of protons (E=110 GeV), as a function of θ_x and θ_y. PLACEHOLDER NEEDS TO BE REMADE W/REAL B FIELD Right: The p_T resolution for protons reconstructed in the B0 tracker. PLACEHOLDER NEEDS TO BE REMADE WITH FINAL LOCATIONS, FINAL TRACKING, PROPER LABELLING ETC

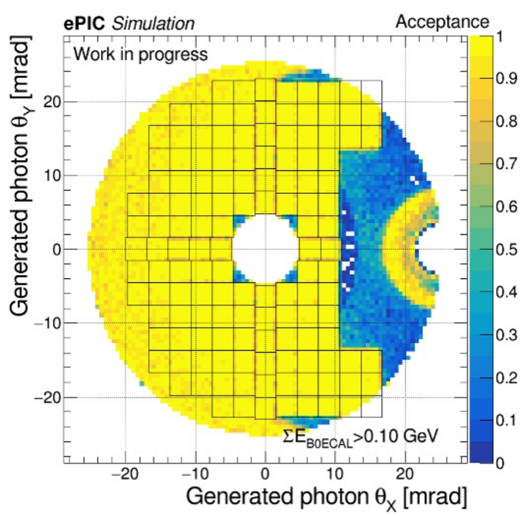

Figure 8.42: The B0 EM calorimeter's acceptance of photons defined as an energy deposit above 100 MeV in a calorimeter crystal.

PLACEHOLDER - SPLIT HARD SOFT, FIX CRYSTAL ALIGNMENT

Subsystem mechanics and integration: The integration of the detectors into the B0 magnet bore is a significant undertaking. The space for the detectors (and services) is quite limited and the installation procedure introduces more constraints. After the vacuum valve is closed there is only about 10 cm of clearance in front of the magnet and this precludes installation of the 20 cm crystals. To address this difficulty, the crystals will be installed prior to closing the valve closing and the beam commissioning. At this point *only* the crystals will be installed to avoid the risk of damaging the other components during the commissioning. Following this the SiPM and electronics of the calorimeter will be installed. Both installations as well as the final positioning of the detectors will

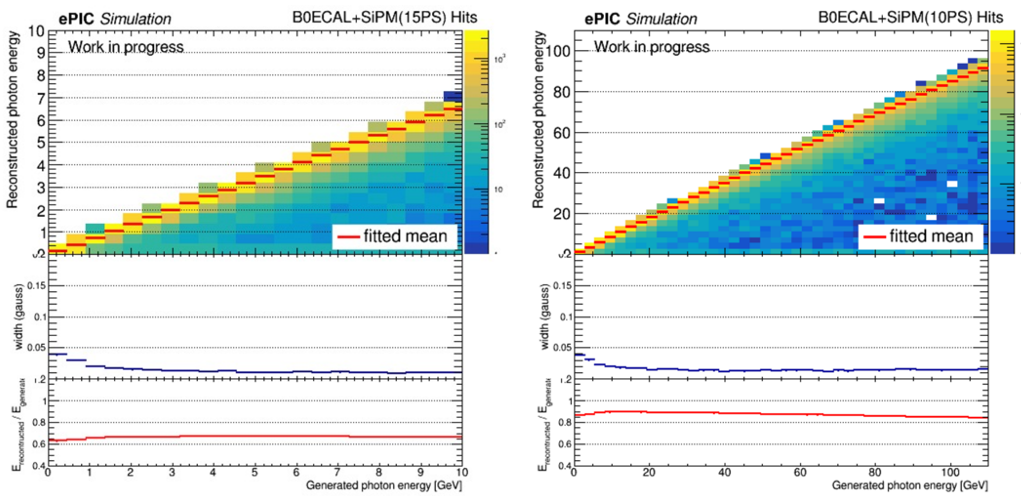

Figure 8.43: The energy reconstructed and associated resolution for the B0 EM calorimeter of photons with $\theta < 13$ mrad in the soft (left) and hard (right) energy reconstruction regimes. PLACEHOLDER - zoom soft photon, update reflectivity

be via a rail system: detector components will be loaded onto the rails system outside the magnet and inserted in to it. We note that the detectors will be installed as sub-detectors not as monolithic pieces covering the entire acceptance.

Calibration, alignment and monitoring: Add text here.

Status and remaining design effort:

R&D effort: There is still work to be done for full detector operation. For the trackers especially demonstrating effective reconstruction using charge sharing and for the calorimeter the multi-SiPM readout. For both the trackers and calorimeter this includes optimizing the acceptance in concert with the installation procedure.

E&D status and outlook: Add text here.

Other activity needed for the design completion: Completion of the mechanical rail system is underway and this includes a final scheme of subdividing the detectors into sub-detectors accordingly.

Status of maturity of the subsystem: Add text here.

Environmental, Safety and Health (ES&H) aspects and Quality Assessment (QA planning: Add text here.

Construction and assembly planning: The tracking system should benefit from the BNL local expertise and production capabilities for AC-LGAD and from there 'directly' to installation readiness. The calorimeter sub-components may be prepared either on or off site, but in any case the final assembly can not be separated from the installation procedure.

Collaborators and their role, resources and workforce: The Israeli ePIC consortium (in particular BGU and TAU) are playing the main role in the detector development and this will continue through installation/operation. There is also very significant participation from BNL generally, and especially for the common AC-LGAD instrumentation.

Risks and mitigation strategy: For the trackers the largest risk is the necessity to utilize charge sharing in the reconstruction to obtain the needed momentum resolution. Other detection technologies have been considered to mitigate this risk (with smaller pixels) but to this point none has been identified as an appropriate alternative. For both detectors (and even more acutely for the calorimeter) the installation challenge risks limiting the detector acceptance.

Additional Material Add text here.

8.3.7.2 The roman pots and the off-momentum detectors

Requirements

Requirements from physics: Measurement of protons at various rigidities, with rigidity defined by ratio of the proton momentum to that of the beam itself, and with scattering at angles < 5mrad requires detectors integrated directly into the hadron beamline in the form of Roman pots (RP). The Off-Momentum detectors (OMD) enable tagging and reconstruction of spectator protons from the breakup of light nuclei (e.g. deuterons and He-3), which produce protons at rigidities $< 65\%$, with deuterons producing protons at an average of $\sim 50\%$ rigidity. For the Roman pots, achieving acceptance down to 0 mrad is impossible due to the presence of the hadron beam itself, so the low-θ (low-p_T) acceptance is essentially entirely driven by the focusing quadrupoles (machine optics) before and after the interaction point. For IP-6, the choice of low-β^* optics to maximize luminosity (so-called "high divergence") means the transverse beam size, $\sigma_{x,y} \approx \sqrt{\beta_{x,y}(z_{RP}) \times \epsilon_{x,y}}$, where $\beta_{x,y}(z_{RP})$ are the beta-functions in (x,y) at the Roman pots location and $\epsilon_{x,y}$ is the emittance for the machine, is larger, worsening the acceptance at the expense of luminosity. Generally, $10\sigma_{x,y}$ is the average "safe distance" for the Roman pots to operate. Conversely, a choice can be made to reduce luminosity to improve low-θ acceptance at the Roman pots location, normally referred to as "high acceptance" optics. Given this set of operational parameters for the machine itself, it is required that the sensor packages have minimal dead area at the edges to take maximum advantage of the machine optics during data taking runs.

For resolution, the detectors must deliver p_T-resolution better than 10%.

Requirements from Radiation Hardness: Maximal radiation doses are shown to be ¡ 10^{12} 1 MeV neutron equivalent for NIEL radiation, while ionizing doses are around 1 krad for the Roman pots region of ePIC [will add plot here, or reference section on the radiation].

Requirements from Data Rates: Rates during normal operations, with expected vacuum of 10^{-9} mbar, are a few Hz/channel. However, the beam halo could potentially provide rates of 30-50kHz at $\sim 10\sigma$ from experience of Roman pots at STAR. While the EIC hadron beam will have many differences to the RHIC hadron beam, it's hard to estimate the full rate impact of the beam halo without an appropriate simulation. This is something to be done in the coming year as the machine develops.

Justification

Device concept and technological choice: The basic concept of Roman pots detectors for measuring protons near the beam is not new and has been employed at HERA, RHIC, and the LHC, among other collider facilities. In the case of the EIC, the Roman pots (and OMD) need to be able to make measurements with challenges different to those in previous facilities. Studies from the EIC generic R&D program, in particular eRD24, demonstrated that the RP detectors need to have both high spatial ($\sim 140\mu$m) and timing ($\sim$35ps) resolutions, a challenge to deliver with one subsystem. As silicon detector technology has advanced, an evolved version of the DC-coupled Low Gain Avalanche Diode (DC-LGAD) sensor, normally used for high-resolution timing detectors Add reference here later, has come to the fore in the form of an AC-coupled version, known as the AC-LGAD. The AC-LGADs allow for pixilization and can meet the requirements of the RP and OMD subsystems, as was the goal of eRD24.

An additional challenge with operation of the RP and OMD systems is the operation of these detectors in vacuum. The subsystems themselves are large enough to prohibit use of the conventional "pot" vessels used to protect the detectors in other colliders, and therefor necessitate the inclusion of the sensor planes directly into the machine vacuum, providing unique challenges for cooling and shielding.

add figures of full detector layout here

Subsystem description:

General device description: The Roman pots and off-momentum detectors are both vacuum-based silicon sensors arranged into two stations for fully reconstructing protons at various magnetic rigidities, where rigidity here refers to the fraction of the momentum the proton has with respect to the steering dipoles design orbit momentum.

Sensors: AC-coupled low-gain avalanche diodes (AC-LGADs) are the technology of choice for these two subsystems due to their capability to provide both high-precision space and time information. add references here for testbeam results on SENSORS.

FEE: ASICs will be readout using LPGBT in-place of FPGAs due to the high-radiation environment in which these detector will be located. Up to sixteen AC-LGAD + ASIC modules will be connected to a single LPGBT, which will be coupled to a VTRX+ to convert the signals to a fiber to send off to the DAW system. The stave design is aimed to have the minimal amount of components inside the vacuum to ensure smooth operations and ease of access during maintanence periods.

Other components: Design of the front-end board and power distribution is still in a very early stage for the RP and OMD systems.

Performance The performance of the Roman pots and Off-Momentum Detectors is summarized in Fig. 8.44. The overall momentum resolution is also affected by the detailed understanding of the hadron magnet lattice, which is used to be able extract the normal transfer matrices used to reconstruct momenta in Roman pots detectors. There is also a software solution in place using

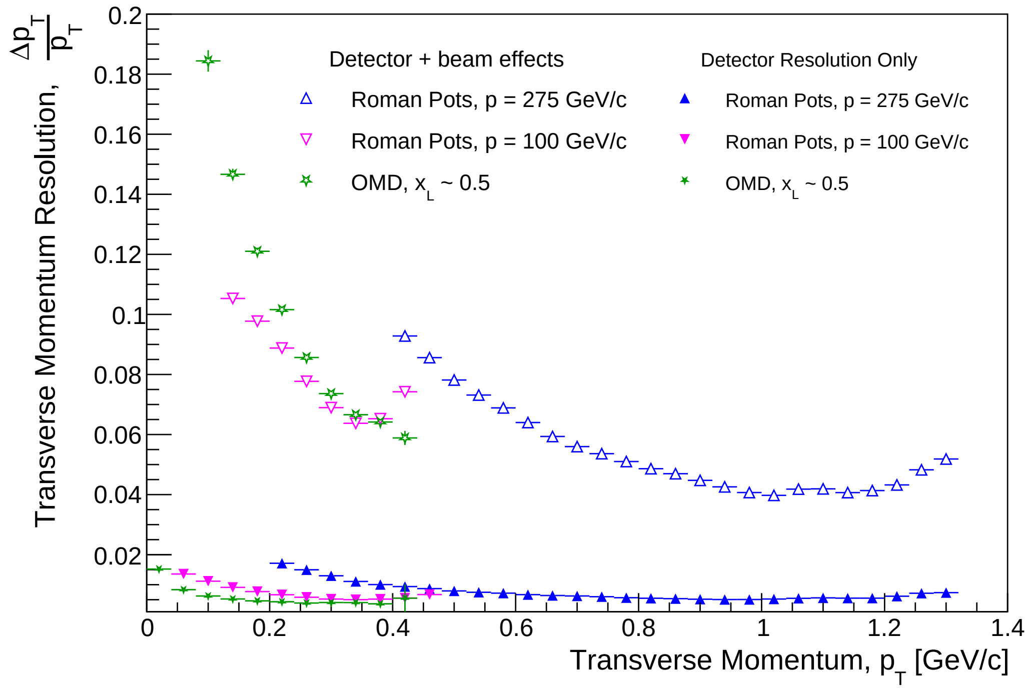

Figure 8.44: Summary of transverse momentum resolutions for the Roman pots and Off-Momentum Detectors. Contributions are separated by those induced by intrinsic detector choices (e.g. pixel sizes) and those from beam effects (e.g. angular divergence), which have an outsized impact on momentum measurements at very-forward rapidity. Will be replaced with DD4HEP version

deep neutral networks to further improve the momentum resolution performance, especially for the off-momentum detectors.

Implementation

Services: The Roman pots and OMD have the same essential needs for services, which include cooling using conductive strips coupled to an external chiller to allow cooling in-vacuum, low voltage (∼3V) and high voltage (∼150V) supplies for the operation of the ASICs and the HV bias supply for the sensor, and slow controls to control both voltages and the DAQ system, and also to control the moving stages necessary for the detector operations. There will also need to be communication between the slow controls and the machine for safety interlocks for faat beam abort systems, and for permits to enable motion control of the detectors when beam conditions are stabilized.

Subsystem mechanics and integration: The primary support systems only need to be able to support very light staves with 3-4 modules per PCB. However, the entire subsystem needs to be a on motor-driven rail system to enable movement near the hadron beam, especially in order to achieve acceptance at very-low $p_T \sim 0.2$ GeV/c.

Calibration, alignment and monitoring: AC-LGAD sensors will be calibrated with MIPs, while alignment of the detector systems will need to be carried out using beam-based alignment with dedicated, short very-low luminosity running, which enable the detectors to approach the beam much closer than the standard 10σ such that the beam halo itself can be seen on the sensor planes.

Status and remaining design effort:

R&D effort: Much work is still needed to demonstrate full system operations with full size sensors + ASICs, and the cooling concept using conductive strips. As of now, only 4x4 channel versions have been tested.

E&D status and outlook: Engineering design is still very preliminary, but necessary design choices are being evaluated as engineering support becomes available.

Other activity needed for the design completion: The design of the front-end PCB which carries the sensors, ASICs, and necessary services needs to be carried out. Presently, only a strawman concept which will meet our requirements exists.

Status of maturity of the subsystem: The design maturity of the system will be at $\sim 60\%$ by Q2 of FY25.

Environmental, Safety and Health (ES&H) aspects and Quality Assessment (QA) planning: Since these detectors are embedded directly into the machine vacuum, special considerations must be made for integration with the machine. We expect that the detectors will be interlocked against operation until permits are received from the machine, pending stable operations of the machine in terms of stable beam losses, collisions at the IP, and background conditions. The cooling system will also have to be integrated with the machine envelope and likely must pass an evaluation from the machine group.

Construction and assembly planning: Sensors and EICROC ASICs will be manufactured in different foundries, but bump-bonding of the sensors + ASICs can be done for the far-forward at BNL, since these detector subsystems are very small compared to other ePIC sub-systems. The assembly will have to take place in stages which include the following steps. First, preparation of stave printed circuit boards and quality assurance testing to ensure traces pass continuity tests to the Samtech connectors will have to be carried out. In parallel, diced sensors need to be tested to ensure they can maintain bias voltage safely, and other electrical tests. ASICs will undergo similar tests to ensure they are ready for bonding into full modules. Once sensors and ASICs are prepped, modules of 32x32 channel size (one sensor, one ASIC) will be bump-bonded. Once sensors are bump-bonded, QA will need to be performed on the final modules before they are integrated into stave PCBs.

Collaborators and their role, resources and workforce: BNL and JLAB will take the primary role in constructing the Roman pots and Off-Momentum Detectors, with engineering support for cooling possibly supplied by IJCLab in France.

Risks and mitigation strategy: The primary risks to the successful construction of the Roman pots and OMD are late receipt of the final 32x32 channel EICROC ASICs and issues with the bump-bonding and construction of the final staves. There are additional risks related to machine integration.

Additional Material Will add sufficient reference to support documetns as they are compiled.

8.3.7.3 The zero degree calorimeter

Requirements

Requirements from physics: The Zero-Degree Calorimeter (ZDC) plays an important role in many physics topics. The production of exclusive vector mesons in diffraction processes from electron-nucleus collisions is one of the important measurements. For the coherent processes, where the nucleus remains intact, the momentum transfer (t) dependent cross section can be related to the transverse spatial distribution of gluons in the nucleus, which is sensitive to gluon saturation. In this case, however, the coherence of the reaction needs to be determined precisely. Incoherent events can be isolated by identifying the break-up of the excited nucleus. The evaporated neutrons produced by the break-up in the diffraction process can be used in most cases (about 90%) to separate coherent processes. In addition, photons from the de-excitation of the excited nuclei can help identify incoherent processes even in the absence of evaporated neutrons. Therefore, in order to identify coherent events over a wide t range, neutrons and photons must be accurately measured near zero degrees.
The geometry of the collision is important to understand the characteristics of each event in electron-nucleus collisions. It has been proposed that collision geometry can be studied by tagging it with the multiplicity of forward neutrons emitted near zero degrees. Determining the geometry of the collision, such as the "travel length" of the struck partons in the nucleus, which correlates with the impact parameters of the collision, is very useful in the study of nuclear matter effects. Determining the geometry of the collision will allow us to understand the nuclear structure with greater accuracy.

Requirements from Radiation Hardness: In the ePIC radiation doses and particle fluences, ZDC neutron fluence is smaller than 10^{12} neutron/cm^2 for 6 month operation. It is not demanding, but degradation may occur for crystals and/or photon sensors due to radiation

Requirements from Data Rates: Dynamic range of the crystal calorimeter is a clear challenge. $\sim$100 MeV photons from e+A "quasi-coherent" reactions and $\sim$10-100 GeV photons possible from other exclusive processes (Λ decay, u-channel DVCS) should be covered.

Justification

Device concept and technological choice: Add text here.

Subsystem description:

General device description: The Crystal calorimeter needs a good measurement of low-energy photons. The first part of ZDC is designed to use a layer of crystal calorimeter towers which is $8X_0$ in thickness. The layer consists of 2×2 cm^2 crystals in an array of 30×30. LYSO is considered as the material choice for the crystal. SiPM and APD are considered as photo-sensors. The FEE and other components are also under consideration.

Sensors: Add text here.

FEE: Add text here.

Other components: Add text here.

Performance Test beams for crystal calorimeter prototype have been performed and its data analysis is underway. Its prototype modules have been made by Taiwan group. Two simulation calculations and evaluations have been ongoing; Λ identification and low-E photon identification. Angular resolution is a common thread. They have been less-emphasized early-on, but absolute requirements for successful exclusive physics program should be given.

Implementation ZDC implementation would have a benefit from a creative approach; potentially non-static configuration which can be “changed” for different running conditions. The crystal calorimeter need depends on physics channel; some level of conflict in the final states and associated requirements. Having the ability to bring the crystal calorimeter in/out of configuration, as needed, would provide clear benefit to specific physics needs.

Services: Add text here.

Subsystem mechanics and integration: In the current crystal calorimeter prototype module made by Taiwan group, by glueing modules together, 4x4 crystals are made, and then 4 modules are put 64 crystals together. Support and mechanical structure need to communicate with US experts.

Calibration, alignment and monitoring: Add text here.

Status and remaining design effort:

R&D effort: Add text here.

E&D status and outlook: Add text here.

Other activity needed for the design completion: Add text here.

Status of maturity of the subsystem: Add text here.

Environmental, Safety and Health (ES&H) aspects and Quality Assessment (QA planning: Add text here.

Construction and assembly planning: Add text here.

Collaborators and their role, resources and workforce: Add text here.

Risks and mitigation strategy: Add text here.

Additional Material Add text here.

8.3.8 Far backward detectors

The luminosity system at the Electron-Ion Collider plays a critical role in achieving high-precision measurements in nuclear physics experiments. By determining, monitoring and optimizing the number of particle collisions, the luminosity system ensures that the collider operates at peak performance, enabling detailed exploration of the structure of matter. When electrons collide with protons or nuclei, Bremsstrahlung (BH) photons are generated, with a well know cross section []. This process thus provides us with the mean to indirectly determine the luminosity by accurate and precise determination of the Bremsstrahlung photons generated in the interaction region of the collider.

Accurately determining luminosity is essential for addressing the fundamental physics questions that underpin the construction of the Electron-Ion Collider. The Yellow Report specifies the EIC requirements for luminosity determination to be 1% in absolute uncertainty and 10^{-4} in relative luminosity [**?**]. This requirement will be fulfilled by two complementary detectors in the luminosity monitoring system: the Pair Spectrometer (PS) and the Direct Photon Detector (DPD). It was demonstrated at HERA – the first electron-hadron collider – that the bremsstrahlung process can be successfully used to precisely measure the luminosity of high-energy *ep* collisions (ZEUS achieved an absolute uncertainty of 1.7% [**?**, **?**]). The luminosity monitors designed for the EIC utilise the same approach with implementation that mitigates large systematic uncertainties.

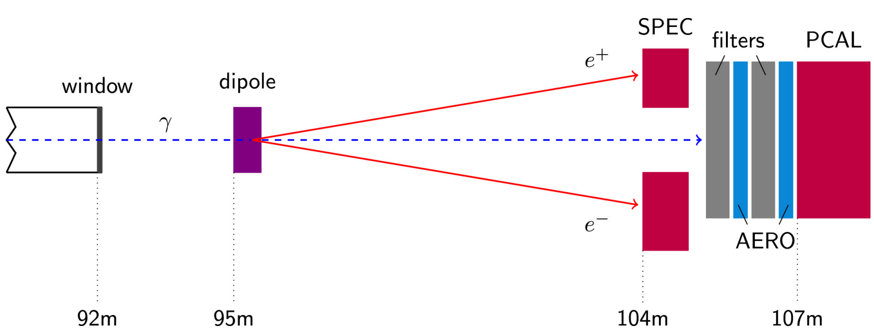

Figure 8.45: The layout of the luminosity monitor in the ZEUS experiment [**?**].

The two subsystems, Pair Spectrometer, and Direct Photon Detector, are sensitive to different systematic effects; on one hand the Direct Photon detector is placed downstream the photon beam with full acceptance, but within the synchrontron radiation fan and needs to be shielded. In addition, at nominal luminosities planned for the EIC several photons will hit the DPD in each bunch crossing. Thus the counting of bremsstrahlung photons is done through the total energy determination deposited in DPD and is associated with systematic uncertainties related to gain stability. On the other hand, the PS is outside the synchrontron radiation fan and overall rates can be controlled with a dedicated converter. The luminosity determination from the PS is sensitive to systematic effects related with the acceptance determination.

The PS and DPD detectors in the ZEUS luminosity monitor are shown in figure (8.45). The PS system consists of an analysing dipole magnet and two electromagnetic calorimeters, while the DPD system includes absorbing plates and an electromagnetic calorimeter. BH photons generated in the interaction region exit the vacuum chamber through a thick exit window. About 10% of these photons (depending on the window's thickness) undergo pair conversion into electron-positron pairs, which are then detected by the PS calorimeters. The remaining unconverted photons are detected by the downstream DPD. Additionally, the luminosity monitor includes a collimator positioned just after the exit window to produce a uniform, narrow cone of photons and pair-converted particles. This simple steel block also protects the PS system components from direct synchrotron radiation (SR), BH radiation, and unwanted stray particles.

The PS was needed at ZEUS due to challenges introduced by upgrades to the HERA accelerator, which significantly increased luminosity and, consequently, the rate of BH events [**?**]. The stronger beam focusing and increased synchrotron radiation (SR) — radiation resulting from the bending of electrons by the magnet—led to a higher pile-up of photons in the DPD, increasing the uncertainty in luminosity measurements from 1% to 3% [**?**]. The PS, positioned outside the SR fan and unconverted photon flux, experienced a lower pile-up due to fractional pair conversion. This introduction reduced the uncertainties in rate measurement to 2% [**?**], and additionally both detectors were utilized to monitor real-time detector inefficiencies and manage systematic uncertainties.

8.3.8.1 The luminosity system

This ZEUS luminosity monitor design serves as a baseline for EIC but the expected luminosity at EIC will be about 10^2 to 10^3 times that of ZEUS [**?**]. This directly leads to several challenges faced during the upgrade of HERA, such as beam size effects (BSE), increased SR backgrounds, and higher pile-up from BH radiation, becoming much more pronounced at the EIC. In addition to these, the EIC will also feature electron beams colliding with a diverse range of hadron species, from protons to heavy nuclei like gold, lead, and uranium. This in turn dramatically increases the BH rates by a factor of Z^2, making pile-up at detectors even more difficult to manage. Furthermore, both the electron and light hadron beams will be polarized, adding another layer of complexity. In the following section, we will discuss these challenges in more detail and outline how the "upgraded" luminosity monitor of EIC will overcome them.

Beam Size Effect - The BH process in electron-proton collisions is notable for its extremely small momentum transfers between the radiating electron and the proton. It is kinetically possible for both particles to continue along their initial paths without angular scattering, while the BH photon is emitted in the direction of the electron's momentum. This specific configuration results in the smallest virtuality ($\mathrm{Q}^2_{\mathrm{min}}$) of the exchanged photon [**?**]. At high-energy colliders, this minimal photon virtuality becomes incredibly small. For instance, at HERA, the Q^2_{min} for a photon energy of 1 GeV can be as low as 10^{-8} eV^2. Consequently, the typical transverse momentum transfer ($q_\perp$) reaches values around 10^{-4} eV/c. Since the BH differential cross section is proportional to Q^{-4}, photon virtualities near Q^2_{min} dominates the process and allows for the approximation,

$$Q^2 = Q^2_{\mathrm{min}} + q^2_\perp$$

and not to forget the scenarios with $q_\perp = 0$ is also feasible. Analyzing the process in impact parameter space reveals that these small $q_\perp$ values correlate to large impact parameters ($b = \hbar/q_\perp$), explaining the precision of Bethe-Heitler cross-section calculations in the Born approximation.

The derivation of the two-particle rate (R) relation with the collision luminosity (L) and cross-section (σ)

$$R = L\sigma \tag{8.1}$$

assumes both beams to be modeled as simple plane waves with a uniform impact parameter distribution. However, this assumption falls short when beams are strongly focused at the interaction point, as focusing suppresses large impact parameters. Consequently, the BH differential cross section is predominantly "over-sampled" at low impact parameters where the cross-section value is smaller. This results in an effective suppression of BH. This is particularly pronounced at lower photon energies, since typical $q_\perp$ is proportional to E_γ.

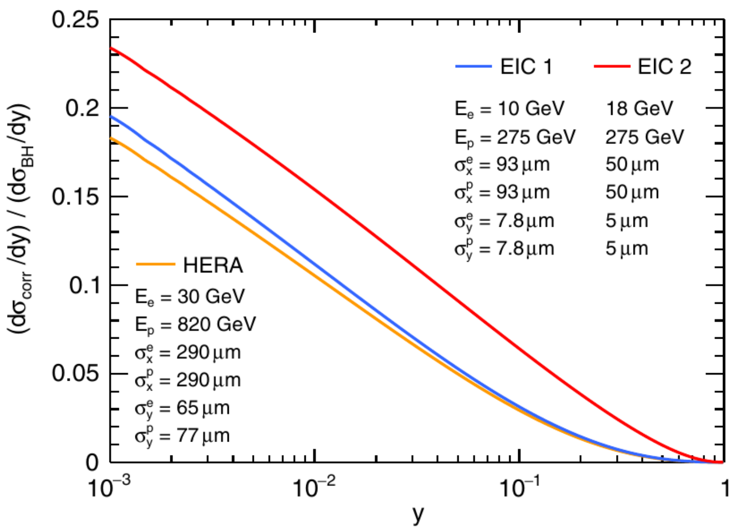

Figure 8.46: Relative suppression due to the BSE $(d\sigma_{corr}/dy)/(d\sigma_{BH}/dy)$ is shown as a function of $y = E_\gamma/E_e$ for three cases of collider parameters, HERA, EIC 1 & EIC 2. The corresponding beam energies and Gaussian lateral beam sizes at the interaction point are listed [**?**].

Relative corrections to the standard Bethe-Heitler cross-sections due to the BSE is shown in figure (8.46). Here the observed suppressed BH cross-section is related to the Bethe-Heitler cross-section as $(d\sigma_{obs}/dy) = (d\sigma_{BH}/dy) - (d\sigma_{corr}/dy)$. It is worth noting that even after higher beam energies at HERA, the BSE will be higher at EIC due to a stronger focused beam as evident from beam size parameters. In a recent study, the BSE is proposed to be corrected by a precise measurement of the BH spectra as a function of lateral beam displacements (indirectly the impact parameter) at the interaction point. This will be achieved using Van der Meer scans, commonly performed at hadron colliders. This involves systematically varying the beam positions and crossing angles to find the L as a function of lateral beam displacement, which can be described by the formula

$$L(B) = L(0)\exp\left(-\frac{B}{2(\sigma_1^2 + \sigma_2^2)}\right)$$

Here, B represents the lateral displacement of one of the beams within either the horizontal or vertical plane, σ_1 and σ_2 are the two Gaussian widths in a given plane, often assumed to be equal, and $L(0)$ corresponds to the luminosity of nominal, head-on collisions. However, in the case of BH, its photon spectrum will also be modified in a very specific manner, reflecting the BSE.

High rate of BH radiation and SR background - The bunch crossing rate at EIC will be set to 100 MHz for 5 and 10 GeV electron beam and 25 MHz for 18 GeV electron beams [**?**]. When this rate is multiplied by the BH photon production rate per bunch crossing, as illustrated in Figure (8.47), the resulting photon rates reaching the detectors looks substantial. For instance, with a 5 GeV electron beam and a 41 GeV proton beam, the coincidence rate (the rate when both the pair converted pairs are detected simultaneously) at the Photon Spectrometer (PS) can reach approximately 90,000 photons per second. The BH photon rates during electron-nuclei interactions will be proportional to the square of nucleus's atomic number. Therefore for the same setup but 41 GeV Gold nuclei beams will result coincidence rate equivalent to $79^2 \times 90000 = 56 \times 10^7$ photons per second.

SR, similar to BH radiation, is emitted at very small angles ($\sim m_e/E_e$) relative to the instantaneous direction of an electron beam's motion. At the EIC, the electron beam exiting the interaction region passes through two quadrupole magnets, Q1eR and Q2eR, followed by a dipole magnet, B2eR. The electron beam passes through the center of the quadrapoles and consequently, the B2eR magnet is the sole source of direct SR impacting the far-backward region. [Calculation of SR rates at EIC? Comment quantitatively on how much sweeper helps in subsequent paragraph.]

To address the issue of high photon flux and its associated pile-up, as well as to mitigate the high SR background, the luminosity monitoring system has been redesigned to include two new components: a sweeper magnet and a thin converting foil, both positioned between the EW and the spectrometer magnet, as illustrated in Figure (8.48). The enormous BH radiation and SR pass through the exit window, resulting in substantial pair conversions. These converted particles are deflected by the Sweeper magnet, leading to a reduced photon flux, with a large percentage being BH photons. These photons then encounter a thin converter made of the same material as the exit window. This setup results in fewer pair conversions reaching the PS and an overall reduced photon flux to the DPD.

For electron beams at 10 and 18 GeV, the SR flux is substantial, with power reaching the exit window potentially exceeding 4 kW. To mitigate this, it was proposed to divide the dipole magnet into two segments. The first segment, relevant to luminosity detectors, has a magnetic field about four times weaker than that of B2eR. This modification is crucial to minimize the direct SR flux, which is vital for accurate luminosity measurements, as it influences both PS and DPD readings [**?**].

Beam Polarisation - The electron and light ion beams at the EIC will be polarized both longitudinally and transversely. A recent study investigated the impact of longitudinal beam polarization on the Bremsstrahlung cross-section in the low-q^2 region [**?**]. Numerical calculations revealed that the polarized component is significantly suppressed compared to the unpolarized component, by a factor of $m_e^2/E_e E_p$. Figure (8.49) illustrates the unpolarized component first calculated by Bethe-Heitler, alongside the polarized component. However, no calculation exists for transversely polarised beams and also with the effect of nuclear recoil.

Physical Constraints - The components of the luminosity monitoring system are placed within the beam tunnels and are therefore constrained by the beam pipes and the equipment required to maintain the beam, such as magnets and cooling systems. The majority of the system is located

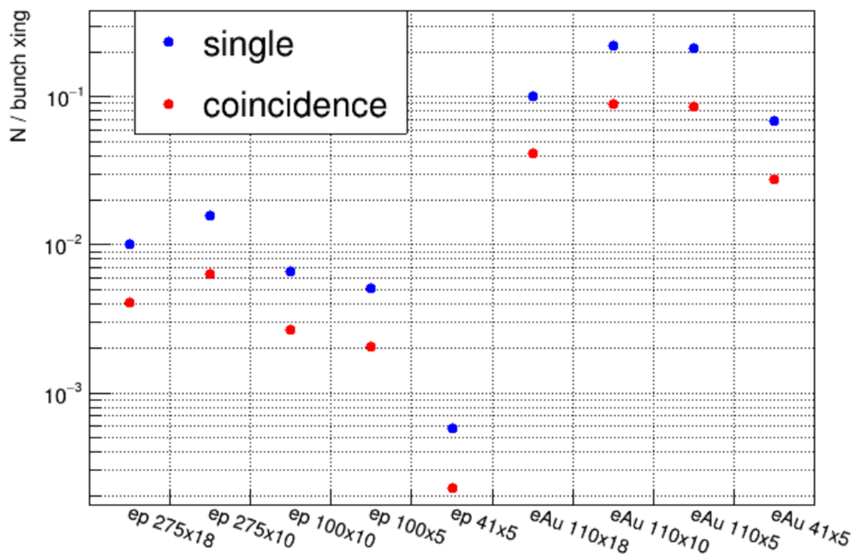

Figure 8.47: Rate of single and coincidence events for the PS detectors calculated by Dr. Gangadharan

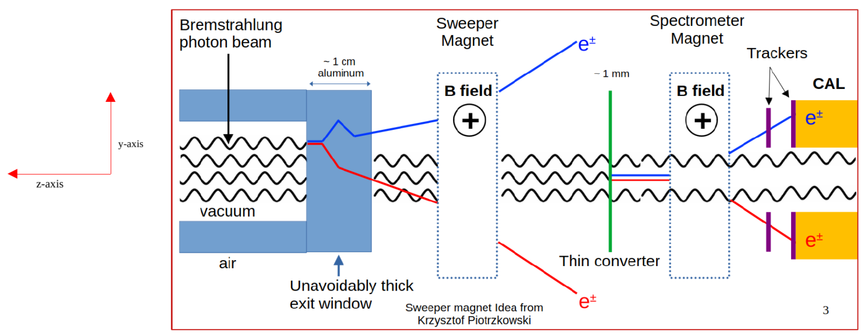

Figure 8.48: The layout of the luminosity monitor in the ePIC experiment of the EIC.

sixty meters back from the interaction region to provide sufficient space for the magnets and detectors to operate without interfering with the beam. The long air column between the exit window and the PS calorimeters is approximately 46 meters. The "unconverted" photon beam from the exit window undergoes pair conversions, which are quite significant (approximately 10%) and indeterminate during experimentation due to variability in air composition. Most of the unwanted pair conversions occur between the exit window and the sweeper magnet and are swept away by the sweeper. To reduce pair conversions in the air column between the sweeper magnet and the spectrometer magnet, a helium or partial vacuum chamber will be installed between the magnets. The thin converter will remain at the same location but will be placed inside this vacuum chamber.

Add paragraph outlining requirements on magnets imposed by physical space limitations.

Systematic Uncertainties - The systematic uncertainty in the luminosity measurement at ZEUS was 1.7 %, and our goal is to reduce this value to below 1 %. Table 8.13 summarises the main systematic uncertainties that contributed to the ZEUS luminosity determination. In our current

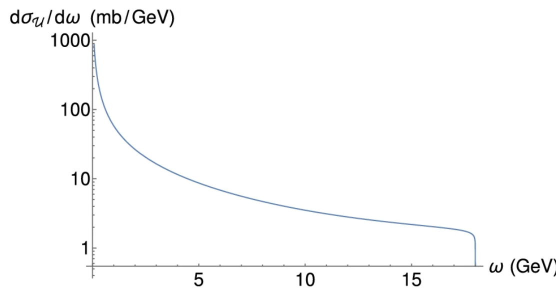

(a) Unpolarised Part

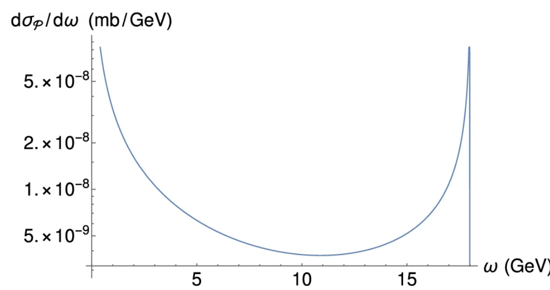

(b) Polarised Part

Figure 8.49: Unpolarised and polarised Bethe-Heitler Cross-Section. [?]

design, we ensure we mitigate the largest of these sources with the introduction of trackers for the PS, that would enable an accurate determination of the detector acceptance and beam size effects, and a sweeper magnet that allows us to have more control on the converted pair rates in the PS.

Source	DPD detector (%)	PS detector (%)
Acceptance	1.0	1.0
x-position of photon beam	1.2	1.2
Pair conversion in EW		0.7
RMS Cut Correction		0.5
Pedestal Shifts	1.5	
Pile up	0.5	
Total	2.2	1.8

Table 8.13: Summary of systematic uncertainties at ZEUS DPD and PS detector. [?]

Design and Components A two-level review of all the components of luminosity monitor is presented below. First, a short review on the component's material, location & dimension, and a longer version with detailed description of each component requirement, design with simulation or test-beam results. Note that all length measurements are in centimeters unless otherwise mentioned.

- Exit Window

  - Material - Aluminum
  - Location - (0.0, 0.0, - 1850.5)
  - Dimension - (4.0, 4.0, 1.0)
- Collimator
  - Material - Stainless Steel
  - Location - (0.0, 0.0, - 2260.0)
  - Hollow Structure, Outer Dimension - (6.5, 6.5, 30.0), Inner Dimension - (4.832, 4.832, 30.0)
- Sweeper Magnet
  - 0.5 T horizontal magnetic field.
  - Location - (0.0, 0.0, - 5600.0)
  - Main Body Structure, Outer Dimension (75.972, 94.0, 120.0), Inner Dimension - (42.032, 61.262, 120.0)
  - Magnetic Coils Structure (How to describe ?)
- Photon Vacuum Chamber
  - Material - Pipe : Aluminum & End caps : Beryllium
  - Location - (0.0, 0.0, - 5800.0)
  - Pipe Structure, Outer Dimension (6.3119, 2π rad, 555.0), Inner Dimension (6.119, 2π rad, 555.0)
- Converter Foil
  - Material - Aluminum
  - Location - (0.0, 0.0, - 5800.0)
  - Disk Dimension - (6.119, 2π, 0.1)
- Spectrometer Magnet
  - Location - (0.0, 0.0, - 6000.0)
  - Main Body Structure, Outer Dimension (75.972, 94.0, 120.0), Inner Dimension - (42.032, 61.262, 120.0)
  - Magnetic Coils Structure (How to describe ?)
- PS Trackers
  - Type - AC-LGAD
  - Locations
    * Module 1 : Top (0.0, 15.76, - 6397.6) and Bottom (0.0, - 15.76, - 6397.6)
    * Module 2 : Top (0.0, 15.76, - 6407.6) and Bottom (0.0, - 15.76, - 6407.6)
  - Dimension - (18.06, 18.06, 0.044)
- PS Calorimeters
  - Type - Electromagnetic sampling (spaghetti) calorimeter
  - Material - Active : Scintillating Fiber (ScFi) and Passive : Tungsten (W)

    * Tungsten as powder, held together with optical epoxy.
  - Location - Top (0.0, 15.76, -6408.6) and Bottom (0.0, - 15.76, - 6408.6)
  - Dimension - (18.06, 18.06, 17.2)
- DPD Calorimeters

Exit window

- Needs exact study of its composition and irradiation studies.

Collimator

- Do we need any further study ?

Sweeper and Spectrometer magnet

- Mapping the magnetic field. Need info from magnet experts

Photon Vacuum Chamber

- need info from accelerator

The thickness of the exit window for electrons and positrons must be minimized to reduce material interactions. However, if a vacuum chamber is selected instead of helium filled, a minimum thickness of the exit widnow is required to withstand a pressure difference of 1 atm. The minimum thickness of beryllium should exceed 3 mm to ensure structural integrity under these conditions.

- Mapping the Pressure
- Study of exact composition and thickness of two end caps.

Converter Foil The converter foil is expected to operate in a vacuum, necessitating heat removal due to synchrotron radiation (SR). Heat removal from the converter can be achieved through the holder, utilizing one of two options: passive cooling or circulation of a coolant.

- Study of exact composition, thickness and radiation dose.
- Study of pair conversion percentage.
- How this will reduce the error in position resolution.
- Heat removal due to SR radiation.

PS Trackers

- PS trackers are required to reconstruct the vertex position at the conversion foil, which has a direct impact on determining acceptance. A vertex resolution of less than 6 mm is necessary to achieve an acceptance determination uncertainty of less than 1%.
- This has not been studied yet; however, since the PS system is located away from the IP and positioned behind collimators and magnets, and not within the BH cone, the radiation levels are expected to be manageable.
- AC-LGADs are chosen for their excellent position and timing performance. Due to the relatively small detection area and the fact that this technology is planned for FTOF, PS trackers will utilize a similar design.
- Initial studies with the nominal 500 μm pitch are expected to provide a 2 mm resolution at the vertex (conversion foil).

The tracking layers for the PS system are based on AC-LGAD technology with pixelated sensors. Each side will consist of two tracking layers, resulting in a total of four layers. AC-LGAD sensors will be placed on modules similar to the FTOF design. The pitch between the readout pads, set at 500 μm, is expected to provide approximately 70 m position resolution at the detector plane and around 2 mm at the vertex (conversion foil). Current estimations indicate that, in order to achieve acceptance uncertainties below 1%, the vertex resolution in the dispersive direction must be less than 6 mm. With a 500 μm pitch, the number of readout channels is estimated to be about 130,000 per plane. To minimize the number of DAQ channels, the number of pixels in the non-dispersive direction could be combined.

PS Calorimeters The two electromagnetic calorimeters (CALs) used for the PS are of the sampling type, colloquially known as spaghetti CALs. The active component of the CAL consists of plastic scintillating fibers (ScFi), while the passive, or "hard," component is tungsten (W). The volumetric ratio of W to ScFi in each CAL is 4:1. The CALs are composed of 20 layers, with the fibers in alternate layers oriented parallel to either the x-direction or y-direction in the transverse plane. This alternating orientation in 10 layers along each direction aids in reconstructing the shower profile of hits, thereby enhancing the position resolution of hits. Each layer has a thickness of 0.86 cm and a transverse size of 18.06 × 18.06 cm^2. Additionally, the layers are segmented into three modules, each with a width of 6.02 cm. Each module contains well-distributed 448 ($14 \times 2 \times 16$) fibers. Finally, a group of 16 fibers forms a single channel for readout. Each readout will be associated with a silicon photo-multiplier (SIPM).

The two PS CALs are symmetrically positioned in the vertical plane, perpendicular to the photon flux i.e., along the y-axis. The gap between the two CALs is approximately 3σ, which is sufficient for the detectors to not obstruct the final photon flux from reaching the DPD. The PS CALs serve the purpose of measuring the energy and the transverse coordinates of the pair-converted photons, which enables the reconstruction of the photon energy spectrum and thus the determination of the beam luminosity.

The acceptance of PS system is effected by four major parts of the PS system.

- The collimator which obstructs some part of BH photons.
- The sweeper magnet which removes the pair-conversions from EW.
- The front end cap of the vacuum chamber whose pair-conversions are not detected in CALs.

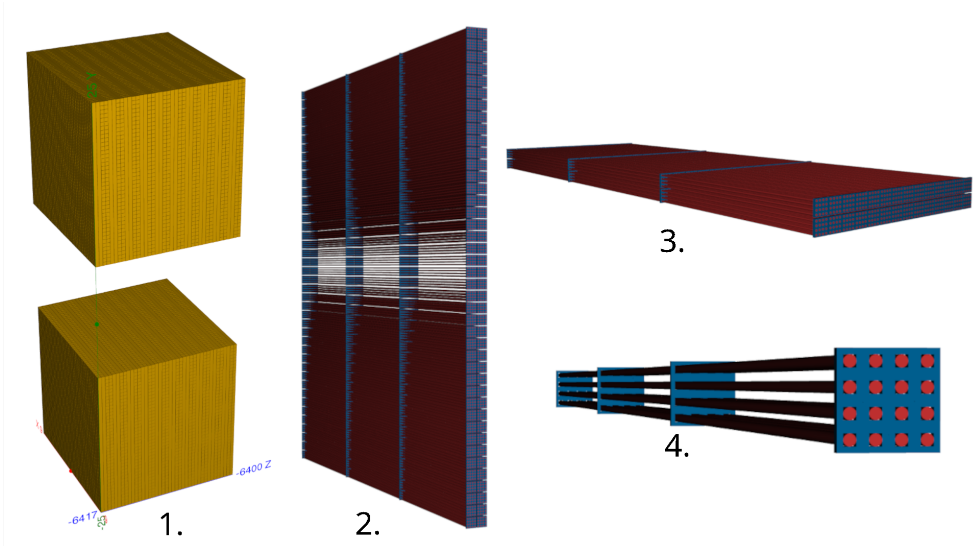

Figure 8.50: DD4hep implementation of PS Calorimeters.

- The fiducial areas of the CALs whose signals are rejected.

Plot the acceptance curve.

DPD

Collaborators and their role, resources and workforce: The main collaborating institutions for the PS calorimeter are York and Houston. The roles of each institution are outlined below -

- University of York, United Kingdom
  - Design and construction of calorimeters
  - Calorimeter simulation
  - Calorimeter reconstruction and analysis
  - DAQ and electronics for calorimeter
- University of Houston, Texas, USA
  - Calorimeter simulation
  - Calorimeter reconstruction software
  - Calorimeter design support
- Tel Aviv University, Israel
  - Design and integration of PS trackers.
  - Simulation.

The workforce at each institution is comprised of -

- University of York, United Kingdom
    1. Dan Watts, academic staff (20-25 % FTE)
    2. Nick Zachariou, academic staff (25-30% FTE)
    3. Mikhail Bashkanov, academic staff (10-15% FTE)
    4. Stephen Kay, PDRA (100% FTE)
    5. Alex Smith, PG Student (100% FTE)
    6. Pankaj Joshi, academic support staff (5% FTE)
    7. Julien Bordes, Geant4/simulation support (10-15% FTE)
    8. Technical Support Staff
        - Electrical engineering
        - Mechanical engineering
        - CAD support
- University of Houston, Texas, USA
    1. Dhevan Gangadharan, academic staff (X% FTE)
    2. Aranya Giri, PG Student (100% FTE)
- Tel Aviv University, Israel
    1. Igor Korover, academic staff (15% FTE)
    2. Avishay Mizrahi, Mechanical engineer (50% FTE).

Note that where an FTE range is presented, this represents a min/max value.

Risks and mitigation strategy: Add text here.

Additional Material Add text here.

8.3.8.2 The low Q^2 taggers

Requirements

Requirements from physics: Add text here.

Requirements from Radiation Hardness: Add text here.

Requirements from Data Rates: Add text here.

Justification

Device concept and technological choice: Add text here.

Subsystem description:

General device description: Add text here.

Sensors: Add text here.

FEE: Add text here.

Other components: Add text here.

Performance

Implementation

Services: Add text here.

Subsystem mechanics and integration: Add text here.

Calibration, alignment and monitoring: Add text here.

Status and remaining design effort:

R&D effort: Add text here.

E&D status and outlook: Add text here.

Other activity needed for the design completion: Add text here.

Status of maturity of the subsystem: Add text here.

Environmental, Safety and Health (ES&H) aspects and Quality Assessment (QA planning: Add text here.

Construction and assembly planning: Add text here.

Collaborators and their role, resources and workforce: Add text here.

Risks and mitigation strategy: Add text here.

Additional Material Add text here.

8.3.9 Polarimeters

Add text here.

8.3.9.1 The electron polarimeters

Requirements

Requirements from physics: Add text here.

Requirements from Radiation Hardness: Add text here.

Requirements from Data Rates: Add text here.

Justification

Device concept and technological choice: Add text here.

Subsystem description:

General device description: Add text here.

Sensors: Add text here.

FEE: Add text here.

Other components: Add text here.

Performance

Implementation

Services: Add text here.

Subsystem mechanics and integration: Add text here.

Calibration, alignment and monitoring: Add text here.

Status and remaining design effort:

R&D effort: Add text here.

E&D status and outlook: Add text here.

Other activity needed for the design completion: Add text here.

Status of maturity of the subsystem: Add text here.

Environmental, Safety and Health (ES&H) aspects and Quality Assessment (QA planning: Add text here.

Construction and assembly planning: Add text here.

Collaborators and their role, resources and workforce: Add text here.

Risks and mitigation strategy: Add text here.

Additional Material Add text here.

8.3.9.2 The proton polarimeters

Requirements

Requirements from physics: Add text here.

Requirements from Radiation Hardness: Add text here.

Requirements from Data Rates: Add text here.

Justification

Device concept and technological choice: Add text here.

Subsystem description:

General device description: Add text here.

Sensors: Add text here.

FEE: Add text here.

Other components: Add text here.

Performance

Implementation

Services: Add text here.

Subsystem mechanics and integration: Add text here.

Calibration, alignment and monitoring: Add text here.

Status and remaining design effort:

R&D effort: Add text here.

E&D status and outlook: Add text here.

Other activity needed for the design completion: Add text here.

Status of maturity of the subsystem: Add text here.

Environmental, Safety and Health (ES&H) aspects and Quality Assessment (QA planning: Add text here.

Construction and assembly planning: Add text here.

Collaborators and their role, resources and workforce: Add text here.

Risks and mitigation strategy: Add text here.

Additional Material Add text here.

8.3.10 Readout Electronics and Data Acquisition

Requirements The electronics and data acquisition systems are required to digitize and readout the data provided by the sensors of all ePIC detectors. The Electronics must tag hits with a time resolution sufficient to identify the bunch crossing (10.16ns) and provide high resolution time references as stringent as 5ps according the specific detector needs. The ePIC readout system must provide high data volume links to front end electronics up to 10Gb/s for selected components. The readout system must provide very high live times, with the goal of zero-system wide deadtime in normal operation, despite the possibility of by-channel deadtime according the specific readout technology of each detector.

Detector Group	Channels					Det Fiber Down	Det Fiber Up	RDO	Fiber Pair (DAQ)	DAM	Data Volume (RDO) (Gb/s)	Data Volume (To Tape) (Gb/s)
	MAPS	AC-LGAD	SiPM/PMT	MPGD	HRPPD/ MCP-PMT							
Tracking (MAPS)	16B					183	5863	183	183	7	15	15
Tracking (MPGD)				164k		160	640	160	160	5	27	5
Calorimeters	500M		100k					510	510	17	70	17
Far Forward		1.5M	10k					80	80	6	36	12
Far Backward	66M	128k	4k					60	82	14	301	16
PID (TOF)		6.1M				500	1364	500	500	14	50	12
PID Cherenkov			318k		143k			1283	1283	32	1275	32
TOTAL	**16.6B**	**7.7M**	**432k**	**164k**	**143k**	**843**	**7,867**	**2,776**	**2,798**	**95**	**1,774**	**109**

Figure 8.51: ePIC DAQ component count summary

The Data Acquisition will group streaming data into time frames of O(0.6ms). The readout systems are expected to digitize up to O(2Tb/s) and must be capable of reducing this data volume to an output rate of O(100Gb/s) using techniques to compress signal and remove noise with minimal impact to signal integrity. The data from all running detectors for each time frame will gathered together in a single buffer for transfer to the echelon 1 computing facilities located at BNL and JLAB for archive and analysis.

Requirements from Physics The scientific mission of ePIC is reflected in the requirements of the Electronics and DAQ through the scale and technology of the ePIC detectors shown in figures 8.51 and 8.52. Large channel counts combined with low occupancy lead to the need for multiple levels of aggregation at the Front End Boards (FEB), the Readout Boards (RDO) and the Data aggregation and Manipulation Boards (DAM).

The performance of the EIC Collider also impacts the requirements of the readout system. The collision rates and background rates are detailed in section **??**. Two aspects are particularly important for the Electronics and DAQ.

The first is the maximum event rates, which we expect to be as high as 500kHZ for DIS, 3.2Mhz for Electron Beam Gas and 32kHz for hadron Beam Gas. These rates are of primary interest within DAQ to estimate the data volumes which are described below.

The second consideration is that individual bunch crossing can have different polarization states. This implies that the luminosity and polarization of the beams must be tracked by bunch and produces the requirement that events must be associated to the bunch crossing from which they originated.

Requirements from Radiation Hardness The electronics installed in the ePIC detector will be subjected to significant radiation doses. Radiation doses are described in section **??**. Electronics placed in the central detector (SVT, eTOF, bTOF, and MPGDs) will utilize radiation hard components to minimize the effect of radiation.

Electronics must be chosen and placed to minimize failure rates. Transient failures such as single bit upsets (SEUs) must have a recovery process which automatically senses, initiates, and accomplishes recovery while running in order to avoid downtime. There are commercial IP cores available for FPGAs that can support recovery from simple SEUs. More complex (multi-bit) failures will require an automated reset and reload feature for FEBs and RDOs.

Detector System	Channels	ASIC	FEB	RDO	Gb/s (RDO)	Gb/s (Tape)	DAM Boards	Readout Technology	Notes
Si Tracking: Inner Barrel (IB)	1.8B Pixels	160	592	24	2.36	2.36	1	ITS-3 sensors &	ASIC corresponds to VTRX+ counts
Outer Barrel (OB)	5.0B Pixels	495	1870	55	3.52	3.52	2	ITS-2 staves / w	FEB corresponds to detector fiber
Backward Disks (EE)	4.7B Pixels	462	1744	52	4.68	4.68	2	improvements	RDO is off detector Fiber aggregator
Forward Disks (HE)	4.7B Pixels	462	1744	52	4.68	4.68	2		
MPGD tracking: Electron Endcap	16,384	256	64	16	2.86	0.58	1	uRWELL / SALSA	VTRX+ based FEB
Hadron Endcap	16,384	256	64	16	4.01	0.80	1	uRWELL / SALSA	
Inner Barrel	32,768	512	128	32	4.10	0.82	1	MicroMegas / SALSA	
Outer Barrel	98,304	1536	384	96	15.81	3.16	2	uRWELL / SALSA	
Forward Calorimeters: LFHCAL	63,280	1130	1130	74	18.54	2.47	2	SiPM / CALOROC	CALOROC:
HCAL insert	8k	142	142	9	17.72	2.36	1	SiPM / CALOROC	56 Ch/CALOROC
ECAL W/SciFi	16,000		500	64	14.75	7.36	2	SiPM / Discrete	16 CALOROC / RDO
Barrel Calorimeters: HCAL	1,536	28	28	2	0.87	0.12	1	SiPM / CALOROC	
ECAL SciFi/PB	5,760	102	102	4	11.45	1.52	1	SiPM / CALOROC	Discrete:
ECAL ASTROPIX	500M pixels			340	1.25	1.25	8	Astropix	32 Ch/FEB,
Backward Calorimeters: NHCAL	3,256	58	58	4	3.46	0.47	1	SiPM / CALOROC	8 FEB/RDO conservative (16 estimate).
ECAL (PWO)	2,852		102	13	2.00	0.99	1	SiPM / Discrete	
Far Forward: B0: Crystal Calorimeter	135		5	1	2.3	2.3	1	SiPM/APD / Discrete	
4 AC-LGAD layer	688,128	672	168	42	12.75	2.1	1	AC-LGAD / EICROC	4 layer x 42 module x 4 EICROC x 1024 ch
2 Roman Pots	524,288	512	128	32	14.53	2.1	1	AC-LGAD / EICROC	2 stations x 2 layer x 32 module x 4 EICROC x 1024 ch
2 Off Momentum	294,912	288	72	18	3.53	0.7	1	AC-LGAD / EICROC	2 stations x 2 layer x 18 module x 4 EICROC x 1024 ch
ZDC: Crystal Calorimeter	900		30	4	2.30	4.5	1	SiPM/APD / Discrete	
HCAL	9,216	165	165	11	0.22	.22	1	CALOROC	
Far Backward: 2 x Low Q Tagger	66M pixels	3456	288	24	37	.3	10	Timepix4	Firmware Trigger to reduce output rate
2 x Low Q Tagger Cal	420			1	-	-	1	SiPM / CALOROC	Low Q Calorimeter doesn't run at high luminosity
2 x Lumi PS Calorimeter	3,360			1	19	7	1	SiPM / Discrete	
2 x Lumi PS tracker	128k	1000	250	64	45	2	2	AC-LGAD: FCFD or EICROCx	
Direct Photon Lumi Cal	100		24	24*	200	7	1	SiPM / fADC250	Direct Photon: commercial digitizer, no RDO
PID-TOF: Barrel	2,359,296	18,432	288	288	15.95	4.79	8	AC-LGAD: FCFD or EICROCx	bTOF 128 ch/ASIC, 64 ASIC/RDO
Endcap	3,719,168	3,632	212	212	33.92	7.34	6	AC-LGAD: EICROC	eTOF 1024 pixel/ASIC, up to 28 ASIC/RDO
PID-Cherenkov: dRICH	317,952	4968	4968	1242	1240	13.5	30	SiPM / ALCOR	Worse case after radiation. Includes 30% timing
									window. Requires further data volume reduction
pfRICH	69,632	544	68	17	24	12.5	1	HRPPD / FCFD or EICROCx	Firmware trigger
DIRC	73,728	576	144	24	11	6	1	MCP-PMT / FCFD or EICROCx	

Figure 8.52: ePIC DAQ component counts

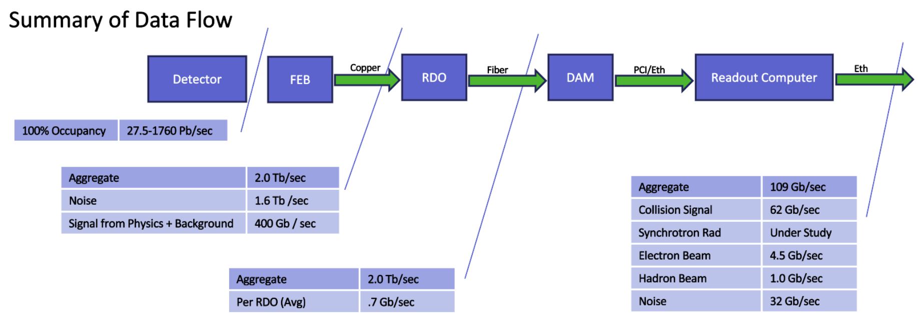

Figure 8.53: Expected worse case data rates contributions for the ePIC detector

Detector	Channel Max Hit Rate (Hz)	Noise To RDO (gbps)	Noise Per RDO (gbps)	Noise To Tape (gbps)	RDO (max) (gbps)	RDO_max / with Noise (gbps)
SiBarrelTracker	4.13E-04	3.25	0.06	3.25	0.00	0.06
SiBarrelVertex	5.22E-03	1.15	0.05	1.15	0.17	0.21
SiEndcapTracker	2.78E-03	6.02	0.06	6.02	0.23	0.29
BackwardMPGDEndcap	2.19E+02	1.74	0.11	0.35	0.42	0.52
ForwardMPGDEndcap	4.44E+02	1.74	0.11	0.35	0.86	0.97
MPGDBarrel	8.67E+01	3.26	0.10	0.65	0.04	0.14
OuterMPGDBarrel	1.29E+01	15.23	0.16	3.05	0.01	0.17
LFHCAL	2.10E+04	10.33	0.14	1.38	1.30	1.44
HcalEndcapPInsert	6.18E+04	1.31	0.15	0.17	2.78	2.93
EcalEndcapP	1.51E+05	0.78	0.01	0.35	2.69	2.70
HCcalEndcapN	7.81E+04	0.53	0.13	0.07	2.64	2.77
EcalEndcapN	8.07E+04	0.14	0.01	0.06	1.06	1.07
HcalBarrel	1.30E+03	0.25	0.13	0.03	0.08	0.21
EcalBarrelImaging	2.92E-02	0.32	0.00	0.32	0.01	0.01
EcalBarrelSciFi	1.52E+03	0.94	0.07	0.13	2.69	2.76
TOFBarrel	1.74E+00	13.59	0.05	4.53	0.01	0.06
TOFEndcap	8.34E-01	32.13	0.15	7.14	0.07	0.22
hpDIRC	2.35E+02	3.22	0.13	1.07	0.00	0.13
pfRICH	4.99E+02	3.05	0.18	1.02	0.00	0.18
dRICH	1.09E+02	1220.94	0.98	6.10	0.00	0.98
B0 Crystal Calorimeter	2.66E+05	0.00	0.00	0.00	0.00	0.00
B0 AC-LGAD	1.72E+01	5.95	0.20	1.32	0.00	0.20
RP	3.31E+01	4.53	0.21	1.01	0.00	0.21
OM	5.93E+00	2.53	0.21	0.56	0.00	0.21
ZDC Crystal Calorimeter	7.81E+04	0.02	0.00	0.02	0.00	0.00
ZDC HCAL	3.39E+01	0.20	0.02	0.20	0.00	0.02
DirectPhoton	2.00E+08	0.00	0.00	0.00	0.00	0.00
LowQ2Tracker	8.76E+00	0.04	0.00	0.04	0.00	0.00
LowQ2Calorimeter	0.00E+00	0.01	0.01	0.01	0.00	0.01
PairSpectrometerTracker	2.44E+02	0.74	0.07	0.25	0.00	0.07
PairSpectrometerCalorimeter	3.26E+04	0.07	0.07	0.07	0.00	0.07
Total		1334.01		40.67		

Figure 8.54: Maximum data volume per RDO with noise estimates.

Detector	Noise (hz/channel)
ITS3, Astropix, Timepix	0.01
AC-LGAD	30
HRPPD	230
dRICH(initial)	3000
dRICH(Max)	300,000
All Others	4.5σ = 340

Table 8.14: Noise Estimates

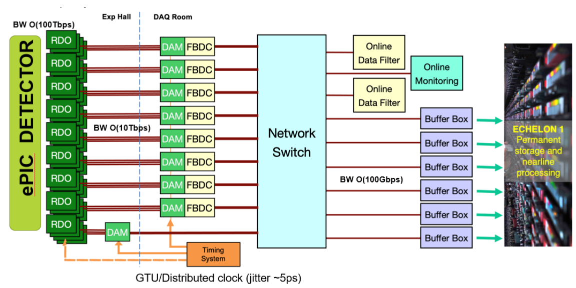

Figure 8.55: Schematic of the ePIC Streaming DAQ

Requirements from Data Rates The triggerless readout of the ePIC detector uses zero-suppression to help manage the volume of data read out. The streaming model's sensitivity to noise, beam background, and collision data make the understanding of these effects critical. Collision, synchrotron radiation and beam gas backgrounds from both the electron and hadron beams have been studied extensively by the ePIC collaboration, and the methods are presented in section **??**. The hits have been converted to data volumes using our current understanding of zero suppression and data formats of each detector readout. Furthermore, the distribution of hits to each component has been estimated by arbitrarily assigning readout components to the sensitive planes of the detectors in order to estimate the impact of potential bottlenecks.

The hit rate for the collision signal is taken from simulated hits for DIS events generated by the ePIC physics and detector simulations. The simulated data set was taken for 18x275 GeV collisions with $Q^2 > 0$ with luminosity $1.54x10^{33}cm^2s^{-1}$. The collision rate was 83kHz, but the hit rates were scaled to the maximum rate of the EIC collider of 500kHz. Hadron and electron beam gas events were generated using the simulated vacuum profile after 10,000Ah of pumping. Noise calculations are currently based on the ePIC detector group expert estimates and shown in table 8.14.

One additional factor that must be considered is dark currents in the SiPM detectors which increase with radiation damage. In particular, this issue affects the dRICH, in which the SiPM threshold must remain low enough to be sensitive to single photons. There are several features planned to reduce these dark currents including annealing, and implementation of timing windows to synchronise readout with collision times. These are described in section **??**. The DAQ system must be designed with the capability to manage the highest rates expected by the dRICH and must also apply filters to reduce the dRICH noise, either by applying a firmware trigger or by using specialized AI algorithms to determine which hits correspond to a dRICH physics signal.

Finally, noise is expected to be a potential issue in all other detectors as well. Generally, the noise level can be controlled with thresholds. The acceptable noise levels by detector is planned to be set according to the bandwidth requirements. The maximum data volume per RDO with estimated noise is summarized in table 8.54.

Device Concept and Technological choice: Streaming Readout The ePIC readout system will implement a flexible, scalable, and efficient streaming DAQ as outlined by the EIC Yellow Report. This design will provide the advantages of streaming include the replacement of custom L1 trigger electronics with commercial off-the-shelf (COTS) computing, virtually deadtime-free operation, great flexibility in event selection using full event data along with offline analysis, and the opportunity to study event backgrounds in detail. These advantages come at the cost of greater sensitivity to noise and background. A schematic of the readout system is show in figure 8.55.

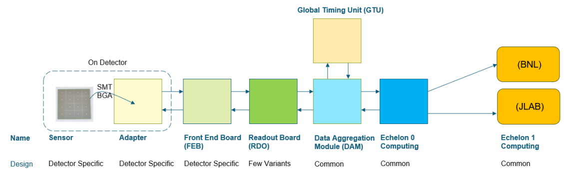

Figure 8.56: Components of the ePIC Streaming DAQ System

The components in the ePIC readout system are shown in figure 8.56. Readout will be accomplished using detector specific front end sensors and adaptors. Even though the organization of the front end electronics varies by detector needs the custom electronics of each system generically referred to as Front End Boards (FEBs). There is no global trigger system in ePIC, instead each FEB is required to self-trigger, providing a stream of hit data. Digitization and zero-suppression is typically handled with ASIC support. Each FEB has similar needs for clocks, configuration, and serial data links. These needs are provided by Readout Boards (RDOs). The RDOs also aggregate data from the FEBs. The RDOs are driven by either FPGAs or lpGBT. The RDO serves as an interface between custom, technology driven, readout schemes of specific detectors and the ePIC DAQ. While there are a number of variations of the RDOs depending upon the FEB technology, all of the RDOs support a unified ePIC DAQ fiber protocol. They distribute high-resolution time reference, configuration, and control to the FEBs and transmit hit data and monitoring information to the Data Aggregation and Manipulation Boards (DAM).

The DAM boards have significant processing available for implementing firmware triggers and other data reduction algorithms. They also provide further aggregation and function as the interface between the electronics and the first level of COTS computers called the Frame Builder Data Collectors (FBDC). The farm of COTS DAQ computers dedicated to readout, data reduction, logging, monitoring, QA and data buffering and transfer to data centers is integrated in the ePIC computing model and referred to as echelon 0.

Synchronizing the front end electronics and provide high resolution time reference to beam crossings is an important requirement of the streaming DAQ. The Global Timing Unit (GTU) is the interface to EIC collider controls. It receives the 98.5Mhz bunch crossing clock and distributes it via the DAM boards to the RDOs and FEBs. The GTU is the only global source of real time information provided to the FEB/RDOs, so it must provide information a trigger system would normally provide. These functions include the ability to synchronize data from different detectors, to send flow control signals, to pass bunch information such as spin orientations and bunch structure, the ability to provide user defined signals for signaling special data formatting or calibration needs, and the ability to implement a hardware trigger for debugging or as a fallback option to solve unforeseen readout issues.

The communication between the RDOs, DAM, and GTU will use an unified data protocol serving four functions:

- The distribution of configuration information from the DAQ System to configure the RDOs, and to distribute configuration information to the FEBs via the RDOs using their serial links,
- The distribution of real-time control information to the RDO and FEBs,
- The distribution of a high-resolution beam crossing timing signal to the RDO and FEBs,
- The high performance (∼10Gb) transfer of hit data and monitoring information from the FEBs and RDO to the DAM boards.

Implementation	Detector/Sensor	Key Attributes
Discrete	Calorimeter/SiPM	COTS devices, 14-bit digitization
CALOROC	Calorimeter/SiPM	ASIC, 10-bit digitization
EICROC	AC-LGAD, pixel	ASIC, High-precision timing for Cd < 5 pF
FCFD	AC-LGAD, strip	ASIC, High-precision timing for Cd < 10 pF
ALCOR	dRICH/SiPM	ASIC, uses shutter for 1 p.e. sensitivity
SALSA	MPGD	ASIC, peaking time to 50 ns, includes DSP

Figure 8.57: ePIC Electronics and ASICs summary

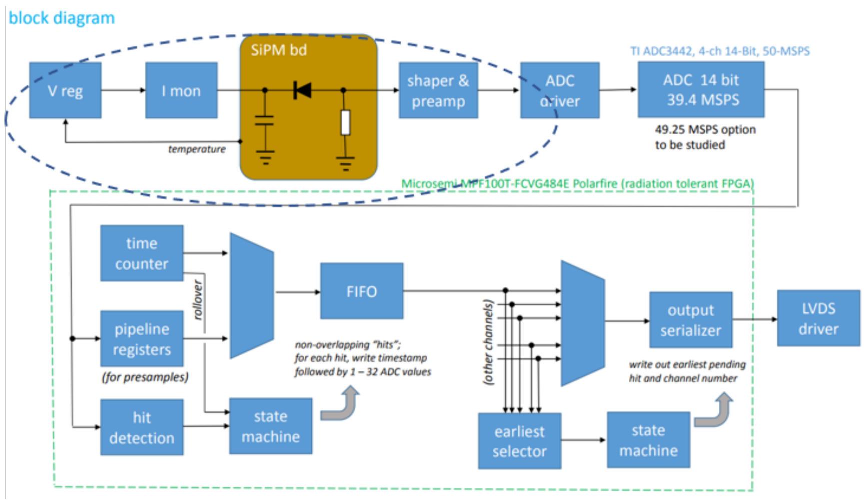

Figure 8.58: Discrete block diagram

Subsystem Description (components)

Readout Electronics and ASICS

Overview Readout electronics is being developed based on the sensor technologies. Common requirements among various sub-detectors have been identified to maximizing synergy. The readout electronics conforms to the ePIC streaming readout model with triggerless operation and serial interfaces. To facilitate calibration and debugging, capability for triggered operation is also implemented. The development of the readout electronics and ASICs are summarized in figure 8.57.

Discrete The Discrete readout implementation addresses the readout from calorimeters with SiPMs where high resolution digitization is required and commercial devices (COTS) are employed. The design and technologies will be validated for specific locations within the ePIC detector, where radiation hardness of COTS devices will need to be verified. The block diagram is shown in figure 8.58.

The circled area in fig. 8.58 delineates the Adapter section with SiPMs and bias circuitry; the remaining parts make up the FEB PCB, which includes signal conditioning, ADCs and readout logic. The Adapter and FEB PCBs are located at the detector, as a stack, and CAT6 cables are employed for serial interfaces. Key specifications are shown in figure 8.60. Prototypes of the Adapter and FEB

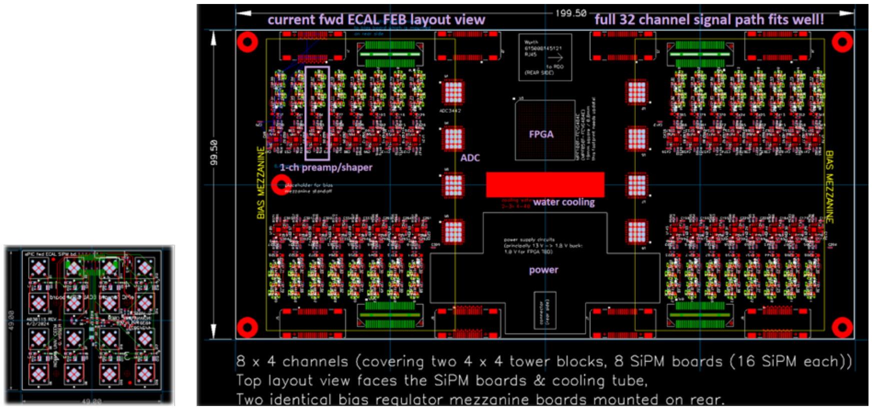

Figure 8.59: Discrete Adapter (left) and digitizer FEB PCBs

Function	Waveform digitizer with COTS devices
Channels	32
Digitizer	TI ADC 3422
Resolution	14-bit (12-bit also available)
Shaping	80 ns peaking time
FPGA	Microsemi MPF100T-FCVG484E Polarfire (Rad Hard)
Power	DC-DC converter (bPOL12V, bPOL48V, LTC36xx)
Cooling	Liquid
Cabling	CAT6

Figure 8.60: Discrete key specifications

PCBs are shown in figure 8.59.

CALOROC The CALOROC ASIC is currently under development to address readout from calorimeters with SiPMs and for which a 10-bit resolution digitization with wide dynamic range capabilities is applicable. The CALOROC design is based on the existing H2GCROC ASIC for SiPMs with similar frontend and a backend, or digital section with interfaces, conforming to the needs of the streaming readout approach at the EIC. In parallel, tests with the H2GCROCv3 chip continue to provide input and validation into the design of the CALOROC ASIC. There are, however, two frontend variants being considered: CALOROC1A uses an ADC, a TOA and a TOT for wide dynamic range, similar to the H2GCROC; CALOROC1B uses a different frontend architecture making use of dual gain switching techniques to extend its dynamic range. The CALOROC block diagram is shown in figure 8.61 and its specifications summarized in figure 8.62.

EICROC The EICROC ASIC is currently under development to address readout from AC-LGAD pixel detectors with low detector capacitance (Cdin) and very stringent timing precision requirements. The EICROC design is based on the existing HGCROC ASIC for Si and PMTs with similar frontend and a backend, or digital section with interfaces, conforming to the needs of the streaming readout approach at the EIC, which is already being designed for the CALOROC. Main IP blocks consist of preamp, discriminator, TOA, ADC and TDC. The EICROC block diagram is shown in figure 8.63 and its specifications are summarized in figure 8.65. Figure 8.64 shows the EICROC timing performance with varying charge from input signals.

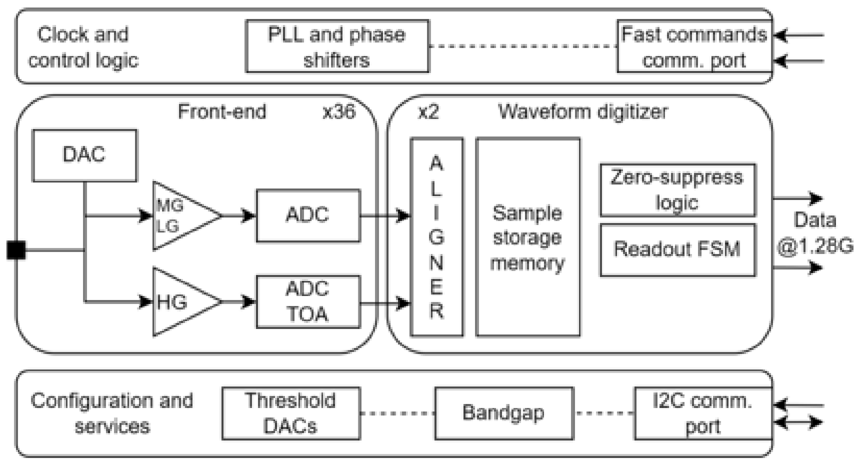

Figure 8.61: CALOROC block diagram

Function	Charge and timing digitization from SiPMs
Tech Node	130 nm CMOS
Channels	64
Cdin	500 pF – 10 nF
Digitization	Charge: 10-bit ADC, 15-bit TOT; Timing: <500 ps TOT (1 MIP)
Dynamic Range	Up to 12 nC
Clock	39.4 MHz operation from BX 98.5 MHz
Links	1260.8 Mbps @ 39.4 MHz, multiple
Power	10 mW/ch
Package	BGA
Rad Tolerance	Radiation hard

Figure 8.62: CALOROC Key Specifications

FCFD The FCFD ASIC is currently under development to address readout from AC-LGAD strip detectors with medium detector capacitance (Cdin) and very stringent timing precision requirements. The FCFD design implements the constant fraction discriminator technique for high precision timing without time-walk corrections. The backend, which is currently being considered, may be based on the existing ETROC ASIC or the EICROC development. The FCFD block diagram is shown in figure 8.66 and its specifications are summarized in figure 8.68. Figure 8.67 shows the FCFD timing performance with varying charge from input signals.

ALCOR The ALCOR ASIC is currently under development specifically for the readout of the dRICH detector with SiPMs due to its single photo-electron sensitivity requirement. The ALCOR design includes trans-impedance amplification (TIA) with regulated common gate (RCG) bias for low noise, inhibit or shutter operation to limit contribution from dark-rate SiPM noise and TDCs to allow for single-photon tagging or time and charge digitization. The shutter function is a critical aspect of this ASIC and it is programmable for width and latency. The ALCOR Die and block diagram are shown in figure 8.69 and its specifications are summarized in figure 8.70.

SALSA The SALSA chip is an ASIC currently under development, foreseen to do the readout of the different MPGD trackers, namely the barrel cylindrical Micromegas, the barrel RWELL and

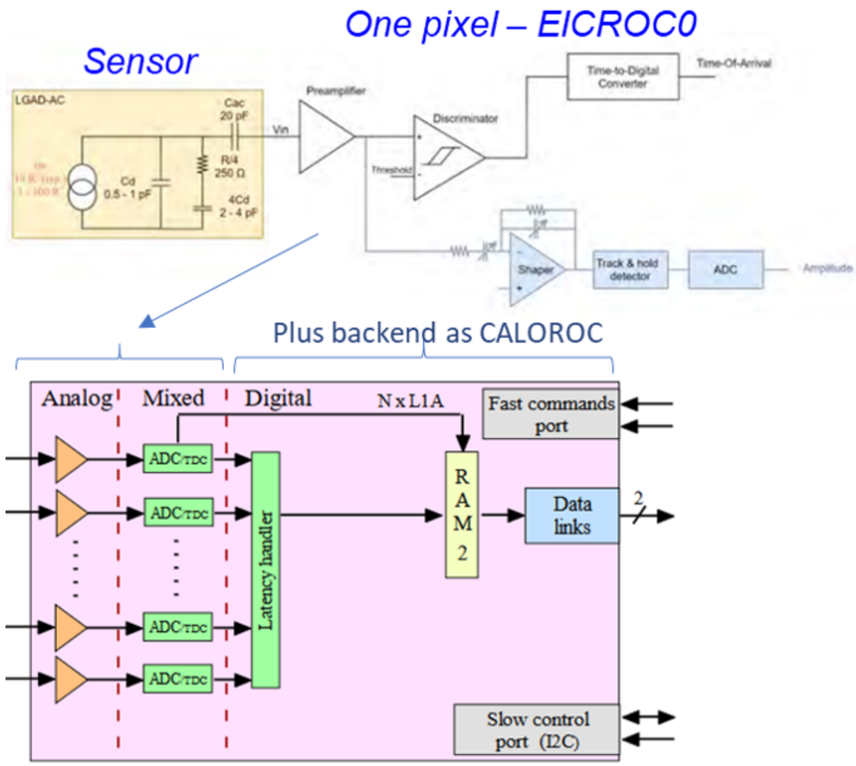

Figure 8.63: EICROC block diagram

the end-cap RWELL detectors. The purpose of SALSA is to amplify, shape and digitize signals coming from the MPGD detectors, and then perform basic data processing on the digitized samples before to transmit them to the next element of the data acquisition chain. It gathers in a single die a CSA pre-amplifier, a shaper and an ADC for each of the 64 channels, followed by a DSP which performs baseline corrections, digital shaping and a zero-suppression in order to reduce the output data bandwidth. Furthermore, to reduce data output even more, a peak finding algorithm is implemented to extract from samples information like amplitude and time of detected hits. It will be able to work both in the streaming readout environment foreseen at EPIC, and in a triggered environment.

The characteristics, performances and configurability of SALSA are designed to make the ASIC very versatile, being able to be adapted to several kinds of MPGD detectors and to several applications. It will be able to work with a large range of signal amplitudes, a large range of electrode capacitance and large range of signal rise times. Its target specifications are summarized in the Table 8.15.

Scope of the Effort The scope of the electronics and ASICs developments is summarized in figure 8.71, based on the number of readout channels, technologies employed and institutions developing these readout solutions.

It is noted that the pfRICH and the hpDIRC detectors benefit from the FCFD and the EICROC developments due to their timing precision requirements. The FCFD is, however, the nominal choice

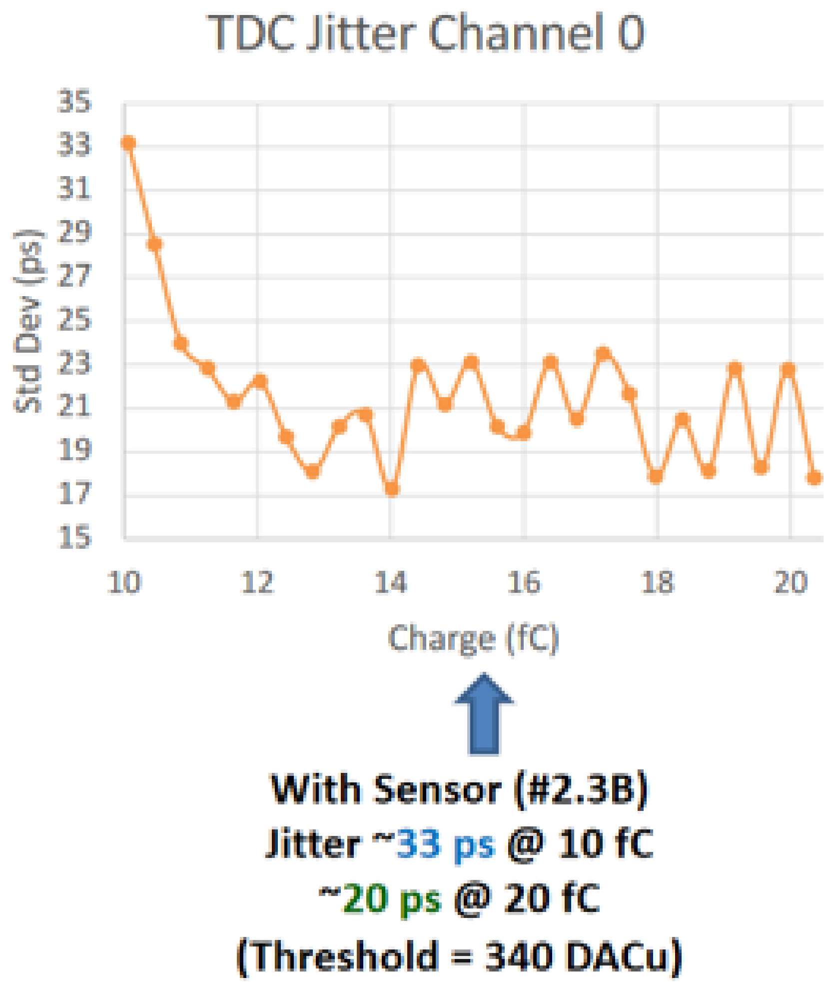

Figure 8.64: EICROC timing performance

Function	Timing digitization from AC-LGAD pixels
Tech Node	130 nm CMOS
Channels	1024 (32x32)
Cdin	1 – 5 pF
Digitization	ADC: 8-bit, TDC: 10b; Timing: 30 ps
Dynamic Range	1 – 50 fC
Clock	39.4 MHz operation from BX 98.5 MHz
Links	1260.8 Mbps @ 39.4 MHz, multiple
Power	<2 mW/ch
Package	Bump + wire bonds
Rad Tolerance	Radiation hard

Figure 8.65: EICROC Key Specifications

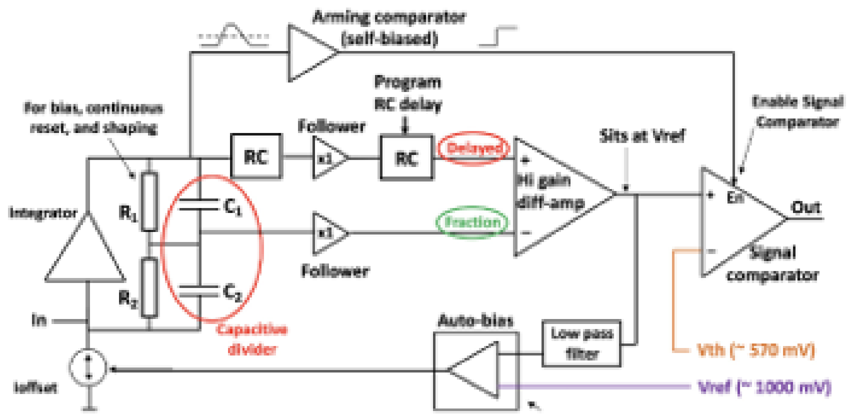

Figure 8.66: FCFD block diagram of the frontend

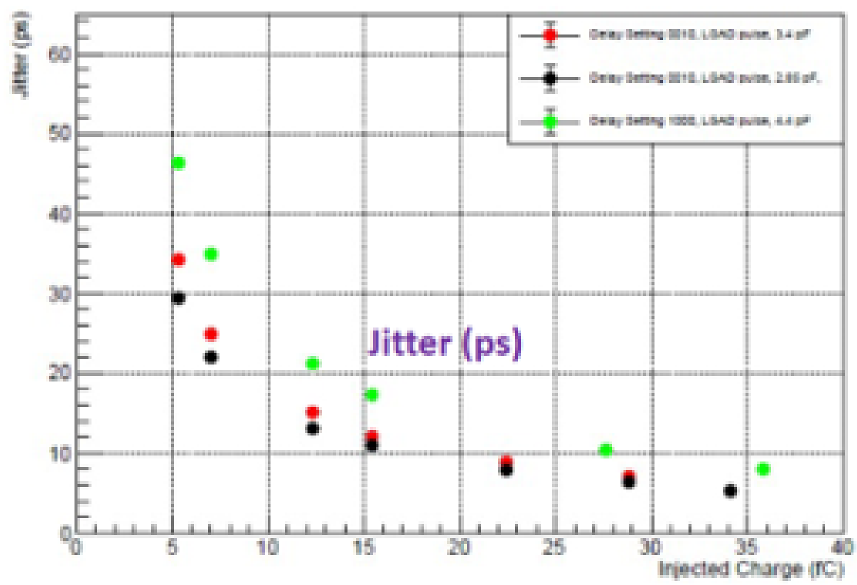

Figure 8.67: FCFD timing performance

Function	Timing digitization from AC-LGAD strips
Tech Node	65 nm CMOS
Channels	128
Cdin	<15 pF
Digitization	TBD; Timing: 10 - 30 ps
Dynamic Range	5 – 40 fC
Clock	39.4 MHz operation from BX 98.5 MHz
Links	1260.8 Mbps @ 39.4 MHz, multiple
Power	<2 mW/ch
Package	Bump + wire bonds
Rad Tolerance	Radiation hard

Figure 8.68: FCFD Key Specifications

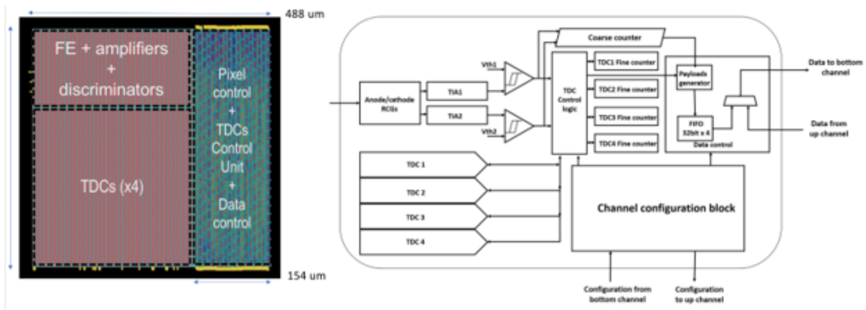

Figure 8.69: ALCOR Si Die (left) and block diagram

Function	Digitization from SiPMs with 1 p.e. sensitivity
Mode	Single-photon tagging or time and charge
Tech Node	110 nm CMOS
Channels	64 (8x8), dual polarity
Cdin	<1 nF
Digitization	25 ps TDCs, TOA + TOT; Timing <100 ps
Shutter	Width: 1 – 2 ns, programmable latency
Input Rate	<5 MHz
Clock	39.4 MHz operation from BX 98.5 MHz
Links	640 Mbps LVDS, SPI configuration
Power	12 mW/ch
Package	BGA
Rad Tolerance	Radiation hard

Figure 8.70: ALCOR Key Specifications

due to its lower channel density packaging for these applications with higher detector capacitances, which enable tailoring their timing performance via detector bias adjustment.

FEB components

DC/DC converters DC/DC converters are employed throughout ePIC for the efficient distribution and regulation of the various sub-systems. The bPOL12V and bPOL48V DC/DC modules are selected for their radiation hardness and high magnetic field tolerances. Designs based on the

	# Ch	# Ch/ Unit	#ASICs/ Wafer	#Wafers	Node (nm)	Package	Institution
Discrete/COTS	24 k	32	NA	740 Digitizers	COTS	NA	IU
CALOROC	97 k	64	480	5	130	BGA	OMEGA/IN2P3/IJCL/ORNL
EICROC	5.2 M	1024	160	42	130	Wafer Bump	OMEGA/IN2P3/IJCL/CEA-IRFU/AGH
FCFD	2.6 M	128	180	149	65	Wire Bond	FNAL
ALCOR	318 k	64	800	8	110	BGA	INFN
SALSA	202 k	64	500	9	65	BGA	CEA-Saclay/U of Sao Paulo

Figure 8.71: Scope of the electronics and ASICs developments

Specification	Values	Remarks
Number of channels	64	
Input capacitance	50-200 pF	Reasonable gain up to 1 nF
Peaking time range	50 - 500 ns	
Max gain range	50 fC to 5 pC	
Max input rate	100 kHz/channel	Fast CSA reset
Signal polarity	Negative and positive	
ADC max sampling rate	50 MS/s	
ADC dynamics	12 bits	More than 10 effective bits
DSP processing	Baseline correction, filter, zero-suppression, peak finding	
Readout modes	Streaming readout, triggered	
Output data links	4 Gigabit links	1 only used at EPIC
Die technology	TSMC 65nm	
Die size	$\sim$1 cm^2	
Power consumption	$\sim$ 15 mW/channel	
Radiation hardness	Up to 300 Mrad and 10^{13} n_{eq}/cm^2	

Table 8.15: Main specifications of the SALSA chip.

LTC36xx family of devices will also be employed after proper validation.

lpGBT The low power Giga-Bit Transceiver (lpGBT) chip will be extensively used in ePIC subsystems to provide aggregation and serial communications of up to 2.5 Gbps. The lpGBT is radiation hard with Serializer/Deserializer (SERDES) functionality.

VTRX+ The VTRX+ module is an electro-optical receiver/driver which will be extensively used in ePIC to interface to multi-mode optical fibers with MT optical connectors. One (1) receiver Rx (2.5 Gbps) and four (4) transmitters Tx (10 Gbps) are implemented. The VTRX+ is radiation hard and it is tolerant to high magnetic fields; it has a small footprint, has low power consumption and interfaces directly to the lpGBT transceiver devices.

RDOs The RDO aggregates ASIC information from the multiple front end boards. The RDO also has the function of delivering a high resolution clock ($<=$ 5ps jitter) to the front end boards. This clock is reconstructed from the data downlink fiber. The final function of the RDO is act as the interface between the detector specific function of the ASICS to the global ePIC DAQ fiber protocol. This protocol labels bunch crossings, organizes time frames, uses user defined fast commands to communicate with the ASICs and provides the capabilities for firmware triggering and flow control.

However, several detectors: the SVT, the MPGD based detectors, and all AC-LGAD based readouts will make use of lpGBT or lpGBT-like aggregation using VTRX+ transceivers. The lpGBT aggregates ASIC information, and deliverers a high resolution reconstructed clock. However, it attempts to give a transparent interface to the ASICs. It does not have the capability of implementing the

Target Detector	**Input**	**Output**	technology
TOF Pre-Prototype, Calorimeters	copper	SFP+ fiber	FPGA
dRICH	copper	VTRX+ fiber	FPGA
SVT, MPGD, AC-LGAD second level	fiber	fiber	FPGA
AC-LGAD	copper	VTRX+ fiber	lpGBT
Imaging Calorimeter (Astropix)	copper	fiber	FPGA
Low Q^2 Tagger (Spyder3 Board)	copper	up to 12 fiber	FPGA
Direct Photon Detector	copper	fiber	flash

Table 8.16: Types of RDO

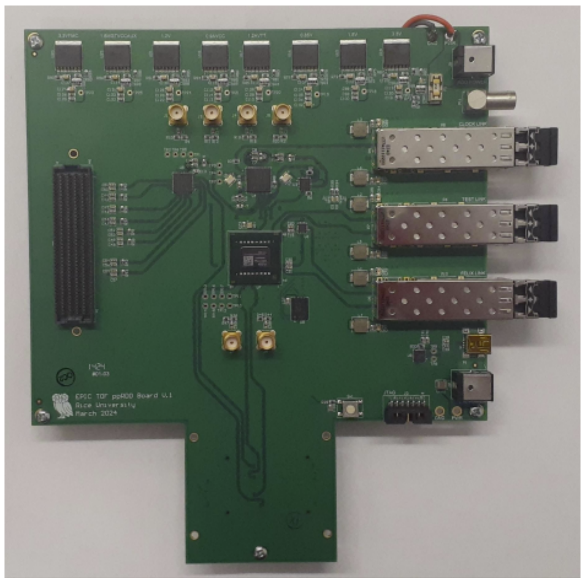

Figure 8.72: TOF pre-protype RDO

full ePIC protocol. For these RDOs the protocol will be implemented at the next level, either inside the DAM board or in a second level fiber to fiber RDO.

There will be several versions of the RDO depending on the needs of the specific detectors. The different RDO types are summarized in table 8.16

TOF pre-prototype RDO (FPGA based copper to SFP+ The TOF pre-prototype RDO was designed to use elements common to most ePIC detector RDOs. These elements include Xilinx Artix+ FPGA, SFP+ fiber optics interface, clock cleaner PLLs, and clock recovery. The pre-prototype has been produced and is undergoing measurements of power usage and clock jitter. The board is shown in figure 8.72.

dRICH RDO The dRICH RDO is part of the dRICH Photo Detector Unit PDU (see section **??**, 1248 PDUs will serve the dRICH). It provides read-out of four 64-channel ALCOR ASIC, installed each on a separate FEB. The space constraints are particularly demanding: the total RDO area is 40x90 mm^2 - quite similar to a credit card - requiring a devoted design, given the high integration

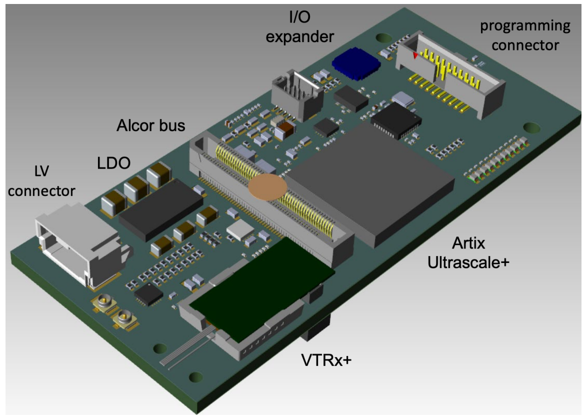

Figure 8.73: 3D model of dRICH RDO

of data buses and services within the PDU. The FPGA providing readout of the ALCOR is an AMD Artix Ultrascale+ AU15P-SBVB484, complemented by a PolarFire FLASH-based FPGA MPF050T-FCSG325. The latter will support remote programming and continuous scrubbing of configuration bits of the SRAM-based AMD FPGA, to protect against SEU. Given the space constraints and the need to curb power consumption (total RDO power is expected ≈ 4 W) the CERN-developed VTRX+ optical transceiver has been selected, directly connected to the AMD FPGA SERDES. The maximum throughput per link (reached at maximum radiation damage before annealing) is foreseen not exceeding 2 Gbps, safely within VTRX+ specifications The ALCOR will be read out at 394 MHz, with a clock multiplier and jitter-attenuator (Skyworks Si5326) deriving this clock from the reconstructed EIC clock. A Microchip microcontroller provides power management and acts as watchdog against SEL. The first prototype of this card is under production and will be intensively tested during 2025, including irradiation tests. A 3D-rendering of the card is shown in Fig. 8.73.

Fiber to Fiber RDO The fiber to fiber RDO is to be used with lpGBT-like FEBs to convert the transparent ASIC interface to the ePIC DAQ protocol. They are also necessary to further aggregate the fibers, particularly in the case of SVT and bTOF large numbers of low-data utilization fibers are required.

lpGBT based copper to fiber RDO This RDO is yet to be designed, but is required for the lpGBT based readout of the inner detectors.

Astropix End of Stave Card (RDO) This RDO is to be developed by NASA for use with the Astropix sensors.

Low Q^2 RDO This is a RDO specifically for the low Q^2 taggers. It is expected to be an updated version of the Spyder3 board. These use the timepix sensor and have high potential data volumes, requiring several uplink fibers per RDO.

Flash based RDO The Flash RDO is a specialized interface for the Direct Photon Detector. This detector has only about 100 channels, but is expected to have very high occupancy, and as such the appropriate technology is to digitize all data at 200MHz and stream it directly to the DAM boards which will summarize the information, writing out only the summed energy deposited each bunch crossing, or histograms of the bunch crossing energies according to bunch number.

DAM - Data Aggregation and Manipulation Hardware For the ePIC DAQ system the DAM boards will be used as the primary aggregation point for the “raw” detector data streams. Because these boards are also the final aggregation points for the front-end (hardware managed) DAQ, there will need to be some well-defined but configurable algorithms for merging streams and managing potential congestion and data loss both for the incoming detector streams and the outgoing aggregated streams being queued up for online processing.

In Addition, the DAM boards will interface with the Global Timing Unit (GTU) hardware via a proprietary communication protocol that supports a synchronized EIC clock distribution to all subsystems and general DAQ/Run control and configuration. Finally, the DAM will act as the slow control interface for configuration and monitoring of all detector subsystem front-end boards (e.g. ASICs and other digitizing electronics).

We have identified an ideal candidate for the DAM hardware. An updated version of the FELIX board (Model FLX155) is currently being produced at BNL for ATLAS at the HL-LHC. Its features are substantial and the updated components ensure a longevity of production, performance and support that match very well with the EIC timeline. The board is built around the new Xilinx Versal FPGA/SoC family. This will facilitate using the board both as a PCIe device (supporting both PCIe Gen4 and Gen5 standards) in a server or as a standalone “smart” “aggregation” switch running a Linux OS. It can support up to 48 serial links to RDOs at the front-end running at speeds up to 25Gbps as well as an LTI interface (8 fibers) supporting a high-resolution direct clock along with our GTU-DAM communication protocol. There is also a separate 100Gb ethernet link off the board. A DDR4 RAM slot is available to support buffering and more complex algorithms for data reduction or interaction tagging. The board supports JTAG and I2C communications.

We expect to procure several FLX155 boards for testing and software/firmware development in 2025.

GTU - Global Timing Unit The design of the global timing distribution system (GTU) will be central to the operation of the streaming readout model. The timing system must provide signals to ensure that the data from different detectors can be synchronously aggregated. It must provide a copy of the accelerator bunch crossing clock (running at 98.5Mhz) to all front-end systems. A subset of these systems (e.g. TOF) will require a phase aligned system clock with a jitter of < 5ps in order realize required timing resolutions for these detectors (20-30ps).

The GTU is also the only source of real time information provided to the FEB/RDOs, so it must provide information a trigger system would normally provide. These functions include the ability to synchronize data from different detectors, to send flow control signals, to pass bunch information such as spin orientations and bunch structure, the ability to provide user defined signals for signaling special data formatting or calibration needs, and the ability to implement a hardware trigger for debugging, calibration or as a fallback option to solve unforeseen readout issues. It will also need to track potential phase changes of the beam relative to the accelerator clock due to the transitive loading specific to the EIC acceleration scheme.

Figure 8.74 shows a schematic layout based on required functionality of the GTU. The physical concept is shown in figure 8.75. In general the GTU will be custom rack-mounted hardware in the DAQ room. It will be based on a multi-FPGA architecture including a single Zync SoC FPGA supporting

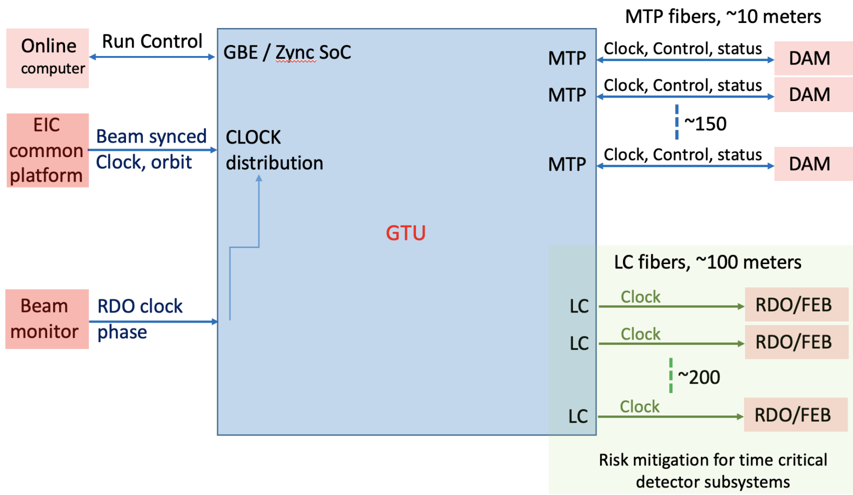

Figure 8.74: Schematic layout based for the GTU

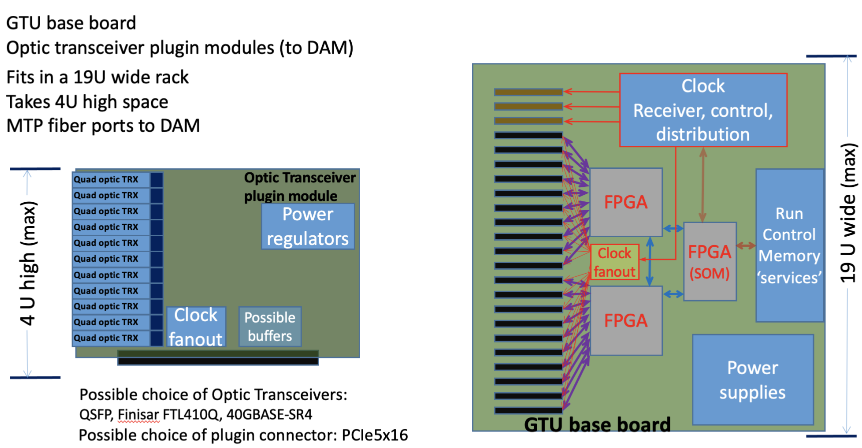

Figure 8.75: Physical concept for the fiber distribution for the GTU

gigabit ethernet and a full Linux OS to facilitate both ePIC Run Control and other user-based applications. It will include an interface for the EIC Common platform (Clock, beam orbit and other collider information) and an interface for feedback from the local IP-6 beamline to support bunch crossing clock phase corrections

The jitter-cleaned and phase corrected clock then is fanned out for distribution to all DAM boards via a multi-fiber communications link (We intend to support up to 150 of these links for current needs as well as potential future requirements). In addition we plan to support up to 250 direct clock links to the RDO/FEB electronics. This is to mitigate potential limitations with the distribution of the low jitter (< 5ps) clock via the DAM path communication protocol.

Protocols The ePIC fiber protocol is used to communicate information between the GTU, DAM and RDO boards. The DAM to RDO communications are limited by the type of interface, and can be described in three categories as shown in table 8.18.

DarkGray	Decoded Synchronous Command Structure							
Gray	[0:7]	[8:15]	[16:23]	[24:31]	[32:39]	[40:47]	[48:55]	[56:64]
Gray	Flexible Command Data Encoding	FAST CMD	Comma					
type		type specific			FAST CMD	Comma		

Table 8.17: DAM/RDO Decoded Synchronous Command Structure. This structure is defined to allow continuous availability of the critical beam related bits and more rare commands. The data in the 40 bits worth of flexible command data encoding remains flexible but must contain enough control bits to select what structure it has. The ”type”, ”type specific” division is an potential holding this flexibility

type	**clock (MHz)**	**downlink rate (Gb/s)**	**downlink word length** (ns)	**downline word width** (bits)
FPGA Standard	98.5	10	10.15	64
FPGA VTRX+	98.5	2.56	10.15	16
lpGBT VTRX+	39.4	2.56	25.375	64

Table 8.18: RDO downlink words

The ePIC fiber protocol depends upon a synchronous command structure (table 8.17 which simultaneously encodes fast commands, to be delivered to the RDO or ASICs with fixed latency relative to the bunch crossing and control information such as the current bunch crossing. The RDO acts upon delivered synchronous commands to provide headers defining the time frames, and to implement required features. The lpGBT provides a transparent fiber interface to the ASICs and does not have features capable of implementing the full ePIC DAQ protocol, so this functionality must be provided later in the chain, either in a second layer fiber to fiber RDO, or in the DAM board itself.

The maximum timeframe length, in bunch crossings will be defined to fit within $2^1$6, which implies a time frame length of $\approx$ 0.6ms. This is also a convenient time as it corresponds to a manageable maximum time frame size of $\approx$ 10MB. The need to support both the 10.15ns EIC clock and the synchronized 25.375ns clock support by cern lpGBT and CERN developed asics demands that time frame lengths be limited to multiples of 5 EIC clocks, if the time frame’s are to be synchronized in time.

The features encoded in the Synchronous command protocol are

1. Synchronize bunch counters among all detector readouts
2. Define the time frame boundaries
3. Provide RDO and DAM Data processing flags
4. Configure ASICs and RDOs
5. Firmware based triggering
6. Flow control
7. Transfer Data
8. Transfer Slow Controls Data

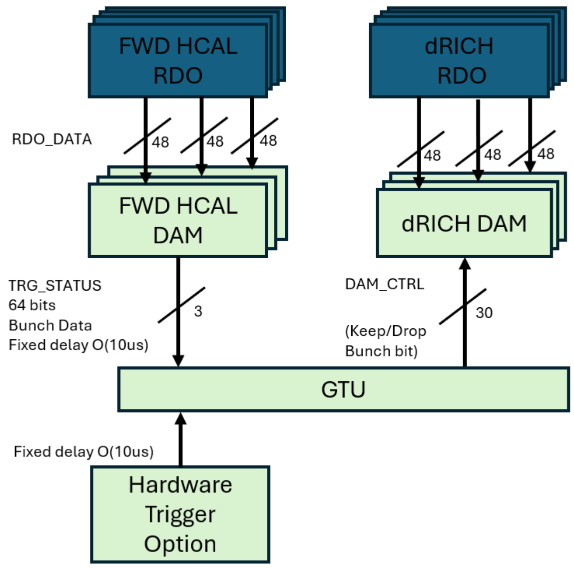

Figure 8.76: Operation of firmware trigger under assumption that the trigger decision for the dRICH depends upon data from fHCAL

Firmware Trigger One example of the operation of the protocol is in the firmware trigger to be implemented to reduce dRICH noise. It's important to note that the the firmware trigger under discussion is not (or not necessarily) a global trigger that would remove full events from the readout of the ePIC detector. Instead, this trigger is expected to affect only the data from particular detectors with unusually high data volumes. In this example, the dRICH.

The path of the commands sent is show in figure 8.76. Data arrives at DAM boards with 10us from digitization. It is stored in the DAM boards. After 10us FPGA based algorithms provide a description of the data (for example number of hits above a specified threshold) from each fHCAL DAM board. This information is encoded into 64 bits and sent to the GTU which aggregates data from fHCAL DAM boards and sends the keep/drop bunch bit to the dRICH DAM boards. The dRICH DAM boards drop or transmit data based upon this message. The decision comes after a fixed latency of about 11us which is very small compared to the buffering available on the DAM board.

Note that a similar approach can be implemented with a hardware signal into the GTU. In this case a fixed delay is applied to the hardware signal, but the decision mechanism uses the same data path.

dRICH Internal trigger There is also another scheme for implementing a dRICH trigger using only dRICH data under investigation by the dRICH group **??**. In this scheme, 8 of the data ports are dedicated to connect a second layer of DAM boards which implement a multi FPGA ML algorithm with deterministic time. The results of this calculation are transmitted to the GTU in the same manner as in the previous firmware trigger.

DAQ/Online Computing - Echelon 0 Table 8.19 outlines the planned resources for the ePIC detector DAQ and Online computing needs. This is based on the elements shown in the DAQ

Resource	Totals
DAM/FELIX boards	136
EBDC Servers	92
DAQ Compute Nodes	108
File Servers (Buffer Box)	6

Table 8.19: DAQ Computing Resources

schematic in Figure 8.55. Several thousand fibers from the RDOs will be aggregated in the DAM boards and presented to the Online Farm. To be clear each online farm node represents one multi-core server. The expectation is that they will minimally support 32-64 cores, and selected nodes will support PCIe-based GPUs and/or FPGAs in addition to the DAM boards in the FBDC (Frame Building Data Concentrator) nodes. The high performance DAQ network is expected to support 100/400Gbps bandwidth connections. As the majority of the Online computing is expected to be COTS hardware, much of it will be acquired as late as is reasonable in the construction phase.

All Echelon 0 resources are fully dedicated to operation of the ePIC Detector and are included as part of the EIC Project. One open question under consideration, however, is to split these resources between the DAQ Room at IP-6 and the SDCC (BNL main data center) and to integrate them as a single enclave under ePIC control. There are several advantages to this configuration. First it will reduce the overall cost of infrastructure upgrades to the DAQ Room cooling systems. Also, having a subset of ePIC computing resources available in the SDCC will allow better network access to DAQ and electronics labs during construction (when the DAQ Room will not be available. Finally, during operations having DAQ tiered storage of production data in the SDCC will facilitate distribution of that data to both Echelon 1 processing sites (BNL and JLAB).

At the DAM stage the aggregated data streams will have substantial buffering and available network bandwidth for online processing that will be primarily focused on event identification and background/noise reduction. While we do not currently have solid estimates on the necessary computing resources to complete the required tasks, we have tried to provide conservative estimates of computing resources that would allow a full reconstruction of a 500kHz trigger rate of events from similar scale detectors that exist now (e.g. GlueX and CLAS12 at Jefferson Lab and sPHENIX at RHIC). More likely the necessary computing resources for online filtering to get the expected data rates of O(100Gbps) to files will be somewhat smaller.

Time Frame Building In the streaming model, the primary consideration is ensuring that enough bandwidth and buffering will be available to handle the digitized data at each stage of the DAQ. At the front-end stage time frames for the individual streams are created, managed and aggregated. Given current background and noise estimates the planned bandwidth off the detector to the DAM boards O(10Tbps) should be more than sufficient.

Streams at the DAM boards will support time frames using a 16 bit bunch crossing counter which would represent a configurable time window of up to 65536*10.15ns = 665µs. Although the front-end DAQ will be synchronized using a single common clock from the EIC, not all ASICS/digitizers at the FEBs will be running at the same frequency. Hence the timestamps coming from hits in different detectors will need to be wrapped in smaller "time slices" within the full time frame to establish an absolute time for each hit.

Time frames buffered at the DAM boards will be able to utilize the online farm to complete a full build of complete time frames with data from all detectors. Effectively N streams from the DAM boards will generate M<N streams of time frames containing the time frame fragments from the N original streams. This will greatly facilitate additional event identification and processing at both the Echelon 0 and Echelon 1 stages.

Data Processing The ePIC readout system must support data reduction techniques. The implementation of firmware based triggering has already been described, but there are many additional techniques that might be implemented in echelon 0. These include zero loss techniques like aggregation of headers from ASICs or DAM board data. It could include standard or ML based compression techniques. It could involve analysis techniques such as cluster finding or track reconstruction. There could also be ML based noise reduction techniques. And there could be analysis done for specific purposes such as the creation of scalers for monitoring or collider feedback.

The framework for the code generating these features must allow the code to be shared with the offline software, for operational transparency, and for algorithm evaluation.

The results of the code must be incorporated into the time frame data using data formats that allow for independent data banks to co-exist. The policy of ePIC is expected to be to avoid dropping any data unless data volumes make it necessary. There should also be a sample of unprocessed data even if the readout of raw data banks are suppressed due to data volume limits. This implies that the write out of specific data banks be controlled by configurable prescales.

Configuration Databases Configuration information must be stored and made accessible to the ePIC Collaboration.

Slow controls interface to RDOs/FEBs The primary configuration and slow control communications interface to all the ASICs and other digitizing electronics (FEBs) will be through our proprietary data link between the DAM board and the RDOs. Our current plan is to take advantage of the Versal SoC FPGA dual-core ARM CorteX processor. ALL DAM boards will support a full LinuxOS and gigabit ethernet access. This will facilitate running an EPICS soft IOC as well as user-based server applications for local and remote communication with the front-end electronics.

Slow control communication on the DAM-RDO link must be bidirectional which means that slow control communications must share the link with streaming data coming from the detectors. Nominally, we will be providing more than adequate bandwidth to support this slow control piece even if the stream is active, but provisions will be made to ensure that stream time frames will take priority.

Software and firmware development of drivers and libraries necessary to access all the FEB ”flavors” is supported as part of the Project. The majority of the FEBs will support standard I2C control communications.

Monitoring / Logging A unified system for centralized logging of informational and error messages is required. These messages should be ideally be available and archived in web-accessible form.

A unified system for monitoring of the real time behaviour and utilization of online components is also needed.

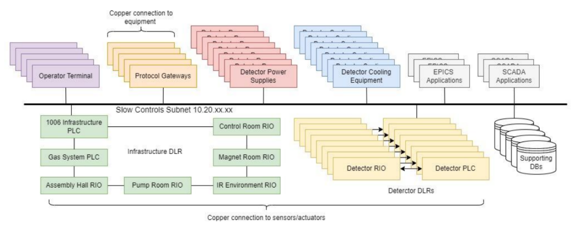

Figure 8.77: Proposed ePIC slow controls network topology

Scenario	Yearly Database Storage (TB)	Network Traffic (Mbps)
estimated	53.9	22.8
worst case	173.5	73.4

Table 8.20: Slow Controls data volume and network traffic

Interface to Echelon 1 As discussed in Section X (computing), the ePIC DAQ (Echelon 0) is an integral part of the computing system, and the output of the DAQ data triggers the calibration and reconstruction pipeline in Echelon 1, located at the computing centers of the host labs. From the DAQ buffering disks, two identical copies will be sent to the buffer file system at the BNL SDCC via a dedicated fiber link and at the JLab Data Center via the 400Gbps ESnet link, respectively. Each data center's data buffer has the capability of about three weeks' ePIC data taking to allow for multiple iterations of calibration jobs and reconstruction passes. Data will also be copied to permanent archival storage (presumably HPSS-like tape system), one copy at each site, which allows for reprocessing of the data in the future in case a problem identified in the prompt reconstruction pass or an improved reconstruction becomes available in the future. Nevertheless, in a steady state, the prompt calibration and production are expected to make the final analysis-ready data for physics working groups within days of the data taking, significantly expedited compared to many ongoing Nuclear Physics experiments.

Slow Controls There will be a myriad of slow controls information associated with both the EIC collider and the ePIC detector. These include various systems associated with the beamline, magnets, detector biases, gas flows, temperatures, pressures, etc... While the design and implementation of these slow control systems will be driven by the relevant subsystems they are associated with, it is the defined responsibility of the DAQ to provide software tools to facilitate the integration of all this information with the streaming physics data. This will include synchronizing the times associated with readout of slow control systems and the bunch-crossing clock that will be driving the DAQ system. Online slow control databases to support calibration and reconstruction processing will also be developed. Finally, a general network infrastructure in the experimental hall and control room, independent of the high performance DAQ network, will be provided to support integration of all slow control systems

A schematic of the proposed slow controls network topology is shown in figure 8.77. The implementation uses EPICS 7 on an ethernet network to control detector operation and read and archive conditions information. Allen-Bradley PLCs are to be used for controlling power to racks in the IR and for detector interlocks.

Resource requirements for the slow controls system were obtained by surveying detector managers. These resulted in approximately 500,000 channels to be read and stored. The yearly storage estimates and network traffic estimates are show in table 8.20.

Figure 8.78: DAQ/Computing schedule

Implementation

Calibration, alignment and monitoring: During run time, predetermined calibration and alignment will be used in configuring the readout electronics and data reduction computing tasks. These calibration and alignment are managed by detector groups, extracted from dedicated prior-to-beam calibration runs, such as pedestal runs and zero field runs. When necessary, such as changes in detector condition, new calibration will be extracted and updated to be used in data taking. The calibration constant used will be archived in the run database and made available for reference in the offline analysis.

Constant monitoring for detector status and data pipeline healthiness is key to high-efficiency data taking and a successful run. We expect a multi-level of monitoring that includes monitoring the metrics on (1) detector statues (2) each stage of the data pipeline (3) sampled data content for decoding and analysis. In addition, in the Echelon-1 computing facility, full reconstruction will be performed for a small fraction of time frames expediently to provide holistic feedback of the experiment capability down to analysis level observable such as pi0 and K0s.

Status and remaining design effort:

R&D effort: ASIC R&D to continue through 2025

E&D status and outlook: The bulk of the engineering design efforts still required for the readout electronics are centered around the development of RDO and FEB designs needed to support all the detector subsystems. This information is needed to establish baseline costs and better define construction and testing schedules. Project Engineering design for a GTU engineering article can be completed prior to CD2/3. Finally, we expect to procure several FLX155 engineering articles in 2025 to support further timing and communication protocol testing and initial firmware development.

Status of maturity of the subsystem: Electronics and DAQ held a second PDR in June 2024. We expect to hold a third PDR in 2025 on track to an FDR in 2026. There are CD-3B items in the Electronics for VTRX+ and lpGBT. The FDR was held in June 2024, and will be presented during the CD-3B review in January 2025.

Environmental, Safety and Health (ES&H) aspects and Quality Assessment (QA planning:

Construction and assembly planning: Figure 8.78 shows the current project schedule for DAQ/Computing. It is broken down into four general categories: Design/Procurement, Fabricate and Delivery, Test and Accept and Installation. Early in the construction phase there is a heavy focus on building and testing custom hardware (GTU, DAMs, RDOs) in order to facilitate detector subsystem testing and DAQ firmware/software development. This will take place primarily in several DAQ/Electronics labs at BNL in the Physics building.

Once IP-6 infrastucture upgrades have been completed (DAQ and Control rooms, Wide Angle Hall), we can begin the main trunk fiber pulls into the hall and tunnels and install required patch panels and terminate fibers. At this time we can also start installation of the general IP-6 network infrastructure in the Hall, DAQ and Control Rooms.

Computing hardware procurement and installation are scheduled in three phases during the course of construction. Phase I at the beginning of construction will be for a small subset of machines for development and evaluation. They will be placed in both the DAQ/Electroncs development labs as well as in the SDCC. Phase II will be primarily in the DAQ Room as part of the DAQ subsystem installations and will provide the opportunity for full chain large scale testing of the DAQ as well as for detector subsystems as they begin to be installed at IP-6. Finally Phase III will be implemented at the end of the full ePIC detector installation as we have a better understanding of the required resources needed for inital Physics operation. This hardware will be installed at both the DAQ Room and in the SDCC which will define the full Echelon 0 enclave.

Collaborators and their role, resources and workforce: The institutions specifically developing the readout electronics and ASICs are listed under the electronics section. Figure 8.79 lists the institutions which have expressed interest in participating in the design of various other parts of the readout chain. Formal agreements committing engineering and technical personnel have not been officiated.

8.3.11 Software and Computing

Requirements

Requirements from physics: Add text here.

Requirements from Radiation Hardness: Add text here.

Requirements from Data Rates: Add text here.

Justification

Device concept and technological choice: Add text here.

Subsystem description:

General device description: Add text here.

Sensors: Add text here.

FEE: Add text here.

Detector System		Channels	SensorTechnology	Redout Technology	Institution
Si Tracking					
	3 vertex layers	7 m^2	MAPS	lpGBT, VTRX+	STFC, UK, ORNL
	2 sagitta layers	368 pixels	MAPS	lpGBT, VTRX+	STFC, UK, ORNL
	5 backward disks	5,200 MAPS sensors	MAPS	lpGBT, VTRX+	STFC, UK, ORNL
	5 forward disks		MAPS	lpGBT, VTRX+	STFC, UK, ORNL
MPGD Tracking					
	Barrel, e & H Endcaps	202 k	uRWELL, MicroMegas	SALSA	CEA, OMEGA, JLab
Forward Calorimeters					
	LFHCAL	63,280	SiPM	CALOROC	ORNL, Debrecen
	HCAL Insert	8 k	SiPM	CALOROC	ORNL, Debrecen
	pECAL W/SciFi	16,000	SiPM	Discrete	IU
Barrel Calorimeters					
	HCAL	7,680	SiPM	CALOROC	ORNL, Debrecen
	ECAL SciFi/Pb	5,760	SiPM	CALOROC	U Regina, ORNL
	ECAL Imaging Si ASTROPIX	500 M pixels	Astropix	Astropix	KIT,NASA (GSFC), ANL
Backward Calorimeters					
	nHCAL	3,256	SiPM	CALOROC	ORNL
	ECAL (PWO)	2,852	SiPM	Discrete	IU, EEEMCAL Consortium
Far Forward					
	B0: 3 Crystal Calorimeter	135	SiPM/APD	Discrete	IU, JLab
	B0: 4 AC-LGAD layers	688,128	AC-LGAD Pixel	EICROC	IJCLab, OMEGA, BNL, ORNL, Rice
	2 Roman Pots (RP)	524,288	AC-LGAD Pixel	EICROC	IJCLab, OMEGA, BNL, ORNL, Rice
	2 Off Momentum (OMD)	294,912	AC-LGAD Pixel	EICROC	IJCLab, OMEGA, BNL, ORNL, Rice
	ZDC: Crystal Calorimeter	900	SiPM/APD	Discrete	IU, JLab
	ZDC: HCAL	9,216	SiPM	CALOROC	ORNL, Debrecen, JLab
Far Backward					
	Low Q Tagger 1	33,030,144	Timepix4	Timepix4	U. Glasgow
	Low Q Tagger 2	33,030,144	Timepix4	Timepix4	U. Glasgow
	Low Q Tagger 1+2 Cal	420 (2x210)	SiPM	CALOROC	U. York
	2 Lumi PS Calorimeter	3,360 (2x1680)	SiPM	Discrete	U. York
	2 Lumi PS Tracker	128,000 (2x64,000)	AC-LGAD Strip	FCFD/EICROCx	FNAL, OMEGA, Hiroshima, NTU, ORNL, UIC, UH, Rice, KSU, Tokyo
	Lumi Direct Photon Calorimeter	100	SiPM	Flash250	AGH Krakow, JLab
PID-TOF					
	Barrel bTOF	2,359,296	AC-LGAD Strip	FCFD/EICROCx	FNAL, OMEGA, Hiroshima, NTU, ORNL, UIC, Rice, BNL, KSU, Tokyo
	Hadron Endcap fTOF	3,719,168	AC-LGAD Pixel	EICROC	IJCLab, OMEGA, BNL, ORNL, Rice
PID-Cherenkov					
	dRICH	317,952	SiPM	ALCOR, VTRX+	INFN (BO, FE, TO)
	pfRICH	69,632	HRPPD	FCFD/EICROCx	BNL, FNAL, JLab
	hpDIRC	73,728	MCP-PMT or HRPPD	FCFD/EICROCx	BNL, FNAL, JLab

Figure 8.79: Electronics and DAQ Resources

Other components: Add text here.

Performance

Implementation

Services: Add text here.

Subsystem mechanics and integration: Add text here.

Calibration, alignment and monitoring: Add text here.

Status and remaining design effort:

R&D effort: Add text here.

E&D status and outlook: Add text here.

Other activity needed for the design completion: Add text here.

Status of maturity of the subsystem: Add text here.

Environmental, Safety and Health (ES&H) aspects and Quality Assessment (QA planning: Add text here.

Construction and assembly planning: Add text here.

Collaborators and their role, resources and workforce: Add text here.

Risks and mitigation strategy: Add text here.

Additional Material Add text here.

8.4 Detector Integration

Add text here.

8.4.1 Installation and Maintenance

Add text here.

8.5 Detector Commissioning and Pre-Operations

Add text here.

References

[1] Irene Dutta and Christopher Madrid and Ryan Heller and Shirsendu Nanda and Danush Shekar and Claudio San Martín and Matías Barría and Artur Apresyan and Zhenyu Ye and William K. Brooks and Wei Chen and Gabriele D'Amen and Gabriele Giacomini and Alessandro Tricoli and Aram Hayrapetyan and Hakseong Lee and Ohannes Kamer Köseyan and Sergey Los and Koji Nakamura and Sayuka Kita and Tomoka Imamura and Cristían Peña and Si Xie, "Results for pixel and strip centimeter-scale AC-LGAD sensors with a 120 GeV proton beam," 7 2024.

[2] R. Abdul Khalek *et al.*, "Science Requirements and Detector Concepts for the Electron-Ion Collider: EIC Yellow Report," *Nucl. Phys. A*, vol. 1026, p. 122447, 2022.

[3] "The electron-ion collider user group.".

[4] R. A. Khalek *et al.*, "Science Requirements and Detector Concepts for the Electron-Ion Collider: EIC Yellow Report," *Nucl. Instr. and Meth. A*, vol. 1026, p. 122447, 2022.

[5] "The epic collaboration website.".

[6] "Technical Design Report: A High-Granularity Timing Detector for the ATLAS Phase-II Upgrade," tech. rep., CERN, Geneva, 2020.

[7] C. Madrid, R. Heller, C. San Martín, S. Nanda, A. Apresyan, W. Brooks, W. Chen, G. Giacomini, O. Kamer Köseyan, S. Los, C. Peña, R. Rios, A. Tricoli, S. Xie, and Z. Ye, "First survey of centimeter-scale ac-lgad strip sensors with a 120 gev proton beam," *Journal of Instrumentation*, vol. 18, p. P06013, June 2023.

[8] C. Bishop, A. Das, J. Ding, M. Gignac, F. Martinez-McKinney, S. Mazza, A. Molnar, N. Nagel, M. Nizam, J. Ott, H.-W. Sadrozinski, B. Schumm, A. Seiden, T. Shin, A. Summerell, M. Wilder, and Y. Zhao, "Long-distance signal propagation in ac-lgad," *Nuclear Instruments and Methods in Physics Research Section A: Accelerators, Spectrometers, Detectors and Associated Equipment*, vol. 1064, p. 169478, 2024.

[9] L. Menzio *et al.*, "First test beam measurement of the 4D resolution of an RSD pixel matrix connected to a FAST2 ASIC," *Nucl. Instrum. Meth. A*, vol. 1065, p. 169526, 2024.

[10] S. Xie, A. Apresyan, R. Heller, C. Madrid, I. Dutta, A. Hayrapetyan, S. Los, C. Peña, and T. Zimmerman, "Design and performance of the fermilab constant fraction discriminator asic," *Nuclear Instruments and Methods in Physics Research Section A: Accelerators, Spectrometers, Detectors and Associated Equipment*, vol. 1056, p. 168655, 2023.

[11] C. Chock, K. Flood, L. Macchiarulo, F. Martinez-Mckinney, A. Martinez-Rojas, S. Mazza, I. Mostafanezhad, M. Nizam, J. Ott, R. Perron, E. Ryan, H.-W. Sadrozinski, B. Schumm, A. Seiden, K. Shin, M. Tarka, D. Uehara, M. Wilder, and Y. Zhao, "First test results of the transimpedance amplifier stage of the ultra-fast hpsoc asic," *Journal of Instrumentation*, vol. 18, p. C02016, feb 2023.

[12] O. H. W. Siegmund *et al.*, "Advances in microchannel plates and photocathodes for ultraviolet photon counting detectors," *Society of Photo-Optical Instrumentation Engineers Proceedings*, vol. 81450J.

[13] C. J. Hamel *et al.*, "LAPPD and HRPPD: Upcoming Upgrades to Incom's Fast Photosensors,"

[14] "EICROC ASIC." `https://indico.bnl.gov/event/18539/contributions/73731/attachments/46348/78403/CdLT_EICROC_6mar23.pdf`.

[15] "Organization for Micro-Electronics desiGn and Applications." `https://portail.polytechnique.edu/omega/`.

[16] J. Anderson *et al.*, "FELIX: a PCIe based high-throughput approach for interfacing front-end and trigger electronics in the ATLAS Upgrade framework," *JINST*, vol. 11, no. 12, p. C12023, 2016.

[17] "Chiba Aerogel Factory Co., Ltd.." `https://www.aerogel-factory.jp/`.

[18] M. Yonenaga *et al.*, "Performance evaluation of the aerogel RICH counter for the Belle II spectrometer using early beam collision data," *Prog. Theor. Exp. Phys.*, no. 093H01, 2020.

[19] Y. Suda *et al.*, "Performance evaluation of the high-voltage CMOS active pixel sensor AstroPix for gamma-ray space telescopes," *Nucl. Instrum. Meth. A*, vol. 1068, p. 169762, 2024.

[20] A. Accardi *et al.*, "Electron Ion Collider: The Next QCD Frontier: Understanding the glue that binds us all," *Eur. Phys. J. A*, vol. 52, no. 9, p. 268, 2016.

[21] J. K. Adkins *et al.*, "Design of the ECCE Detector for the Electron Ion Collider," 9 2022.

[22] J. Adam *et al.*, "ATHENA detector proposal — a totally hermetic electron nucleus apparatus proposed for IP6 at the Electron-Ion Collider," *JINST*, vol. 17, no. 10, p. P10019, 2022.

[23] O. D. Tsai *et al.*, "Results of \& on a new construction technique for W/ScFi Calorimeters," *J. Phys. Conf. Ser.*, vol. 404, p. 012023, 2012.

[24] C. A. Aidala *et al.*, "Design and Beam Test Results for the sPHENIX Electromagnetic and Hadronic Calorimeter Prototypes," *IEEE Trans. Nucl. Sci.*, vol. 65, no. 12, pp. 2901–2919, 2018.

[25] T. Nicholls *et al.*, "Performance of an electromagnetic lead / scintillating fiber calorimeter for the H1 detector," *Nucl. Instrum. Meth. A*, vol. 374, pp. 149–156, 1996.

[26] O. D. Tsai *et al.*, "Development of a forward calorimeter system for the STAR experiment," *J. Phys. Conf. Ser.*, vol. 587, no. 1, p. 012053, 2015.